Title

Integrated Physical and Computational Platforms to Monitor 3D Cyst and Organoid Growth

ISBN

9798247985686

Author

Susanto, Anna

Publication Date

2026-06-05

Peer reviewed|Thesis/dissertation

UNIVERSITY OF CALIFORNIA

Los Angeles

Integrated Physical and Computational Platforms to Monitor 3D Cyst and Organoid Growth

A thesis submitted in partial satisfaction

of the requirements for the degree

Master of Science in Bioengineering

by

Anna Susanto

2026

ABSTRACT OF THE THESIS

Integrated Physical and Computational Platforms to Monitor 3D Cyst and Organoid Growth

by

Anna Susanto

Master of Science in Bioengineering

University of California, Los Angeles, 2026

Professor Neil Lin, Chair

The morphological progression and dysfunction of tissue governs mechanisms in oncogenesis and organ development. To control and track this process, various physical and digital platforms like fabricated microwell arrays and segmentation algorithms were made. Developing them requires resources with limited accessibility, and both platform types struggle with more complex morphologies and environments. More specifically, irregular microwell topologies reduce image clarity and magnification, while many algorithms are not generalized enough to perform well for challenging image datasets. I integrated various fabrication and imaging strategies to improve on current microarray cell trapping and culture platforms by reducing resource requirements and enhancing confocal image quality. I then identified epithelial disorganization induced by microwell-imposed geometric cues. I also evaluated cutting-edge segmentation algorithms and combined the best performers to tackle less-attempted segmentation problems without high-compute environments. Overall, this thesis describes work that incrementally improves on efficiency and performance of organoid and cyst characterization platforms.

The thesis of Anna Susanto is approved.

Jennifer Wilson

Yue Liu

Neil Lin, Committee Chair

University of California, Los Angeles

2026

To my family

Contents

List of Figures

List of Tables

Acknowledgements

First, I would like to acknowledge Iris Sloan, who I collaborated with to generate cells grown in microwells. I would like to specifically thank her not only for the shared experiments and intellectual contributions but also her cell culture maintenance. I also would like to thank Dr. James Lo for sharing his prostate organoid dataset with me for segmentation and Dr. Alexandra Bermudez for her mentorship and Imaris reconstructions of our data. I also wish to thank Zoe Latham and Dr. Jerry Chen for their support and advice as I progressed through my degree, and Dr. Jennifer Wilson and Dr. Yue Liu for their feedback on my thesis. I am grateful for the mentorship from Dr. Neil Lin. The thesis and my development as a scientist would have not been possible without him. Last but not least, I would like to thank my family for their support both in life and in education over many years.

Chapter 1

Introduction

Tissue shape and architecture play key roles in organ function and behavior, homeostasis, and morphogenesis. The interplay between cells in the microenvironment and the surrounding extracellular matrix (ECM) drives this process. Chemical signals such as growth factors and hormones are transmitted through the ECM and taken up by surface receptors on the cell. Mechanosensitive receptors pick up on physical cues like stress, strain, and pressure from other cells and the surrounding microenvironment. These external stimuli transmit to the cell's nucleus, hence altering their genetic expression and downstream behaviors. Examples include tissue packing, planar and apical-basal polarity, apoptosis, differentiation, migration, metabolism, cytoskeletal re-organization, and more [49, 78, 84, 90]. Cells also remodel the environment, continuing to feed the cycle between tissue shape, environment, and cellular behaviors. Therefore, shape and architecture are simultaneously drivers and end results of tissue function [107].

Dysfunctional shape regulation in tissue is heavily implicated in the initiation and development of ailments including polycystic kidney disease (PKD), cancer, cardiovascular disease, pulmonary fibrosis, and various congenital diseases [100, 149, 172]. For tumors, disruptions in tissue architecture and alterations in mechanical properties and density contribute to

out-of-control mitosis and eventual metastasis as cancer cells vacate the tumor mass and migrate through the bloodstream to colonize distant locations [162]. For PKD, we observe it in the growth of painful, fluid-filled cysts instead of healthy renal tubules [147]. In order to elucidate the mechanisms and identify markers of disease progression as well as regression, it is necessary to thoroughly track changes and dysregulation of organ-level tissue architecture.

Given the difficulty of observing organs directly and the complexity of high-level predictions of organ behavior, researchers have resorted to smaller-scale tissues like organoids as models for biological processes. Drugs treating diseases such as cancer can be tested on organoids prior to rodent studies, and mechanisms and pathways underscoring organogenesis are easier to elucidate in *in vitro*. Therefore, it is of great interest to develop platforms that facilitate research into tissue growth and the impact of the microenvironment. There are two approaches to follow among many. One physically aims to control and enhance organoid growth. This can be achieved by developing microfluidics and patterning varying materials including hydrogels and other biocompatible polymers to control tissue growth, then culturing and monitoring cells inside. One application involves generating microwell arrays using well-documented fabrication techniques like soft lithography serving as platforms for single-cell, drug testing, and organoid manufacturing assays. The other is digital and mainly accomplishes computational analysis through the extraction of morphological features from the image data to characterize multicellular systems. This requires sensitive segmentation models.

We build on the prior work done characterizing self-assembly and growth of three-dimensional tissues and aim to improve on several fronts for both physical and digital platforms. We focus on developing polydimethylsiloxane (PDMS) microwell arrays due to the material's ubiquitousness in bioengineering and also because patterning through soft lithography is a very common technique used in microfluidics. We aimed to accomplish this task without use of a cleanroom, which often poses a cost barrier. Additionally, despite the various microwell studies, few papers have publicized exact protocols discussing signal-to-noise

ratio (SNR) and other imaging limitations imposed by sample topology, particularly at high magnifications and for live imaging. Therefore, we aimed to test and validate various mounting techniques to incorporate into the process as well as design a live imaging setup. The platform was leveraged to investigate a mechanobiological question through the epithelial cell culture system. In mechanobiology, it is well known that environmental cues, such as external stress or geometric boundaries dictated by the surrounding extracellular matrix (ECM), influence key biological processes. Particularly for epithelial cells, they regulate morphogenesis, and the consequences of dysregulated tissue organization is linked to cancer and PKD. Therefore, we aimed to understand if the physical constraints imposed by microwell arrays could impact and even disrupt the normal morphogenetic processes of planar monolayers and spherical cysts.

For digital platforms, characterizing these three-dimensional tissues benefits from high-quality segmentation models due to their speed compared to hand-drawn segmentation. However, the training process of these models requires high-performance computers as well as annotated datasets. While infinitely increasing dataset size does not guarantee infinite improvements in model performance, larger datasets and more complex models trended towards better performance in biomedical applications [85]. While some algorithms require less than a hundred images, the most cutting-edge or reliable models used hundreds to thousands [86, 98, 114]. Therefore, our first objective is in reducing financial and resource cost and improving accessibility by identifying pipelines that do not mandate this bottleneck. The second aim is to improve performance capabilities. While segmentation models are equipped to process the most common, circular organoid dataset types, they are weak against uncommon and complex organoid shapes and culture conditions. Recently, hybrid deep learning and classical algorithms showed an aptitude of leveraging the disparate strengths of both approaches, ultimately producing results at higher quality or efficiency [26, 71, 117]. Inspired by this concept, we hypothesized that by synthesizing different pretrained segmentation models with each other as well as classical computer vision algorithms, we

could address the challenges listed above with minimal hardware requirements. We tested this idea by developing hybrid pipelines tackling unusual organoid brightfield data.

The thesis is divided into these following sections following the introduction. The second chapter is a literature review which is split into several parts: mechanobiology, fabrication, and computer vision and segmentation. First, we explore the historical and more modern developments on epithelial cells in the context of cancer and developmental biology. More specifically, we delve into the impact of geometric cues and apical-basal polarity on key cellular processes, mainly morphogenesis. With the question of how geometric cues influence apical-basal polarity, we proceed into reviewing developments of engineered platforms with which to investigate cell packing and behavior, from chemical micropatterning of flat colonies to three-dimensional confinement in hydrogel wells. Finally, to explore methods that can quantify morphologies of more complex tissue structures, we survey a mix of classical and deep learning segmentation models before diving into organoid segmentation models published recently.

The third chapter is comprised of the fabrication and imaging PDMS microwell array platform designed for morphological assays of epithelial cells. We identify certain strategies and the minimum requirements to successfully fabricate microwells in a regular lab space without sacrificing resolution. We explored sample preparation and seeding strategies to maximize cell trapping and viability and optimized SNR for post-fixation samples. We also attempted to develop a live imaging platform comprised of 3D-printed pieces, but it was not a success. Thanks to the microwell platform, we were able to investigate the question of how and whether geometric cues could disrupt morphogenesis using epithelial cells as the model systems. We applied these microwell arrays to explore the impact of three-dimensional physical cues on epithelial monolayer and cyst growth. For monolayers, we noted that smaller wells induced multilayer epithelial packing, hinting at the potential involvement of monolayer tissue's hallmark apical-basal polarity. For three-dimensional epithelial cysts, we observed

mild lumen compression as well as other abnormal epithelial behaviors like multilayered or multilumen cysts. While the experiments yielded results of interest, throughput was too low to derive significant conclusions, so the next step to focus on is driving up the cystogenesis and cell trapping rate.

The fourth chapter continues with the goal of examining the morphology of complex structures, but also shifts focus to developing a GPU-free computational platform with which to extract these features. We begin by curating six pre-trained models from a list of recently published segmentation algorithms for organoids captured in brightfield microscopy and selecting the top two performers. Relying on their strengths and weaknesses, we integrated them along with classical segmentation algorithms to tackle two relevant challenges in the study of organoids in bioengineering: irregular shapes, and imaging artifacts imposed by the engineered microenvironment, looping back to one of the future objectives posed in the third chapter. The pipelines showed improvement and promise, but not at a statistically significant amount.

The thesis follows a theme of engineering physical and digital platforms to monitor growth of three-dimensional cellular structures at minimal resource cost with optimal performance. One aspect the two processes share in common is the synthesizing of varied, separate concepts towards a common goal. However, the major weakness remains their lower through-put results and future experiments should focus on increasing the organoid generation as well as enhancing segmentation. Results are summarized and further discussions and ideas for future experiments are expounded upon in the final chapter.

Chapter 2

Literature Review

2.1 Epithelial Confinement

2.1.1 Role of Epithelial Tissues in Function and Disease

Epithelial cells line the surfaces of the body, including the skin, gut, and lungs [82]. The most basic form of epithelial tissue is a layer of single adherent cells comprised of an apical (top) and basal (bottom) side while displaying cobblestone packing [162]. In the body, epithelial tissues generally develop into three-dimensional glandular structures like hollow spherical cysts and singular or branching tubes [133]. Epithelial tissue functions as a barrier against external invaders like microbes and pathogens and helps regulate the immune system through recruitment and secretion of immune-associated proteins [32, 62]. They are also involved in gas exchange, tissue regeneration, and structural maintenance [15, 29]. Dysfunction of epithelial tissues can lead to diseases like cancer, polycystic kidney disease (PKD), and many autoimmune disorders [100, 149, 172].

Biological processes in which epithelial cells participate include morphogenesis and oncogenesis. Epithelial cells form many varying three-dimensional structures during embryo

development including tubes and grooves as well as regulate branching morphogenesis [66]. More physiological examples include epithelial tissue elongation during limb development, invagination in glands, buckling of gut tissue to increase absorption area, branching in the lungs and kidney, and fusion of tissues for organogenesis [61, 83, 87]. Disruptions in normal functioning are implicated in PKD and birth defects such as coloboma and cleft palate [115].

The majority of tumors originate from epithelial cells [18]. Breast, prostate, and colon carcinomas stem from multiple oncogenic mutations occurring in epithelial tissue [24, 55]. Improperly regulated epithelial heterogeneity can lead to out-of-control mutations which eventually send the cell down an oncogenic path, and failures in restricting epithelial morphology contribute to changes in mechanical tissue properties and architecture linked to upregulated proliferation and suppressed apoptosis [162]. One of the key roles epithelial tissue plays in cancer progression and metastasis is the epithelial-mesenchymal transition (EMT), in which epithelial cells uptake properties of mesenchymal tissue and remodel their cytoskeleton in ways that facilitate migration and invasion beyond the initial tumor site as well as cancer hallmarks like anoikis resistance [27, 69]. Therefore, the study of epithelial cells would provide key insights into the structural defects that drive developmental defects as well as tumor growth and metastasis.

2.1.2 Apical-Basal Polarity in Epithelial Tissue

One significant property of epithelial cells that influences tissue development and cancer is apical-basal polarity, which dictates their barrier, diffusive, and transport functions, helps organize internal structure, and regulates morphogenetic processes such as formation of lumens and more complex tissue structures [18, 23]. Apical-basal polarity divides epithelial cells into three domains—the apical, or top surface, the lateral, or sides, and the basal, or bottom surface. The apical side facilitates protection against foreign pathogens, transport of ions, and mechanotransduction [6]. The lateral domain participates in cell-cell adhesion,

signaling, and mechanical homeostasis [153]. Finally, the basal side anchors the epithelial cells to the surrounding microenvironment.

Apical-basal polarity can be identified by the organization and localization of specialized protein factors. The apical domain is associated mainly with the polarity Par and Crumbs complex with the regulatory enzyme atypical protein kinase C (aPKC) playing a particularly significant role [18, 23]. E-cadherin-based cell-cell adhesions also influence the development of the apical side [89]. The border between the apical and basolateral regions is marked by the presence of the tight junctions, or zonula occludens [165]. In the lateral domain, the scaffold protein Bazooka is involved in the formation of adherens and tight junctions [19, 144]. As for the basalateral domain, the Scribble and Discs large complex are well-known polarity factors [77].

How epithelial cells are polarized depends on the overall architecture and environment. For epithelial monolayers, the apical side faces the external environment while the basal side faces the adherent surface. However, epithelial cysts experience the opposite. The apical side lines the inner surface of the shell and is in contact with the lumen while the basal surface is external [106]. Several mechanisms can explain this cyst development, which occurs without any guidance from an adhesive surface. Apoptosis of internal epithelial cells hollows out an aggregate and leaves a lumen behind, apical proteins are trafficked where cell-cell adhesion proteins usually reside on the luminal side, or apical-basal polarity guides fluid pumping into the space that becomes the central lumen [109]. These two scenarios demonstrate links between apical-basal polarity and tissue development.

Additionally, all changes in tissue shape require alterations in shape and size of the apical, basal, and lateral domains, further implicating polarity factors in any morphogenetic events [144]. For example, apical constriction, or a decrease in the area of the apical surface, is known to drive invagination, sheet bending, and more [136]. Investigating the process of establishing and maintaining apical-basal polarity as well as environmental influences is

necessary to answer physiologically relevant questions on morphogenesis.

Beyond participating in tissue and embryo development, apical-basal polarity is known to block tumor initiation, EMT, and metastasis, and a loss of this polarity can be considered a sign of cancer and EMT [67]. Generally, abnormal epithelial cells are eliminated through cell extrusion followed by anoikis. However, dysfunctional apical-basal polarity causes piling of these cells, which in turn promotes oncogenesis [148]. The different types of abnormal polarity shifts associated with tumors can be identified as a reduction, complete loss, or inversion [122]. They are tied to cancerous behaviors such as transition from a fluid to filled, solid lumen, dysfunction of cell-cell junctions that increases metastasis chances, and overproliferation, and are linked with worse clinical prognosis.

2.1.3 Role of Mechanical Microenvironment in Epithelial Behaviors

For both morphogenesis and cancer, the mechanical environment plays a key role in its initiation, regulation, and progression. Cells pick up and respond to many physical cues like pressure, stiffness, and confinement from neighboring cells and the extracellular matrix (ECM) by remodeling the cytoskeleton and microenvironment [1, 38]. They are as important as chemical cues in the maintenance of epithelial cell behavior and function and therefore have many downstream effects in developmental and cancer biology. Below, we explore several recent examples emphasizing the role of epithelial cells.

This sophisticated interplay between environmental forces and cells impacts cellular epigenetics as well as biochemical and tension gradients, known factors that regulate morphogenetic events [38]. For example, the mechanosensor Piezo1 regulates morphogenesis by transmitting the mechanical cues it receives through the Yes-associated protein (YAP) and mitogen-activated protein kinases (MAPK) pathways, both of which mediate tissue development and are affiliated with cellular mechanotransduction [59]. Very recently, it

has been shown that changes in apical constriction of epithelial cells mediate neural plate folding in *Xenopus* [97]. Additionally, in *Drosophila* wing discs, the discrepancies in growth between the tissue and the surrounding ECM drive tissue bending and morphogenesis in three dimensions [48].

In cancer, physical cues derived from ECM and interstitial fluids boost malignancy and metastasis by selecting for cells that exhibit such traits [1]. In the intratumoral region, cells and the ECM engage in a vicious cycle where ECM promotes growth by altering the stiffness of the tumor, which in turn remodels the ECM to be even stiffer [43, 175]. This can be observed in how epithelial cells self-regulate by pushing out malignant cells via extrusion, but cancer-driven changes in environmental stiffness block the process [4]. When ECM deforms, apical-basal polarity is changed, which continues to drive forward tumor progression and further ECM remodeling [122]. Commonly but not always through EMT, malignant epithelial cells escape and squeeze through tissues and blood vessels to colonize distant sites in the body, a process that requires cellular ability to sense and react to mechanical forces [171]. A keratinocyte stretch study showed that Piezo1 is just one of multiple mechanosensors involved in EMT regulation [50].

One key aspect of mechanotransduction is confinement because they provide environmental and geometric cues that shape future tissue growth and behavior. Experiments suggest that the physical constraints imposed by artificial boundaries mediate events like neural tube folding, [72]. Additionally, confinement studies are helpful for elucidating the biophysical factors and mechanisms governing biological processes. Studies engineered to mimic confined *in vivo* environments have investigated the relationship between tension arising from cell adhesion and cell fate in mesoderm development [104]. All these examples discussed above show the significant influence of mechanotransduction on epithelial cells and demonstrate that systemic geometric control of the cellular microenvironment has analyzed and is capable of answering many physiologically relevant questions [47].

2.1.4 A Review of Geometric Confinement Studies

Chemically patterning surfaces to generate adhesive islands that restrained cell spreading has historically been the most well-known strategy with which to engineer geometric cues. One of the pioneering works in physical confinement showed that the shape and size of chemically micropatterned islands, or essentially geometric cues, mediated survival or apoptosis of endothelial cells [22]. Later on, it was demonstrated that confined epithelial and endothelial monolayers also impacted cell growth and proliferation due to the mechanical forces imposed by tissue patterning. Essentially, cell growth shaped tissues, which then mediated future growth [108]. Deforet and colleagues observed that restricting epithelial cells to circular adhesive regions was sufficient to trigger events similar to morphogenetic transitions from two to three dimensions as well as radial velocity oscillations [32]. Patterning also led to the discovery that anisotropic boundaries affected epithelial cell polarity [155]. Two-dimensional chemical patterning was not only used for monolayers, but also on epithelial cysts to illustrate the influence of physical confinement on its development. The boundaries of adhesive islands regulated cell contractility, which then impacted where centrosome localization, lumenization, and polarity [132]. While two-dimensional confinement has been shown to be enormously helpful in untangling questions on tissue growth and apical-basal polarity, they cannot recapitulate *in vivo* systems as well as engineered three-dimensional environments.

Microchannels and microtubes were developed in order to examine functions such as cell migration for tubular epithelium and for collective migration [121]. They are usually microscopic, tubular openings inside microfluidic devices. Hydrogel microchannels with tunable parameters showed that stiffness or confinement can both modulate EMT transitions in mammary epithelial cells [105]. One study engineered microtubes in PDMS to examine modes of migration for epithelial cells in tubes. Additionally, as the microtubues successfully captured the physiological environment, they were able to reproduce *in vivo* apical-basal polarization [169].

The work done on microwells is explored in particular detail below. Early work focused on microwell fabrication and cell trapping in order to demonstrate proof-of-concept, but future studies began leveraging this technology in order to make scientific discoveries [128, 129]. Polydimethylsiloxane (PDMS) cylindrical microwells that mimicked intestinal crypts impacted the spreading, metabolism, and differentiation of intestinal epithelial cells [164]. When spherical microwells were coated with ECM proteins, the apical-basal polarity and self-organization of epithelial cells cultured inside varied based on ECM distribution [58]. Hydrogel-based bowl-shaped microwells provided another promising technology with which to explore complex tissue structures by tuning curvature of the environment, and its topology caused actin cables to form around the bowl edges as well as modulate nucleus properties like orientation and packing due to the cytoskeletal changes [94]. Very recently, to investigate scaling in mechanobiology, lung epithelial cells were seeded into polycaprolactone (PCL) microwells. Cells in smaller microwells tended to extend across the opening, therefore deforming the nucleus and increasing its flexibility, which has implications in tumor progression and EMT initiation [53]. While varying shapes and sizes have been explored, systemic work on how microwell size impacts hallmark epithelial behaviors like apical-basal polarity has not been fully explored.

Microwells show much potential for growing organoids and engineering complex tissues in the future. Honey-comb shaped microwells were also able to successfully culture three-dimensional aggregates and cysts of biliary epithelial cells, with the ultimate goal of engineering liver tissue [130]. Microwells created with perforated bottoms provided an environment in which intestinal crypts transferred inside these wells could develop structures mimicking a colon's epithelium [166]. Bubble-shaped microwells could also grow bronchial organoids with complex pseudostratified epithelial layers and coculture epithelial cells and fibroblasts to generate bronchospheres. [11, 39]. Square microwells made of an electrospun polycaprolactone scaffold facilitated acinar growth of human salivary gland cells [140]. Most studies focus on culturing, not the impact of compression on epithelial cyst development.

2.2 Microwell Fabrication

2.2.1 Microwell Design and Fabrication

Many parameters of microwells can be adjusted to fit experimental needs. They can be comprised of many shapes including hexagons, circles, and squares. Other tunable parameters include dimensions of the microwells including depth as well as the space between microwells to control the number of cells that sediment inside the wells and adhere on the surface. The aspect ratio between well size and well depth can dictate the type of tissue formation that occurs [96]. The material used for microwells is also a key component, as properties like stiffness is a key axis in mechanobiology [63]. Examples include PDMS, PCL, polystyrene (PS), and hydrogels such as polyethylene glycol (PEG), all of which are biocompatible [70,140]. Despite its hydrophobic, protein-repellent nature, PDMS is one of the most commonly used materials for microfluidics and microwell fabrication because of its transparency and lack of toxicity [**?**, 102]. PDMS microwells are particularly useful when examining interactions between cells due to its replicability and easily tunable parameters [96].

Various engineering methodology to fabricate microwells has been devised, including soft lithography, photolithography, 3D printing, etching, and laser ablation [2, 96]. PDMS microwells are commonly generated by standard soft lithography techniques which are discussed below. The three major steps in this process include preparing the chrome photomask which contains the desired patterns, fabricating the silicon mold, and finally generating the PDMS microarrays using the mold. Computer-aided design (CAD) softwares produce pattern designs, which are then printed at high resolution on the mask [125]. The mask is then utilized to transmit patterns onto a silicon master via photolithography, typically via an ultraviolet (UV) light source. First, some form of photoresist is spuncoat and layered onto a silicon wafer, which is pre-baked to evaporate photoresist solvent. The mask is lowered onto wafer, and UV irradiation initiates cross-linking. Afterwards, the wafer is baked again,

then submerged in developer to facilitate pattern formation. To completely solidify the patterns, the master is baked a final time. PDMS is cast onto the master and cross-linked in an oven, and the PDMS microarrays are peeled off after sufficient time [125].

Fabrication parameters, like photoresist choice and PDMS subtype dictate the resulting dimensions of the microwells. First, spin coater settings like rotation speed and time influence coating thickness, with higher speeds trending towards thinner layers [10]. The pre-bake and post-exposure bake parameters impact the uniformity of microstructures. [168]. The type of coating applied on the wafer also matters. For instance, UV-exposed positive photoresist turns soluble in the developer, while exposed negative photoresist, such as SU-8 hardens [110]. This process allows patterns to form in the developer, because developer dissolves unneeded photoresist, leaving only pillars behind. While the most common PDMS fabricated uses the curing agent Sylgard 184, there are many other variants, like Sylgard 527, which yield different mechanical properties such as stiffness and elasticity [116]. It is therefore crucial to select materials and parameters that optimize microarray properties to best fit experimental needs. Major challenges of soft lithography-based fabrication include financial cost, fidelity, complexity, and diffraction [96]. Resolution and consistency can be ruined by debris and other small particles contaminating the SU-8 photoresist [111]. Therefore, fabrication generally occurs in a clean room facility, which is expensive to maintain. However, multiple alternatives like fabrication without clean room use, laser ablation, and 3D printing, have been proposed [123, 131]. Diffraction, particularly if the photolithography light source is of poor quality, can create imperfect patterns [36].

2.2.2 Cell Trapping and Imaging

One of the early bioengineering studies on cell culture in microwells devised a technique with which to fabricate microwells and optimized cell trapping for both adherent and non-adherent cells, additionally providing the geometric and seeding parameters with which to obtain the

desired settling density [128]. Many cell trapping applications rely on sedimentation to allow gravity to naturally direct cells inside the microwells, but optimizing this process requires very precise tuning of number of sedimentation cycles and of the settling times [96]. There are many other strategies however such as dielectrophoresis, controlled flow, centrifugation, and optoelectronic tweezers [42, 118, 119, 130]. In order to achieve high-throughput assays that can answer physiologically relevant questions, it is necessary to optimize cell trapping with minimum impact from unrelated stimuli.

Imaging for microwells is challenging because of their inherently complex topology leading to diffraction and reduction of signal-to-noise ratio (SNR), particularly if the microwells are deep. Ochsner and colleagues engineered PDMS microwells which could precisely control the microenvironment of single cells and could also be imaged at high resolution. However, their microwells were less than 10μm deep [101]. Similarly, He and colleagues achieved 63X oil immersion (OI) magnification, but the dimensions of their microwells experienced large sample variance [53]. Hydrogel-based bowl and cylindrical microwells also achieved high SNR up to 40X magnification [58, 94]. Few high SNR images of three-dimensional epithelial structures at larger magnifications have been publicized at this point in time.

2.3 Organoid Segmentation

2.3.1 Segmentation Algorithms

In biology, significant amounts of information can be extracted from images, both confocal and brightfield. Examples include size, shape, motion tracking, aspect ratio, and cell counting. ImageJ, and then later an improved version, Fiji is Just ImageJ (FIJI), is one of the most used softwares developed in order to facilitate image analysis and processing [137]. However, to be able to obtain image data of biological samples, segmentation is one crucial step. Hand

segmentation may provide the most accurate boundaries, but it consumes a significant amount of time and is unfeasible for more recent studies such as high-throughput drug-testing assays combined with microfluidics, which is growing in popularity in the age of "big data" along with genomics and single-cell assays [30, 176].

Prior to the explosion of deep learning models in the biological sciences, many mathematical algorithms were employed to facilitate image segmentation to varying levels of success. Thresholding is one of the most straightforward segmentation algorithms and classifies pixels as object or background by comparing their intensities to a pre-determined value. Global thresholding assumes bimodal pixel values, thereby setting a universal threshold. For example, the Otsu method determines this value by optimizing pixel variance [64]. On the contrary, for adaptive thresholding, its threshold value depends on the pixel location and is thus better suited for images with more complex intensity histograms. Besides thresholding, various clustering algorithms like K-means, log-based clustering, and fuzzy C-means can also group pixels [139].

Another key component is edge detection, in order to identify the boundaries of cells, organoids, and other biological structures. Common filters that rely on changes in pixel intensity or its gradient include Sobel, Canny, and Laplacian operators [65, 103, 174]. Algorithms developed more recently rely on Gaussian differences and multiscale features [150]. A third category of segmentation techniques involves watershed algorithms, which treat images as a flooded topographic relief and delineate object and background based on where the analogous water lines are identified [80]. Finally, region growing algorithms generate seeds throughout the image that grow to form segmentation masks by combining domain knowledge and connectivity within neighboring pixels [74].

2.3.2 Deep Learning Segmentation Models

The advancement of artificial intelligence, particularly deep learning, has further enhanced segmentation performance. The first step towards deep learning began with the development of convolutional neural networks (CNNs) in order to achieve various computer vision tasks such as object recognition and tracking. CNNs are widely used because their shared parameters reduce computational expense, they can address many applications, and their building blocks can be scaled up to custom architectures [5]. Their main innovation comprises the invention of the convolution layer, which convolve kernels across the image. This process identifies spatial information and features useful for segmentation [44]. The architectures of CNNs are varied, but generally involve combinations of convolution, pooling, fully connected, and activation layers. Various CNNs designed over the years include AlexNet, Visual Geometry Group (VGG), GoogLeNet, ResNet, Mask R-CNN, and U-Net [51, 52, 81, 134, 142, 151].

U-Net in particular was targeted towards biomedical datasets from the onset. Its unique contributions involves the introduction of a symmetric, U-shaped path and skip connections that improve localization by tying together representations generated at varying stages [9]. The left half of the path, or the contracting side, takes in the image and applies downsampling in order to produce a map made of semantic features. Then the expansion side on the right upsamples the feature map to output scores associated with each pixel of the original image. [9, 134]. U-Nets caused a breakthrough in not only medical but also biological segmentation [93, 141]. One particularly well-known application in biomedical research lies in the earlier versions of CellPose. Inspired by watershed algorithms, it first extracts gradient flows from the input images and feeds them to a U-net modified with residual blocks [145].

After CNNs, various models emerged. Algorithms strong for sequential data, like recurrent neural networks (RNNs), long term short memory (LSTMs), and transformers, were introduced. By integrating self-attention mechanisms that drives long-range sequential learning, transformers in particular have drastically advanced the deep learning field forward

due to groundbreaking performances in sequence and natural language processing [68, 159]. They have also shown success in biomedical segmentation through softwares like SwinCell, CellT-Net, and Cell-TRACTR [113, 161, 170, 175].

Beyond transformers, greater access to unannotated data led to the development of complex algorithms dubbed foundation models which were trained on gigantic datasets through self-supervision or traditional training with zero-shot generalization abilities. Prime examples include BERT for natural language processing and DALL-E for image generation [16, 34, 127]. The flagship foundation model for segmentation is the Segment Anything Model (SAM) accompanied by a dataset of eleven million images which served as a step towards promptable, zero-shot algorithms that could outperform older models designed for specific tasks [79]. Given the significance of segmentation in biomedical research, versions of SAM for cell and microscopy images were soon published [8, 60, 158]. The creators of CellPose also released the generalized segmentation software CellPose-SAM, which integrates the pretrained weights from SAM into the preexisting model [114].

One challenge for implementing deep learning algorithms involves training, because the process necessitates high-compute devices as well as annotated datasets often ranging from hundreds to thousands of images [86, 145]. Datasets can be curated to achieve equivalent performance with smaller, high-quality inputs, but training is still a problem [21]. One potential method to overcome the bottleneck is through transfer learning, a tactic where a pre-existing model is fine-tuned on a different, but related task, thereby reducing computational load [157]. Another possibility is in combining deep learning and classical segmentation algorithms. Hybrid deep learning and classical segmentation models have also been created for specific tasks, which draw upon and navigate their isolated strengths and weaknesses with the end goal of improved quality or efficiency [26, 71, 117]. Despite the difficulty discussed here, deep learning segmentation models have exhibited high levels of performance across many fields, including biomedical and clinical research.

2.3.3 Organoid Segmentation Models

Many models in biomedicine so far have focused on medical image or single cell or nucleus segmentation [54, 92, 127]. However, significant process has been made towards organoid segmentation. Key challenges such algorithms must tackle are image artifacts caused by culture conditions. The three-dimensional culture causes organoids to be scattered not only horizontally but also vertically, so organoids in a single image may exhibit varying levels of focus and sharpness. Additionally, density variances causing overcrowding, sparsity, and occlusion can weaken and confuse the model. Finally, irregular lighting in culture wells poses an issue [73]. In order to resolve the challenge of high-throughput segmentation of organoids in bright-field images, several models have been developed over the years. The Matlab-based OrganoSeg was designed to grapple with out-of-focus organoids. Its pipeline is as follows: open-close operations, adaptive thresholding, and then finally Otsu's thresholding. Users can modify parameters in the graphic user interface (GUI) and adjust for various datasets [17]. OrganoSeg was also used a baseline for other models. In 2026, an improved version of OrganoSeg, or OrganoSeg2, which is reported to have beaten many deep learning models' performances, was released. Improvements compared to OrganoSeg include more parameters as well as faster segmentation time [167].

With the advent of deep-learning algorithms, the organoid segmentation field has made great progress. OrgaQuant, a deep learning model based off Google's object detection API, and Deep-Orga, a YOLOX-based model, mark bounding boxes around intestinal organoids in brightfield images. However, they are not capable of elucidating boundaries [73,88]. MOrgAna is a segmentation pipeline for brightfield and fluorescent organoid images that is applicable for varying cell types, experimental settings, microscope magnification, and microscope device. MOrgAna utilizes either logistic regression or a multi-layer perceptron network to distinguish between background, contour, and organoid. However, its segmentation is limited to images containing one organoid [45]. OrganoID improves on the limitations of OrgaQuant

further, enabling fast, high-throughput analysis of multiple organoid types, with the goal of generalizing organoid segmentation over many timepoints. The pipeline incorporates a CNN followed by contour resolution and tracking and is recognized for its speed [98].

By combining object detection and semantic segmentation through its Mask R-CNN backbone, OrgaSegment was designed to identify intestinal organoids in brightfield images. Its particular strength lies in its ability to segment acircular and irregular morphologies as well as individual organoids inside clusters [51]. Like OrganoID, it incorporates tracking functions as well [86]. A U-net model trained by a dataset generated by a conditional generative adversarial network could successfully track and identify mammary organoids [56]. A fast, user-friendly multiscale U-net model called OrgaExtractor was also designed that specializes in smaller organoids, which many models struggle with. However, it fails for blurry or occluding organoids. [120]. An enhanced U-net model paired with ROI refinement was developed in order to overcome imaging artifacts like blurriness as well as acircular morphology. However, it is unable to deal with occlusion [3].

MACPNet, a fusion of convolution parallel blocks and multi-axis attention mechanisms, was designed to identify on long-range dependencies between pixels, showing improvement over contemporary models like OrganoID. Additionally, it does not consume high levels of computational resources [57]. TransOrga-plus, a knowledge-based transformer model, can generalize across varying experimental and morphological conditions of the organoids. Its pipeline integrates domain-specific knowledge during training to decrease need of annotations [126]. Very recently, precision organoid segmentation technique (POST) was developed as a generalizable organoid segmentation algorithm that overcomes common imaging artifacts. Quantitative analysis facilitated by POST segmentation demonstrated links between viability and morphology [37].

Many of these models demonstrate strengths in particular aspects of segmentation, whether minimization of computational resources, generalization across various organoid types, ability

to segment clusters, and irregular morphology. However, it seems rare that one model is capable of resolving all these challenges simultaneously.

Chapter 3

Developing a physical platform for high signal-to-noise ratio images of tissue structures

3.1 Overview

One of the key axes of mechanobiology, geometric cues, plays significant roles in cancer progression, embryo development, and tissue regeneration. Engineering artificial cell confinement technologies like microwells can provide a standardized platform with which to investigate the impact of the mechanical microenvironment on cell behavior. Here, we optimized strategies to image deep inside microwells without sacrificing SNR. Leveraging these microwells, we also demonstrate their use in a biological context by exploring epithelial cell self-organization under varying culture conditions and confinement. For two-dimensional cultures, epithelial cells deviated from expected monolayer behavior and exhibited piling, while for three-dimensional cultures that yielded epithelial acini, we observed lumen compression as well as isolated cases of epithelial stratification and multilumen formation that warrant further investigation. These

preliminary observations suggest that apical-basal polarity may be impacted by geometric confinement, and our PDMS microwell array serves as a platform by which to elucidate the mechanism.

3.2 Introduction

Applying artificial physical constraints when culturing cells is a very simple, reproducible way to study questions in morphogenesis and tissue development, the answers of which can be applied to understand tumorigenesis and metastasis and assemble strategies with which to engineer complex tissue structures in laboratory settings [4, 152]. Geometric confinement in epithelial tissues has been extensively explored in two-dimensional patterning, where surfaces are selectively coated with adherence-promoting proteins like fibronectin to control where cells spread and proliferate [22, 32, 155]. Three-dimensional confinement methods, including cylindrical and spherical micro-wells which trap cells, have been also generated to better imitate the *in vivo* environment morphogenesis occurs in [58, 164].

These assays provide an excellent opportunity to study the tissue development process, particularly the intricacies of cell packing, nuclear morphology, and cytoskeletal organization in high detail. The three-dimensional environment shows particular potential for examining processes that extend into the Z-plane. One particular phenomenon that is well-suited for this engineering platform is apical-basal polarity, a hallmark of epithelial development, which involves the spatial organization of cells into three vertical domains: apical, lateral, and basal [18]. It governs processes in both two- and three-dimensional epithelial culture by regulating epithelial monolayer growth on adherent surfaces and epithelial cysts and acini, which are spherical shells comprised of a single layer of epithelial cells encapsulating a fluid-filled volume known as a lumen [112]. Besides growth, apical-basal polarity dictates barrier and adherence function by controlling where relevant proteins localize, and defects

are implicated in cancer development and metastasis [18]. The physical constraints imposed by micro-wells may serve as the biophysical geometric cues that are known to regulate apical-basal polarity. By tuning the parameters of the micro-wells, we can then explore the impact environmental size has on epithelial tissue polarity through confocal images illustrating their packing and morphology.

However, three-dimensional morphogenesis assays are much more challenging to image and observe. One must contend not only with the complex shape of the cells themselves, but also with the topology of the sample they are seeded into. This can lead to difficulties like diffraction and inability to obtain images at sufficiently high magnifications. While many studies have been conducted on tissue development and cell trapping in micro-wells, no studies to our knowledge have published strategies to produce reproducible high signal-to-noise ratio (SNR) confocal images of confined epithelial structures that specifically address complications caused by sample topology. Furthermore, apical-basal polarity in the context of three-dimensional geometric constraints with systemic control has not been as explored as thoroughly as other biological processes like differentiation.

Therefore, we designed a PDMS microwell array accompanied by a sample imaging setup with tunable geometric and cell trapping parameters to answer fundamental questions on morphogenesis in epithelial cells. With this platform, we investigated whether the size of the micro-well impacts healthy epithelial monolayer development and polarization and whether micro-well imposed barriers can influence lumen formation, one of the results of apical-basal polarity processes, during epithelial cyst development. We were able to demonstrate that small micro-wells cause defects in epithelial monolayers, with depiction of cell aggregations which may have been caused by disruptions in apical-basal polarity. Secondly, we also observed that microwells confined developing epithelial acini and resulted in abnormal lumen and cyst development in certain cases. These observations show that our microwell array and imaging setup are promising in terms of providing a platform which can be leveraged as one

of the simplest morphogenetic models.

3.3 Methods

3.3.1 Wafer fabrication

Chromium photomasks containing patterns of 20 and 30 μm diameter circles, 60 and 100 μm long squares, and 70 x 140 μm rectangles were utilized to transfer patterns made of negative photoresist SU-8 onto 50.8 μm silicon wafers through photolithography. All fabrication occurred inside a fume hood with the lights off and did not require a clean room. First, a layer of isopropryl alcohol (IPA) (Isopropyl Alcohol; Sigma Aldrich, 67-63-0) was dispensed on the surface of the silicon wafers. To dry off the alcohol, silicon wafers were spuncoat at 1700 revolutions per minute (RPM) for 30 seconds, then baked in a deep ultraviolet (UV) oven for 5 minutes. Approximately 5mL of SU-8 (SU-8 2025; Kayaku) was poured in a large droplet on the wafer surface and spuncoat at 1500 RPM for 30 seconds for shallower wells and 1000 RPM for 45 seconds for deeper wells. They were spuncoat for an additional 30 seconds if the coating appeared uneven.

The wafer was then pre-baked atop aluminum-covered hot plates at 65℃ for 3 minutes, than 95℃ for 10 minutes to evaporate sufficient amount of water in SU-8. Spincoating the SU-8 causes a bead to form on the boundaries, so a cleanroom, lint-free wipe sprayed with acetone was then used to gently remove the 2-3mm wide excess layer of SU-8 till the silicon substrate was revealed. For maximum success at removing the bead, the wipe traced the wafer unidirectionally and acetone was regularly re-applied. To evaporate the acetone, the wafer were returned to the hotplate and baked at 65℃ for 10 seconds, than 95℃ for 30 seconds.

The wafer was then aligned with the photomask regularly with some pressure to ensure

the mask would stick. In order to initiate cross-linking and obtain sharp, even dimensions for the transmitted patterns, we exposed the wafer and pattern for 15 seconds to UV light from a collimated source (LEDD1B; Thorlabs). As SU-8 is a negative photoresist, unexposed regions will not crosslink and will be washed away while the exposed regions will remain. After peeling off the photomask, the wafer underwent a post-exposure bake at 65℃ for 1 minute, than 95℃ for 5 minutes. This step completed the cross-linking process and harden the exposed areas.

After cooling to room temperature, the wafer was developed to wash away the unexposed regions. Two beakers were rinsed with IPA, than filled with IPA and propylene glycol methyl ether acetate (PG-MEA) (Propylene glycol monomethyl ether acetate; Sigma Aldrich, 484431-1L). The wafer were submerged in PG-MEA for 4 minutes, with the beaker being swirled every minute to ensure sufficient coverage of PG-MEA. The wafer was then dipped into IPA to confirm development and wash off PG-MEA and SU-8 residue. If the IPA turned cloudy, this signified excess amounts of uncrosslinked SU-8 and indicated that the wafer needed more time in PG-MEA. Otherwise, the wafer could then be extracted from the IPA bath, sprayed with more IPA to wash off remaining residue and dried.

A final hard-bake is necessary to make the fabricated SU-8 structures as robust as possible. First, the wafer was baked for 1 minute at 65℃. It was then transferred to a 95℃ hotplate. The temperature was ramped up to 150℃ and the wafer was baked for an additional ten minutes after.

3.3.2 PDMS fabrication

Polydimethylsiloxane (PDMS) and its curing agent Sylgard 184 (SYLGARD 184 Silicone Elastomer Kit; Dow) was mixed at a 10:1 ratio. Depending on the thickness desired of the PDMS sample, 1-5mL of the PDMS mixture was poured onto the surface of a wafer. Most

experiments utilized 1mL as thin layers of PDMS were needed. However, for the live imaging devices, thicker PDMS was required, thereby mandating 5mL per batch. Aluminum foil cups with 90mm diameter and 15mm height were created as a replica of a Petri dish, which served to keep the wafer and PDMS inside while remaining malleable and flexible enough to avoid wafer cracking during demolding. To keep surfaces level, a PDMS ring was also placed on unpatterned margins of the wafer to control PDMS flow. The cup containing the wafer and PDMS was transferred to a 60℃ oven and baked between 4 to 16 hours. Afterwards, the PDMS was peeled off from the wafer.

3.3.3 Sample Preparation for 2D Epithelial Culture

PDMS patterned with microwells were washed with deionized water (DI) to remove debris. They were cut into smaller pieces and placed inside well plates using tweezers. For thin PDMS samples, 3D-printed polylactic acid (PLA) ring inserts were sterilized in ethanol for 5 minutes and placed on top to ensure the PDMS samples would not float. The ring inserts were designed by CAD software, with an outer diameter of 0.9cm, inner diameter of 0.7cm, and a thickness of 0.1 cm. The designs were engraved using the laser cutter at UCLA Samueli makerspace.

2mL ethanol was pipetted into each well containing a sample, and to balance the centrifuge, MilliQ water was pipetted into each corresponding well in an empty well plate. The two well plates were placed in the centrifuge and spun at 100 relative centrifugal force (RCF) for 3 minutes. Under sterile conditions, the ethanol was aspirated and replaced with 2mL phosphate-buffered saline (PBS)(-/-) (DPBS (10X), no calcium, no magnesium; Gibco, 14-200-075). After another round of centrifugation at 100 RCF, the PBS(-/-) was aspirated and the sample was washed once with 2mL PBS(-/-) per well. The samples were treated with 2mL of 20 μg/mL fibronectin to promote cell adherence. They were centrifuged at 100RCF for 3 minutes, then were de-gassed for 30 minutes and incubated overnight in 4℃ fridge.

3.3.4 Sample Preparation for 3D Epithelial Culture

The process is as described above until the fibronectin coating. Instead, 500 μL anti-cell adherent (Anti-Adherence Rinsing Solution; STEMCELL Technologies, 07010) was pipetted inside the wells, which were spun down at 100 RCF for 3 minutes to ensure every surface was coated with anti-cell adherent. The sample was incubated in a degasser for 30 minutes. Afterwards, the anti-cell adherent was aspirated and the sample followed by three cycles of PBS(-/-) washes followed by centrifugation. Finally, the sample was baked in the 60℃ oven overnight to evaporate anti-cell adherent residue.

3.3.5 2D Epithelial Cell Culture

The cell culture was performed by Iris Sloan. Madin-Darby Canine Kidney (MDCK) cell cultures were grown in Minimum Essential Medium Alpha (MEM-alpha; Fisher Scientific, 12561-056) with 10% fetal bovine serum (FBS; Fisher Scientific, 12662-029) supplement and 1% Penicillin–Streptomycin (Fisher Scientific, 15140-122) to prevent microbe growth. The cell flasks were incubated at 37 °C and 5% CO2 under humid conditions. When cells were 80% confluent, they were detached via Trypsin–EDTA solution (Fisher Scientific, 25300-054) and centrifuged at 250 RCF for 3 minutes, and a cell pellet was separated from the supernatant. The cells were seeded into the wells and spun down at 100 RCF for 3 minutes to ensure they were driven into the micro-wells. The samples were stored in a 40℃ incubator for 45 minutes, then imaged at 20X on a brightfield tissue culture microscope to confirm successful trapping. Cell culture was replenished every 2-3 days until day of fixation and samples were monitored daily.

On the day of fixation, media was aspirated out and the samples were washed with PBS(-/-) once, then incubated in 4% formalin in PBS(+/+) (DPBS (10X), calcium, magnesium; Gibco , 14-040-141)in a fume hood for ten minutes. The samples were then washed twice

with PBS(+/+), wrapped in parafilm, and stored at 4℃.

3.3.6 3D Epithelial Cell Culture

1:1 Growth Factor Reduced (GFR) Matrigel (Corning Growth Factor Reduced Matrigel, CB40230C) was thawed overnight at 4℃ on ice. The well-plate containing the samples were placed on ice inside the 4℃ fridge to ensure sufficient cooling prior to cell seeding. The cell culture was performed by Iris Sloan, and utilized LifeAct-14–eGFP expressing MDCK (Madin-Darby Canine Kidney) cells [12]. 80% confluent cell cultures were Trypsin–EDTA solution (Fisher Scientific, 25300-054) and centrifuged at 250 RCF for 3 minutes, and a cell pellet was separated from the supernatant. A 50μL solution of Matrigel to cell media containing cells seeded at a density of 75k cells/ 100μL was released onto the sample and smoothed out to cover all regions using a spatula. Afterwards, the monolayer coating on the surface was scraped away by the spatula and the well was filled with media. The samples were stored in a 40℃ incubator for 45 minutes, then imaged at 20X on a brightfield tissue culture microscope to confirm successful trapping. Cell culture was replenished every 2-3 days until day of fixation and samples were monitored daily. Any observed debris was removed by scraping a pipette tip on the surface.

On the day of fixation, media was aspirated out and the samples were washed with PBS (+/+) once, then incubated in 2% paraformaldehyde in PBS (+/+) in a fume hood for twenty minutes. The samples were then washed twice with PBS (+/+). The plate was wrapped in parafilm and stored at 4℃.

3.3.7 Imaging

Samples were stained with Hoechst at a ratio of 1:1000 (for nuclei), Phalloidin Alexa Fluor™ 555 (Phalloidin Labeling Probes; Invitrogen, A34055) at a ratio of 1:250 (for actin) if cells

were wild-type, and BODIPY at a ratio of 1:1000 (nonspecific lipid dye for PDMS) and incubated at room temperature for thirty minutes. The samples were washed once with PBS (+/+) and stored at 4℃.

An NL5+ Nikon Ni-E confocal microscope equipped with Micro-Manager software was used for confocal imaging. The brightfield channel on the NL5+ system, the Olympus CKX41 tissue culture microscope, and the ECHO REVOLUTION system was used to acquire brightfield images. 50μL of mounting medium with a refractive index of 1.4 was dispensed on a 40mm glass coverslip to avoid diffraction during imaging. The samples were carefully removed from the wells and inverted onto the coverslip with the patterned side facing down. The coverslip was transferred to the microscope and a 50g weight was applied on top to ensure the sample was close to the glass as possible. The samples were imaged at 10X, 20X, and 60X oil immersion (OI) (1.40 NA) in brightfield, blue, green, and red channels at a step size of 0.7 μm.

3.3.8 Live Imaging

We also explored live imaging setups to assess if high-resolution live imaging is feasible for PDMS microwells. A PDMS holder was designed via CAD programs and 3D printed. The margins of the circular opening on the top of the PDMS holder was painted with a thin layer of UV resin and an 8mm coverslip was carefully aligned with the opening using tweezers. The holder was cured in the UV oven for 90 seconds. In order to meet the volume requirement of the holder, 25cm thick PDMS was fabricated.

All components of the PDMS holder was sterilized by soaking in 75% ethanol for three minutes. PDMS pieces were extracted by a punch, rinsed in DI water, and sterilized as written in earlier sections. The PDMS holder was assembled under sterile conditions. With the aid of tweezers, PDMS was pressed inside the holder, as close to the glass coverslip as

possible. To hold the PDMS in place, a four-legged 3D-printed piece was locked around the notches on the periphery of the holder. Finally, the sample setup was placed on the inside of a 6-well plate with another 3D printed well filler locking it in place.

To image, the well filler was removed and the sample was inverted and transferred to the inside of another 3D-printed holder, ensuring that it aligned with the circular opening at the bottom of the holder. The PDMS microwells were then imaged on the NL5+ system at 10X using both the brightfield and 488 channels.

3.3.9 Image Processing

Images were processed through ImageJ/FIJI software, where the Brightness/Contrast bar was used to enhance image quality for visualization purposes. Afterwards, the vertical cross-sections were obtained through the Orthogonal Z function. For the 3D reconstructions, Dr. Alexandra Bermudez processed the images using the software Imaris. Confocal images are presented in a colorblind-friendly format with channels converted to CMYK instead of RGB.

3.4 Results

3.4.1 Single Cell Trapping

Our PDMS micro-well arrays contain many shapes and aspect ratios ranging from circles to squares to rectangles. Although we opted to fabricate them in our lab and not in a clean room, we still managed to obtain sharply defined wells at high resolution. The environmental and experimental factors that enabled this process included covering the wafers with a lid unless they were inside the fume hood to avoid debris, using cleanroom wipes only and replacing

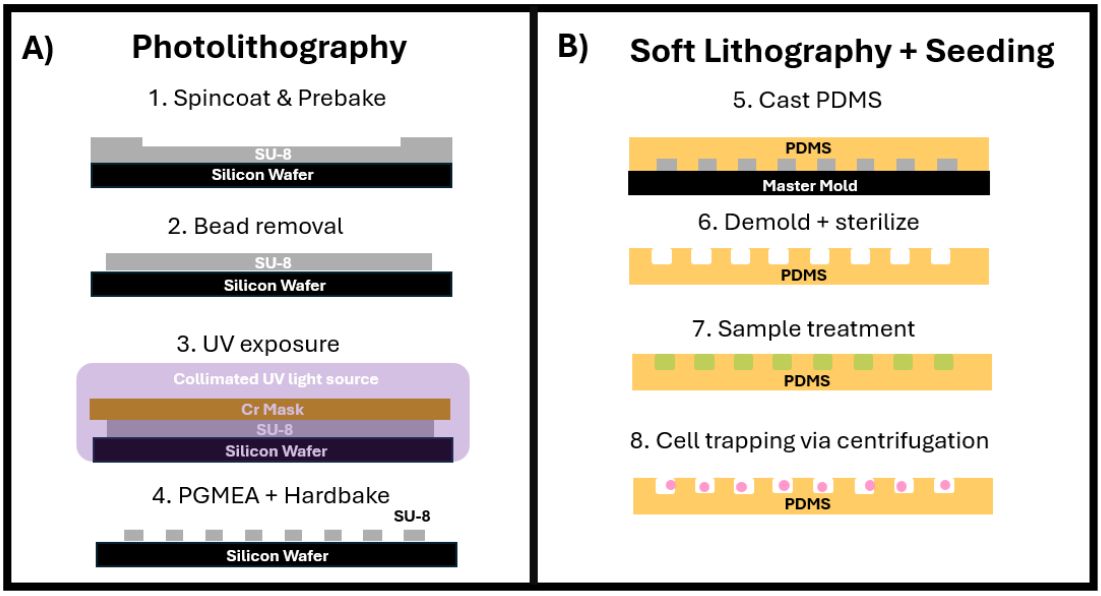

Figure 3.1: Part A shows the photolithography process. SU-8 is spincoated atop a silicon wafer, which is then prebaked to evaporate solvent. After bead removal, a Cr mask is overlaid and the SU-8 is exposed to UV light to initiate patterning and cross-linking. Submerging in PGMEA completes patterning, and the hard-bake enhances structural integrity of the resulting silicon master. Part B describes the subsequent steps. PDMS is cast into the mold and cured, then demolded, sterilized, and treated. Cell suspensions are then seeded and driven into the wells via centrifugation.

them often, removing the edge bead produced by spincoating, and utilizing a collimated UV light source to prevent light from scattering. The process is shown in the schematic Fig 3.1.

To verify viability and success of the PDMS micro-well array fabrication and treatment, instead of regular fibronectin, we coated the PDMS samples with 12.5 μg/mL fluorescein isothiocyanate (FITC) fibronectin via three rounds of centrifugation as described in the methods and examined its silhouette under confocal microscopy. We obtained sharp, clear boundaries along the top and sides which indicated successful fabrication. However, the intensity tapered off towards the bottom of the micro-well, indicating diffraction that reduced SNR (Fig 3.2). This showed us the necessity of measures which reduce the scattering. To overcome this difficulty, we prepared mounting medium which matched the refractive index of PDMS, 1.4, and also a 50g weight that positioned the sample closer to the objective [124]. The schematic is displayed in Fig 3.3.

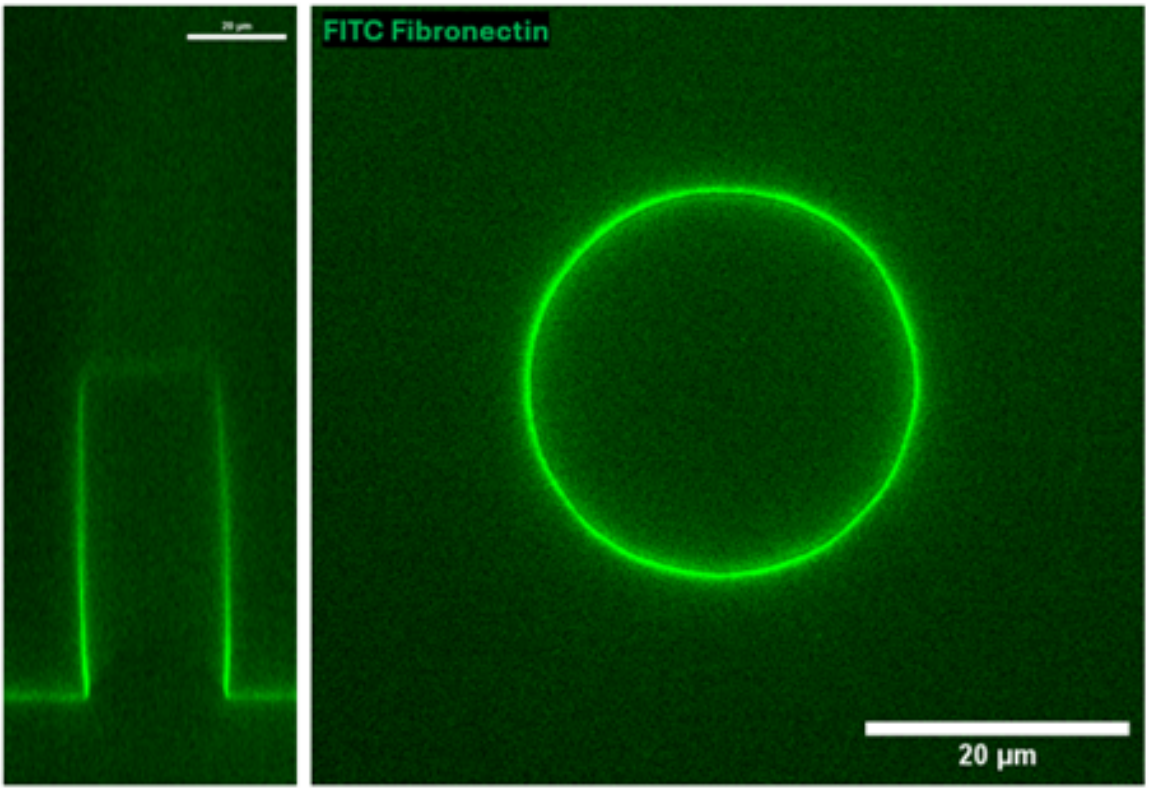

Figure 3.2: A confocal Z-stack obtained of a 20μm diameter cylindrical well coated with FitC fibronectin. Left image represents the orthogonal Z-projection showing the cross-section of the well, which is 50μm deep, while the right image shows the top view, a bright green ring. They demonstrate successful fabrication and sample treatment prior to cell seeding.

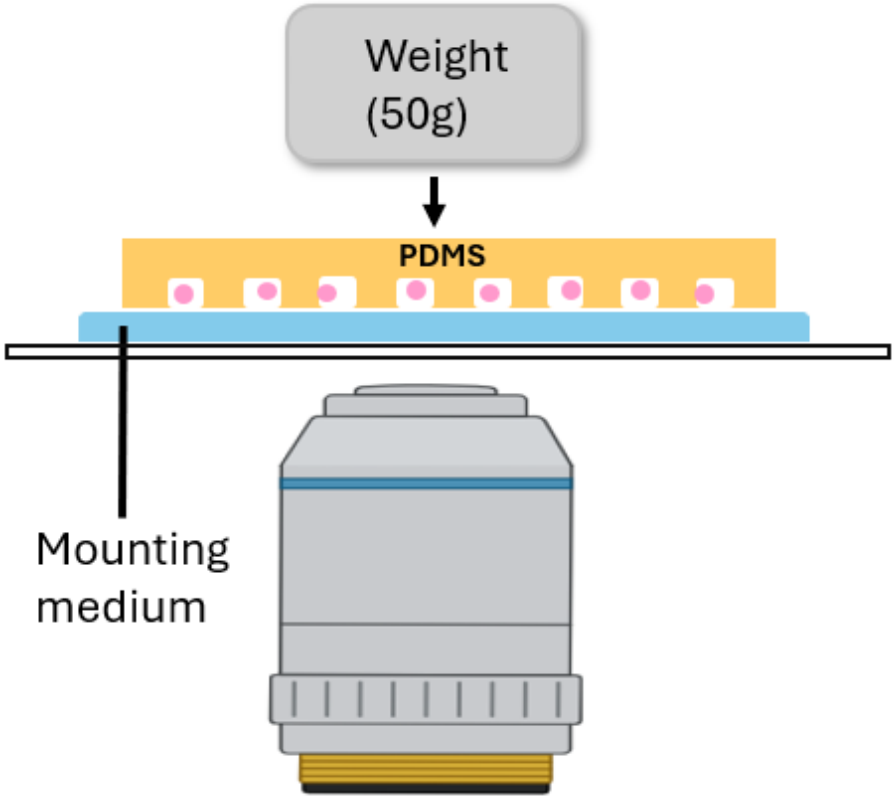

Figure 3.3: A schematic of the imaging setup of the samples is pictured here. The sample is inverted and placed on a coverslip with a drop of mounting medium. A 50g weight is placed on top to bring the sample closer to the glass, and the sample is imaged on an inverted confocal microscope. Created in https://BioRender.com

We also performed a single cell experiment for one of the smallest well sizes, a cylinder below 25μm diameter, to assess the trapping ability of the microwells. As our goal was to assess PDMS microwell confinement capabilities, we focused on the well trapping ratio with the assumption that the cell seeding process yields more than enough cells to fill all the wells. Cells at 30K cells/cm^2 were seeded and centrifuged into the wells. The latter was a necessary step as the small well size prevents cells from sedimenting inside independently. Two hours post-seeding, we confirmed under the tissue culture microscope that each well contained only a single cell (Fig 3.4). Over 120 wells, over 80% of the microwells were occupied.

After 1 day of incubation, the samples were imaged at 60X OI. To maximize SNR, we incorporated mounting medium that matched the refraction index of the PDMS samples, which minimized the scattering we observed earlier as well. However, the mounting medium may not be distributed evenly, causing subtle floating incidents and certain areas of the microwells to be closer or farther from the glass. To prevent unevenness and ensure all fields of view (FOVs) remained within the 60X OI objective's working distance, a 50g weight was applied on on top, flattening the sample against the coverglass (Fig 3.3). The resulting representative Z-projection of the image stack illustrates the ability of the microwells to trap single cells, which shows potential for a variety of applications including sorting and single cell assays (Fig 3.5).

3.4.2 Epithelial Monolayers Experience Defects Under High Confinement

The results of single cell trapping implied that we could apply the strategy to trap higher numbers of cells inside wells by selecting different seeding densities and micro-well dimensions. Therefore, we explored the impacts of different well sizes on monolayer packing to evaluate the role of confinement on 2D epithelial morphogenesis. We define high confinement as wells with sides less than 30μm and low confinement as wells above 90μm long. Our goal was to

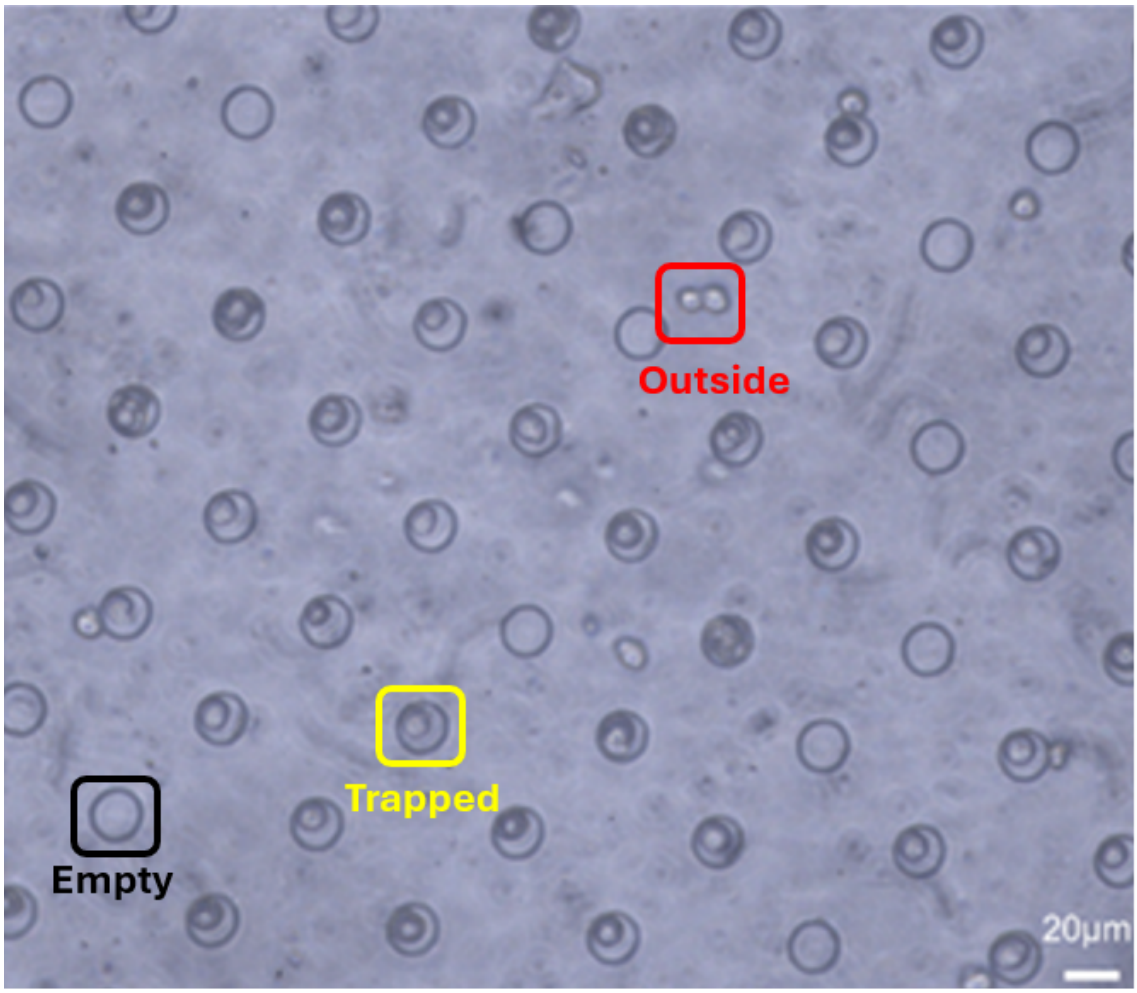

Figure 3.4: A 20X brightfield image showing successful trapping of single cells in 20μm cylindrical microwells immediately after seeding and centrifugation. Most microwells are occupied by cells. The well surrounded by a yellow box denotes a successfully trapped cell, while the cells encircled by red landed on the surface and the black box shows an empty well.

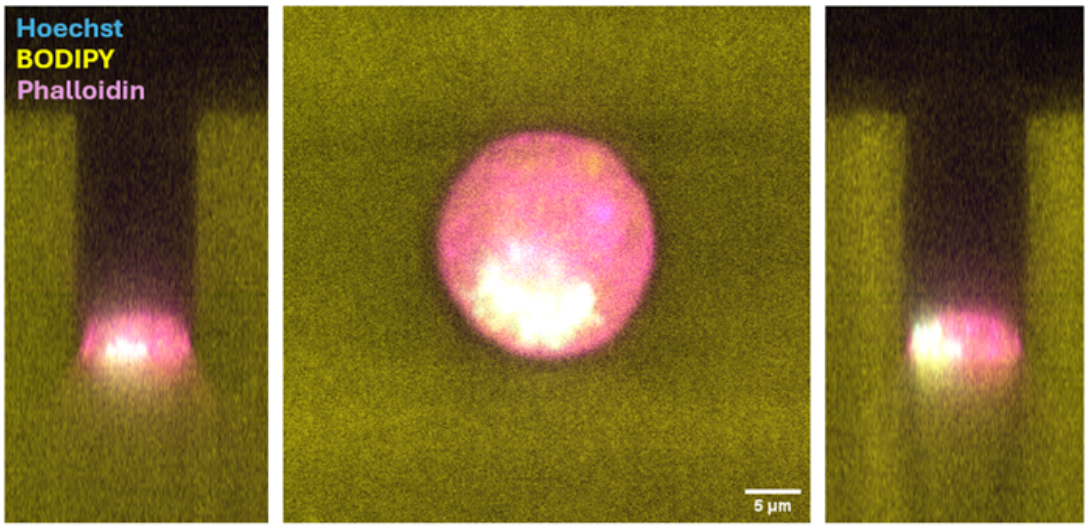

Figure 3.5: A 60X OI confocal image of a single cell maintained in a 20μm PDMS cylindrical microwell for 24 hours. Center image represents the top view of the well, while the left and right correspond to cross-sections in the XZ and YZ planes respecitvely. Cyan structures correspond to the nucleus and magenta is associated with actin and thus overall cell morphology. Finally, the PDMS microwells were stained with lipid dyes and appear yellow in this figure.

observe how epithelial cells seeded into these microwells of varying sizes grew and developed over time. Given that tissue shape often dictates future morphogenetic events, we chose a seeding density low enough to minimize contact between cells centrifuged inside the wells and avoid aggregates from the onset.

For the low-confinement environment, cells were seeded at a density of 30K cells/cm^2 and incubated for 1 day. As shown in the Imaris reconstructions, across the wells, the epithelial cells followed normal monolayer growth and lined every surface (Fig 3.6). This suggests conventional apical-basal polarity, where the basal side faces the adherent surface and the apical side is exposed to the environment [106]. For the high-confinement environment, cells were seeded at 30K cells/cm^2 and incubated for roughly 3 hours, 6 hours, and 1 day. Similar imaging and mounting procedure was followed as described above. At three hours, 2-3 cells were trapped in a well, matching the seeding results, and isolated from each other. However, at 6 hours, instead of cells lining the walls, we observed initial piling, where proliferating cells were stacked on top of each other and formed an epithelial aggregate or multilayers instead of

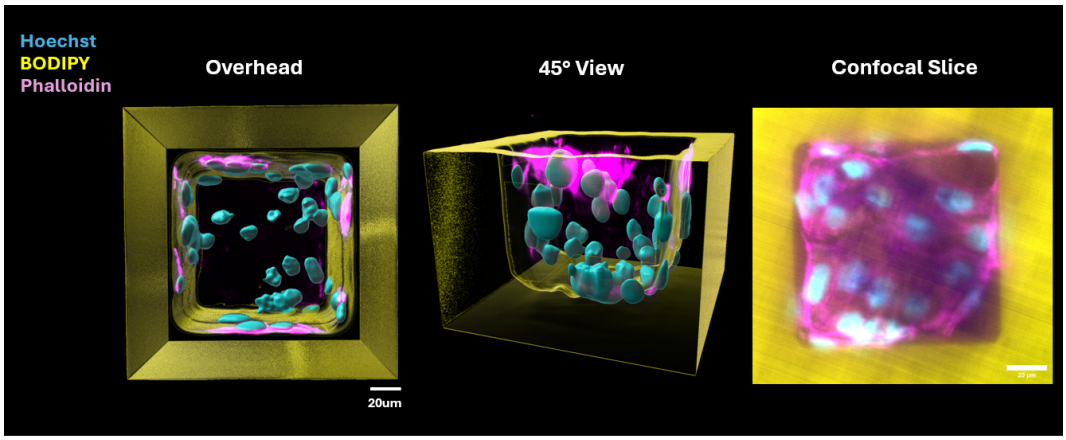

Figure 3.6: A three-dimensional reconstruction of a confocal Z-stack of epithelial cells forming a monolayer along PDMS well topology. Images were obtained through a 60X OI objective. Yellow corresponds to the PDMS microarray paltform, cyan for nuclei, and magenta for actin. The image on the left corresponds to the overhead, XY-plane view, while the image on the middle shows an angled 45° view to illustrate the monolayer behavior of the cultured epithelial tissue. The cells line the walls and the bottom as denoted by the locations of the nuclei. The actin signal is very strong but is weaker at the bottom despite best efforts with the imaging protocol. The image on the right corresponds to a representative slice from the original Z-stack illustrating the cobblestone packing morphology.

spreading out. At 24 hours, the piling patterns continued, although now they occupied more space in the well (Fig 3.7). This was unexpectedly different from the monolayer packing seen in the 90μm microwells. Given the cells stacking on top of each other, particularly for the cells in the middle, it is no longer possible to map the apical and basolateral domains of the cells using simple rules.

It is known that mutated or missing apical-basal polarity mechanisms is linked to the phenomenon of *Drosophila* epithelial cells not polarizing in a single monolayer and instead packing atop each other in a more heterogeneous multilayer [156]. MDCK cells expressing oncogenes were also reported to experience polarity loss that led to multilayer growth [7, 138]. Our experiments paired with the studies conducted on apical-basal polarity defects imply that the constraints imposed by the micro-wells may have led to disruptions of polarity in the epithelial cells, which would explain the presence of multilayer aggregates. One potential mechanism by which the cells formed the multilayer aggregates may be through

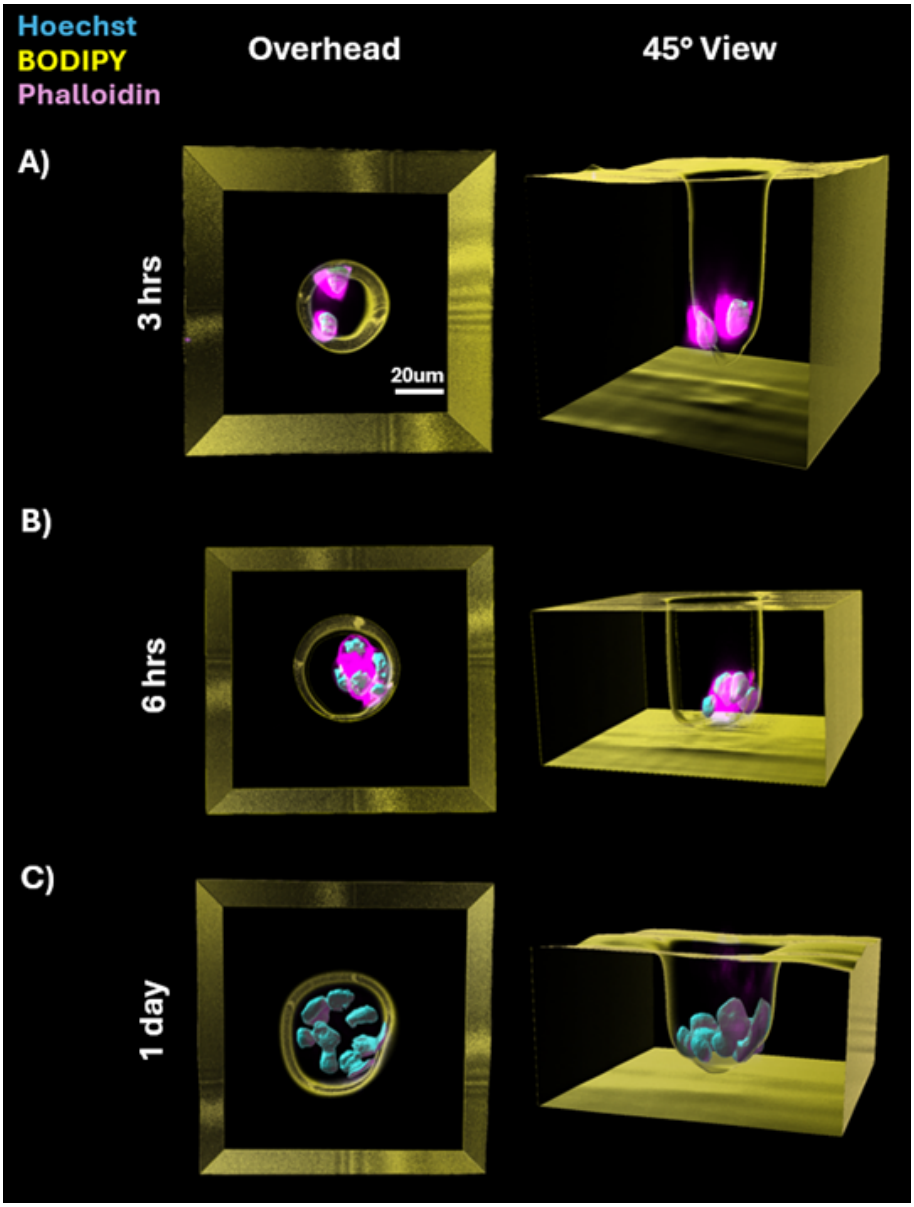

Figure 3.7: Three-dimensional reconstructions of confocal Z-stacks obtained of epithelial cells confined in 20 μm microwells. Images were obtained at (A) 3 hours, (B) 6 hours, and (C) 1 day post seeding via a 60X OI objective. The left column displays overhead views looking into the wells, while the right shows an angled perspective to illustrate epithelial cell behavior against the PDMS walls. Yellow corresponds to the PDMS microarray, and cyan and magenta represent cell nuclei and actin respectively. At three hours, cells resemble status immediately after seeding. At six hours, cells have divided, but do not spread, instead piling on top of each other. After 1 day, more cell proliferation has occurred, but with cells stacking and layering rather than spreading along the well surfaces.

differential extrusion. This is backed by another study that has shown that MDCK cells under confinement will grow to form outer rims through differential extrusions on the boundary of larger two-dimensional chemical patterns [32].

A limitation of the study is the flat value selected for the seeding density for both low and high confinement. The density of the cells that actually enter the microwells may differ due to the size difference in the low versus high confinement. Further experiments to vary the cell seeding density such that the cell trapping density is completely equal may be recommended as an additional control, to promote similarity of initial environment. An interesting side avenue to pursue is how geometric cues impact tissue progression of aggregates. More specifically, if we seeded cells at a sufficiently high density such that they formed clusters instantly, would they remain as aggregates or unexpectedly spread to cover the microwell surface?

Finally, investigation into the mechanism by which the abnormal MDCK growth occurred would be beneficial. We propose incorporation of polarity markers like ezrin, occludins, podocalyxin, and E-cadherin to elucidate the progression of apical-basal polarity establishment as well as more variations of well size to identify the threshold which triggers non-monolayer growth [40,99,163,177]. Additionally, if confinement led to such downstream effects in MDCK monolayers, it may be an intriguing and physiologically relevant research avenue to identify if MDCK morphogenesis is also impacted for three-dimensional structures such as cysts or tubes.

3.4.3 Epithelial Cysts Experience Lumen Deformation Under Confinement

Given the deviations from standard monolayer, cobblestone packing induced by shrinking the well aperture, we hypothesized that three-dimensional structures may experience differences as well. Furthermore, because of the PDMS microwell array's ability to trap single cells, we made

an ambitious step forward towards the three-dimensional realm by evaluating its feasibility at manufacturing trapped epithelial cysts of controlled sizes. Therefore, we conducted an exploratory pilot study on the impacts of geometric confinement on epithelial acini growth and development with the goal of achieving 25% throughput. Instead of wild-type MDCK cells, we utilized an MDCK-LifeAct cell line, where fluorescent actin genes were transfected into the MDCK genome. This enabled regular confocal imaging of the cells' morphology and structure over time, which is crucial to epithelial morphogenesis of cysts. Cells in 10% Matrigel were seeded at 75k cells/100 μL and centrifuged into micro-wells, then incubated and monitored daily. Our objective was to survey the wells and identify if geometric constraints and morphogenetic variations were linked. As a control, we also followed the progression of acini growth on the unpatterned regions of PDMS above the wells.

Microwells were imaged using 20X to record the overview of acinar progression. A majority of the microwells exhibited no cyst growth and was either empty or contained an aggregate, which we define as a cluster of cells with neither lumen nor clearly defined shape (Fig 3.8) . For wells that successfully cultured cysts, the time from initial seeding to acini filling the micro-well varied, but on average wells were filled within 6-8 days, with earliest and latest time points of fully confined acini recorded at 4 days and 11 days respectively. Unconstrained acini on the surface acted as a control which determined if the PDMS microwell array could successfully sustain three-dimensional epithelial culture. They were observed to form aggregates and circular shapes with varying diameters that exceeded well dimensions in some cases, ranging from below 50 μm to above 200 μm radius, due to the lack of limitations imposed by microwells (Fig 3.9). The conventional cyst growth showed that the PDMS microarray culturing platform did not create any unwanted, adverse impacts on epithelial cells.

Despite showing success at individual trapping cases, its main weakness was throughput, which was both low and varied significantly between sample to sample. No overarching

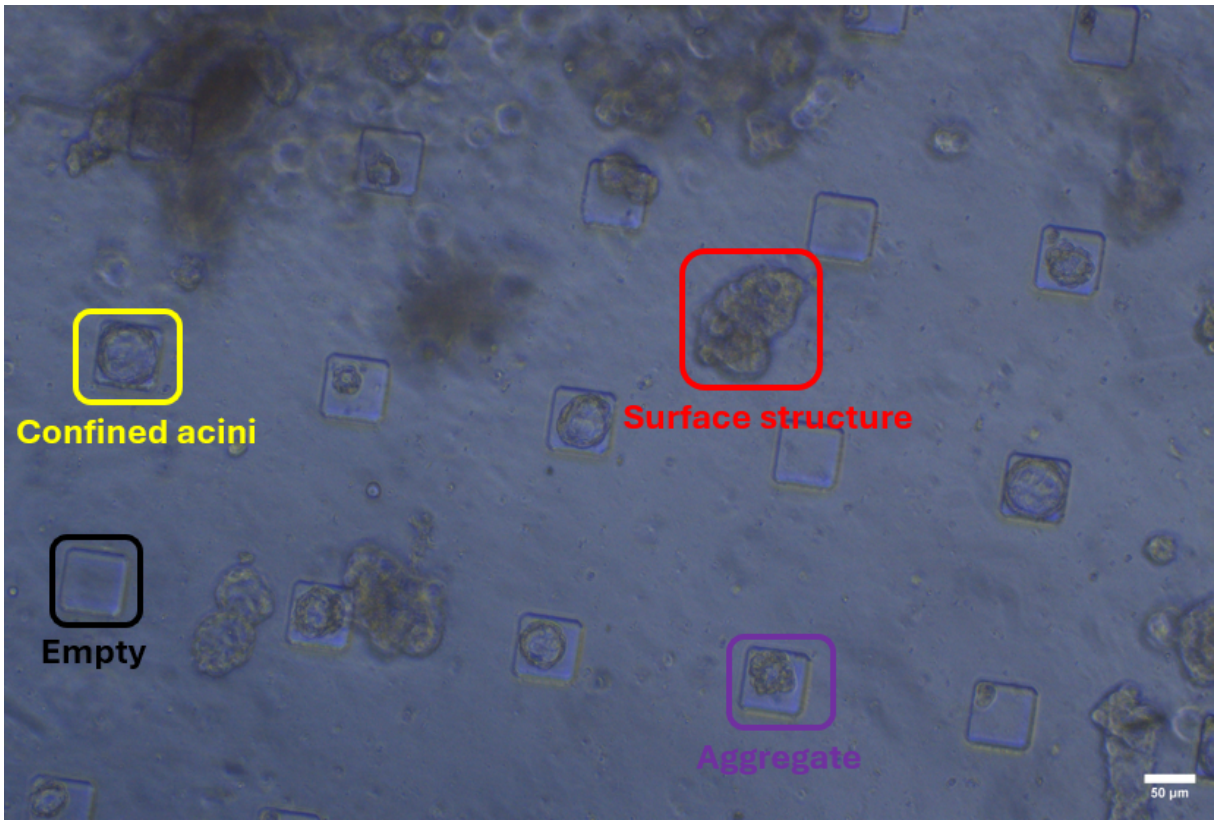

Figure 3.8: 20X brightfield image of epithelial Matrigel suspensions grown in 60 μm wells confinement for 4 days, exhibiting the earliest case of successful acini trapping. The figure shows a image of a PDMS microarray structure with epithelial structures growing on the surface as well as epithelial acini trapped in the wells at varying sizes and levels of confinement. A yellow box encircles a trapped acini, a black box marks an empty PDMS microwell, a red box illustrates an example of an unconfined surface structure, and the purple box demonstrates an example of a multicellular aggregate.

patterns or correlations associated with culture length or microwell size were drawn from the data, with cyst production ratios falling between 5% to 25% in a single FOV. Across the 300 wells observed the overall percentage of wells containing acini was 10%. This is much lower than the 80% reported for single cell trapping in conventional epithelial culture, and the 25% throughput we aimed for. The discrepancy may be partially explained by the material properties of Matrigel. Although it provides the matrix support needed to grow three-dimensional cysts, Matrigel is dense and stiffens easily [143]. For this reason, cells mixed with Matrigel are likely to experience more difficulties in the sedimentation and microwell entry process, particularly if the wells are small. The ratio gets whittled down further during process of generating cysts as not every confined cluster of cells polarizes with a lumen. Further refinement of trapping and fabrication processes may further boost the rate of epithelial cyst trapping.

We also explored the impact of well topology and Matrigel density, both of which mimic the matrix microenvironment for epithelial tissue. While we generally observed expected circular acini formation in 60 μm squares at 10% Matrigel, for cultures in larger squares, different aspect ratios, and/or higher Matrigel concentrations, cases of deviation from textbook acinar development were identified. To further examine their morphology at greater detail, the wells were imaged at 60X OI. An epithelial cyst cultured in a rectangular well exhibited compressed cells for the sides interacting with the PDMS, while the other perimeter cells were rounded. The lumen itself was slightly squashed due to the presence of the walls, but the morphology of the outer layer of cells was dissimilar to the well shape, forming a sphere instead of cylinder, with cells experiencing heterogeneous force levels (Fig 3.10).

In larger, 100μm wells, with 25% Matrigel, we noticed two intriguing phenotypes: multicyst or multilayer structures which deviate from standard cyst growth. In Fig 3.11, a large epithelial cyst is surrounded, not only by a monolayer, but by multiple layers of cells around the basal region. The acini exhibits multilayering as observed for the two-dimensional packing under

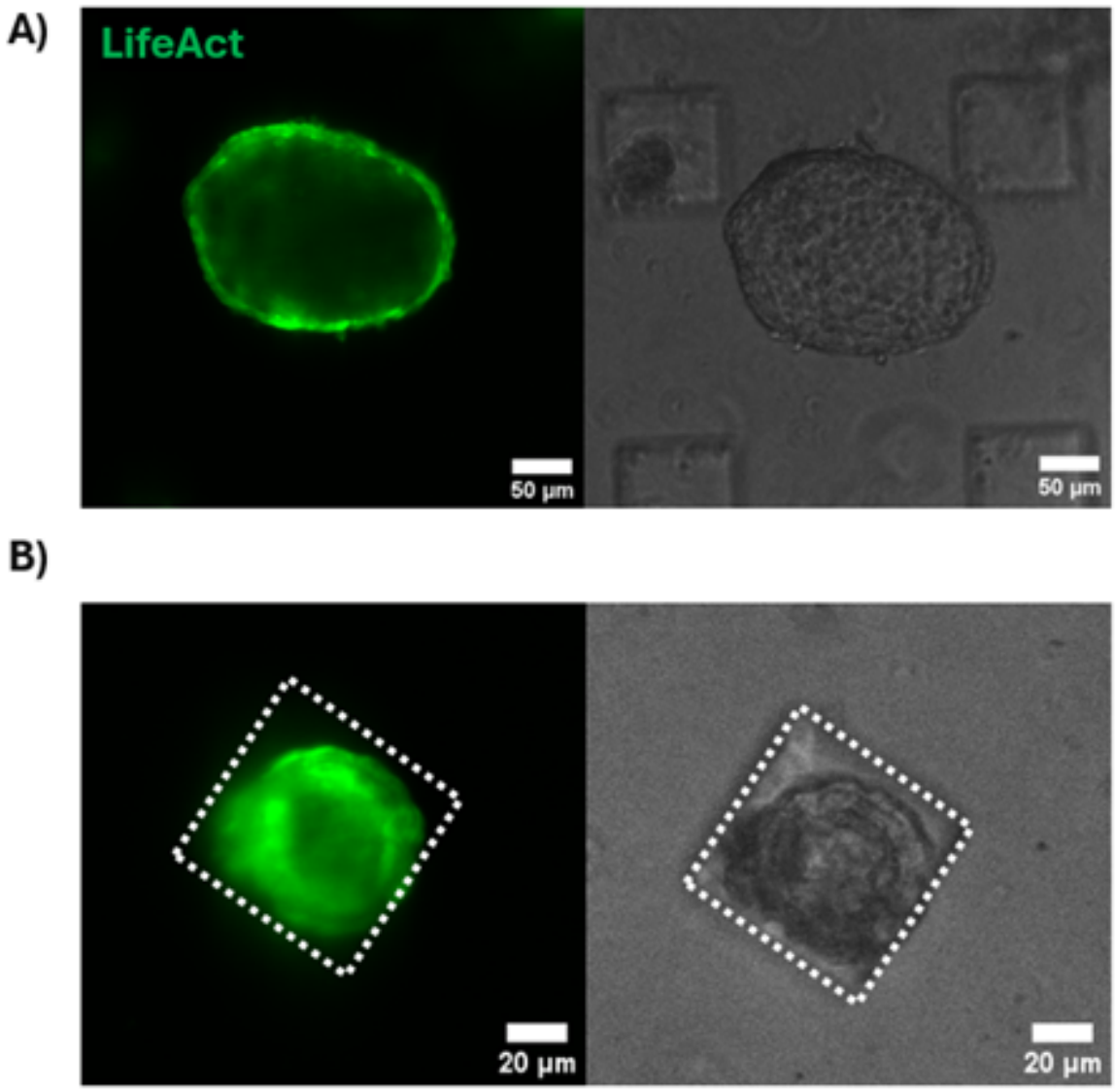

Figure 3.9: Representative acini images from Matrigel culture at the 8-day timepoint are pictured here, with images obtained at 10X brightfield as well as the 488 channel corresponding to actin. (A) shows an unconfined acini on surface which spans a diameter of roughly 200 μm. (B) displays an epithelial cyst constrained within a 60 μm square.

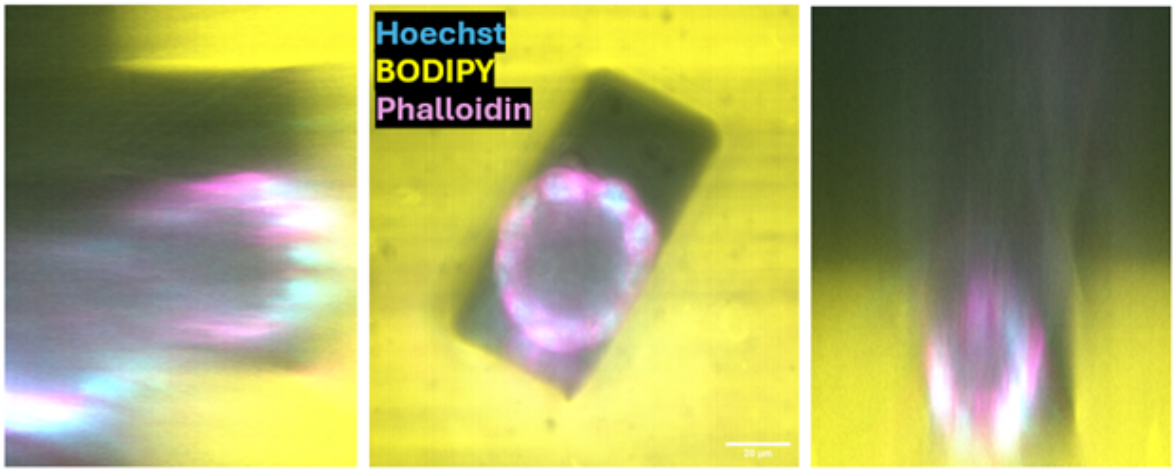

Figure 3.10: This figure shows a confocal cross-section of a 70 x 140 μm rectangular microwell with an epithelial acini growing inside, surrounded by orthogonal YZ- and XZ-projections showing vertical cross-sections from left to right respectively. The images were obtained at 60X OI, and after 6 days of incubation. The cells growing against the walls look flatter and more compressed compared to the cells that do not touch any walls.

high confinement. It also appears to have linked to epithelial cells lining the surface of the PDMS environment, thereby forming what resembles a hybrid 2D-3D epithelial culture analogous to *in vitro* development of colonic crypts [166]. In Fig 3.12, at least two clearly defined lumens were observed. Depletion of the polarity protein atypical protein kinase C (aPKC) is linked to multilumen generation, and loss of its regulator Cdc42 causes disconnected lumen in intestinal epithelia [28, 135]. The cyst in Fig 3.12 may have shown deviations from conventional apical-basal polarity, but the simpler explanation of two acini growing adjacent to each other may suffice. MDCK multilumen structures like this acini have been reported to share similar structures with dutal carcinomas in breast tissue [31]. Given the relationship between apical-basal polarity and cancer, investigating the mechanisms behind the polarization of this structure and identifying potential signs of dysfunction may contribute to insights towards the formation of tumors.

These examples suggest that 100μm wells or greater, equipped with stiffer Matrigel environments, could provide the space which can sustain long-term growth of epithelial

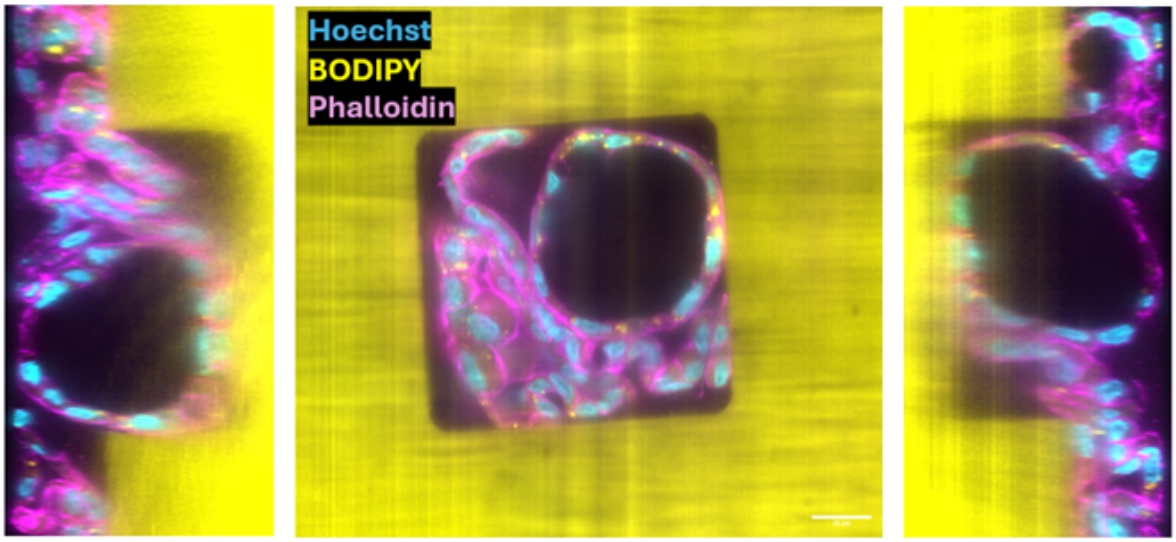

Figure 3.11: This figure shows a confocal cross-section of a 100 μm square microwell with a complex epithelial structure growing inside, surrounded by orthogonal YZ- , XY-, and XZ-projections showing vertical cross-sections from left to right respectively. The images were obtained at 60X OI, and after 10 days of incubation. Epithelial cells from the surface appear to have entered the microwell and potentially merged with acinar cells. The epithelial cyst also displays a non-monolayer structure with stratification of cells occuring along the sides.

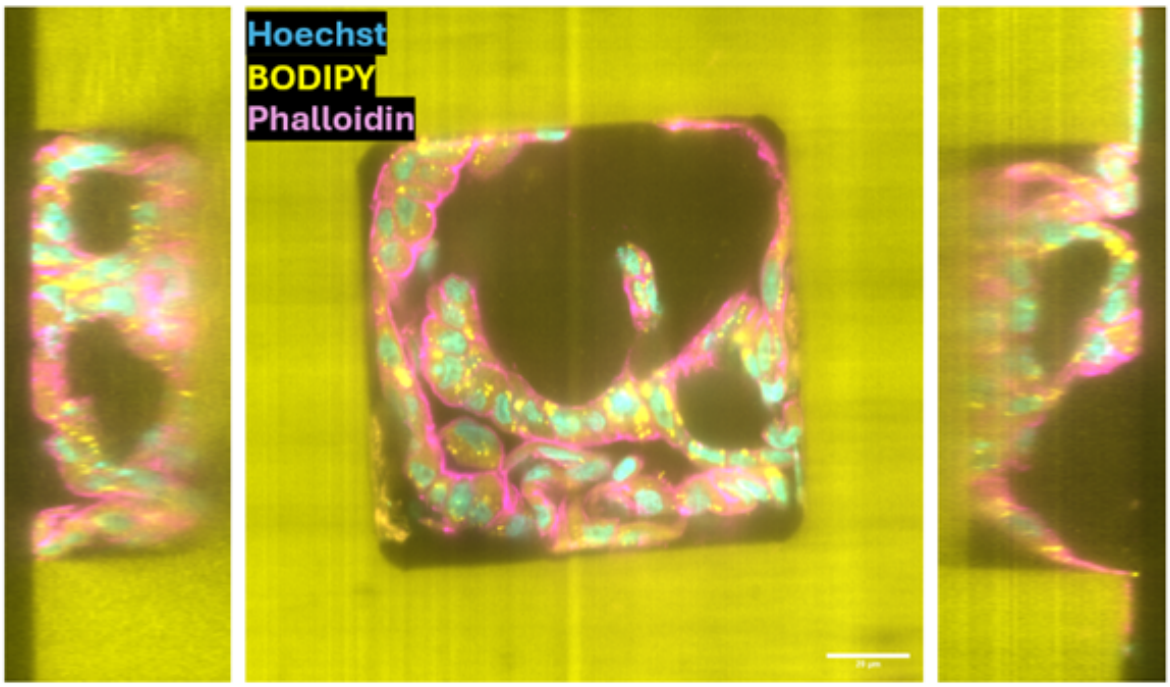

Figure 3.12: This figure shows a confocal cross-section of a 100 μm square microwell with a complex epithelial structure growing inside, surrounded by orthogonal YZ- , XY-, and XZ-projections showing vertical cross-sections from left to right respectively. The images were obtained at 60X OI, and after 10 days of incubation. In the bottom half of the well, the epithelial cells have formed a structure that resembles cysts with at least two lumens contained, and is linked to further extensions of epithelial growth.

structures more complex than a monolayer fluid-filled shell. The manufacturing of multilumen and multilayer cysts can aid biomedical research because they exhibit phenotypes with downstream influences on cancer progression and tissue development. Additionally, wells with more varied topology can also impose geometric constraints on selected regions of epithelial cysts, allowing for direct comparison of the effects of geometric cues on tissue development. Therefore, these microwells have shown potential to explore multiple research avenues for three-dimensional epithelial culture: the generation of geometrically homogeneous epithelial cysts for drug assays, the modeling of epithelial stratification under confinement, and the investigation of the relationship between physical cues, and lumenization and apical-basal polarity development.

3.4.4 3D-Printed Sample Holder to Facilitate Live Imaging

One challenge of live imaging epithelial structures growing in microwells is the distance between the objective and the cells. The PDMS sample lies with the microwells facing up, so the working distance and light emitted need to accommodate both the plastic of the well plate as well as the PDMS before finally reaching the region of interest. Obviously, magnifications of higher than 20X cannot be reached, and SNR may be sacrificed. Additionally, inverting the PDMS for 60X OI imaging can destroy sensitive epithelial cysts due to the mounting procedure, most notably the weight.

Therefore, to explore progression of epithelial cysts further at high magnification, we developed a 2-part PDMS holder along with a well insert and a sample container for imaging. The PDMS holder consists of the holder itself, which was designed to snugly hold a cylinder of PDMS with 21mm diameter and 4mm thickness, with a coverglass window, two rectangular openings beside it to facilitate pipette entry and media exchange, and notches around its circumference. It is paired with a four-legged compressor with a 3.6mm central tube that applies mechanical pressure to the PDMS to minimize the spacing between the microwells and

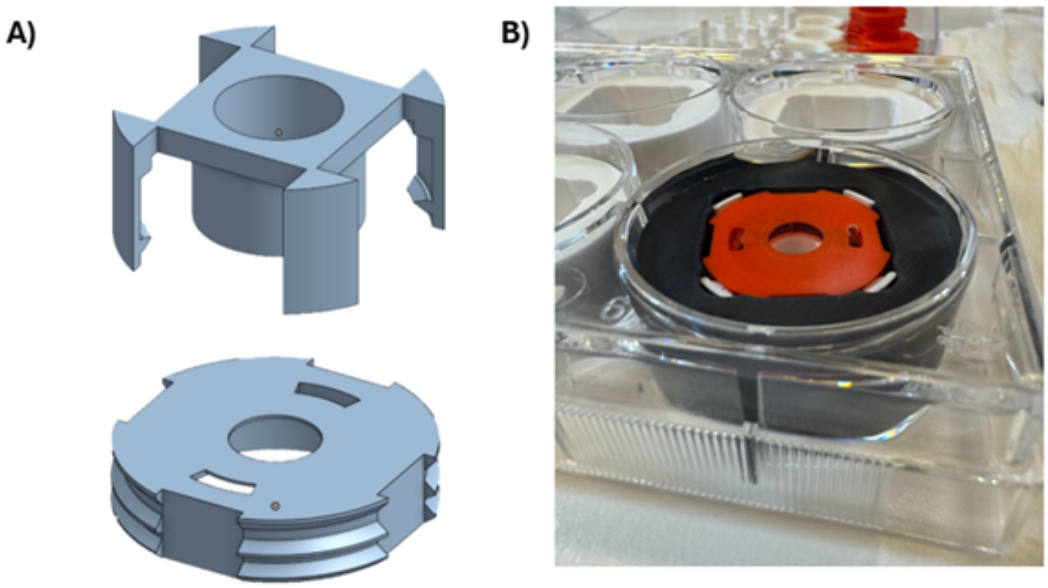

Figure 3.13: Part A illustrates the CAD design of the 3D-printed PDMS holder, while part B shows an example of the parts assembled together in a 6-well plate, along with the well insert. The red piece corresponds to the cap, the small white rectangles match the legs locking around the holder, and the black ring fills the well to minimize cell medium required.

window Fig 3.13. When combining the vertical size of the compressor and holder itself, the height of the overall setup is large. Hence, when placed inside a 6-well plate, this indicates the necessity of a significant, costly amount of cell medium to maintain cultured acini. Therefore, we incorporated a cylindrical well insert, which functions as well filler to minimize amount of medium consumed (Fig 3.13). Finally, the sample container resembles a lid and a slide insert which can store the PDMS sample, with a small opening at the bottom (Fig 3.14).

Unfortunately, the holder device did not work as effectively as we had anticipated. Although cells could initially be cultured and formed aggregates inside at a density of 150K/100 μL and 5% Matrigel as shown in Fig 3.15, we experienced various, currently insurmountable issues ranging from insufficient Matrigel entry into the microwells as well as lower cell health and viability despite varying seeding and Matrigel-related parameters. Combined with the inability to reach magnifications higher than 10X as well as the complexity of sample handling and maintenance, we opted to focus on other objectives such as basic

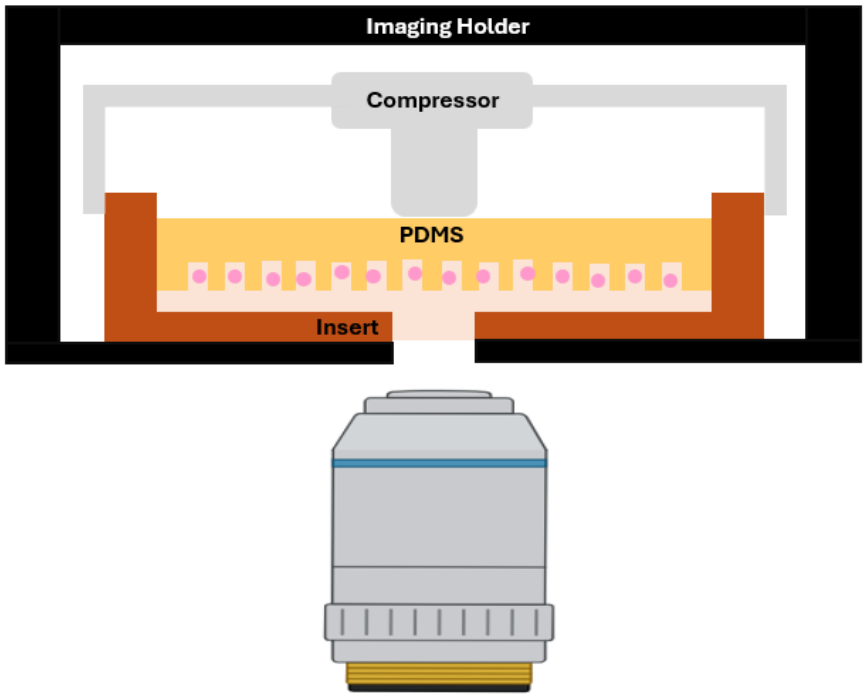

Figure 3.14: A schematic showing the live imaging setup. The PDMS microwells with cells and medium is inverted and wedged into the red PDMS holder, held into place by the white compressor. To prevent outside contamination, the sample is stored in a slide insert which is placed above the objective. Created in https://BioRender.com.

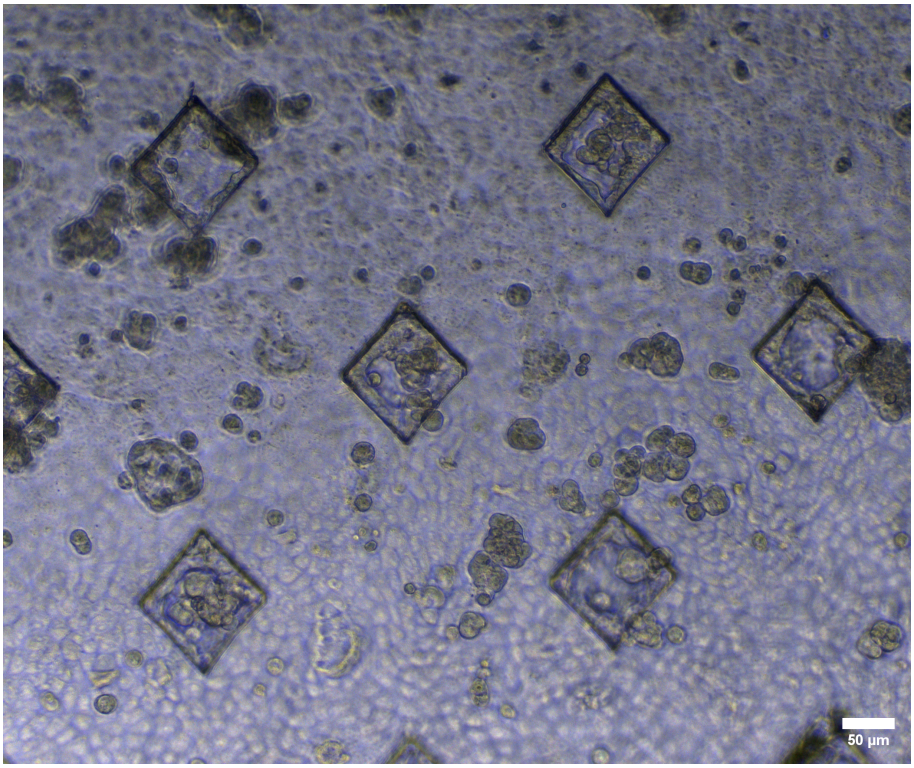

Figure 3.15: A 10X brightfield image of PDMS microarray contained in a 3D printed device designed to facilitate live imaging. The image was obtained by ECHO Revolution microscope after incubation for almost 1 day. Cells grow on both the surface and inside the 100 μm wells, forming aggregations and monolayers.

throughput and impact of geometric cues on lumenization.

3.5 Conclusion

We developed PDMS microwell imaging strategies to further facilitate research into the effects of geometric confinement on biological systems. One major challenge in PDMS microwell confinement assays is obtaining confocal microscopy at high SNR, which we overcame by applying imaging strategies like utilizing mounting media that match the index of refraction of the sample and reduce scattering. We explored a low-cost live-imaging setup comprised of 3D-printed inserts for the PDMS samples. Although we encountered difficulties with managing working distance, limiting our imaging to 10X magnification, we succeeded in devising sample

holders that can allow for quick transport between the confocal microscope and the well plates. Refinement of the design and materials may lead to actualized live-imaging experimental protocols.

Through these microwells, we were able to explore the impact of the mechanical microenvironment on epithelial organization and potentially apical-basal polarity. We showed that smaller microwells and thus high confinement is correlated with epithelial piling instead of expected monolayer growth. For three-dimensional epithelial structures, we also observed instances of compressed luminal development as well as potential multi-lumen structures and epithelial stratification, further underscoring the mechanobiological impact of geometric confinement on apical-basal polarity. In the future, we anticipate that these microwell arrays can serve as platforms with which to monitor epithelial tissue growth and track the trafficking of apical-basal polarity proteins to further explore our hypotheses.

Chapter 4

Computationally efficient segmentation of complex tissue structures in brightfield images

4.1 Overview

Organoids and other three-dimensional structures like acini are excellent biological models with which to recapitulate *in vitro* tissues for broad biomedical applications ranging from drug testing to tumor development. Pipelines that capture morphological properties of organoids through segmentation in order to answer key biological questions are needed, but because deep learning models with many parameters dominate segmentation performance, many require high-computing environments and consume significant resources during training. We first review performance of a curated selection of segmentation models against Cellpose cyto2, then explore the effectiveness of synthesizing the results derived from the best-performing models for two challenging segmentation tasks: organoids with acircular morphologies and organoids confined in engineered microwell arrays, which introduce imaging artifacts.

4.2 Introduction

Three-dimensional organoid culture has increasingly grown more prevalent in biomedical and bioengineering research due to their ability to capture the *in vivo* environment more closely [146]. Organoid images contain key properties of tissue behavior like viability and shape changes over time for studies in drug development, morphogenesis, and more [46, 75]. Therefore there has been an uptick of image data of organoids, increasing the need for assays and image analysis pipelines [95]. Particularly in morphogenesis studies, many properties of organoids require quantitative measurements of size, aspect ratio, and circularity. However, hand-segmenting organoids is a very time-consuming, resource-intensive task, driving a need for automated segmentation pipelines.

There have been a number of segmentation software released over the years, most famously Cellpose for more general identification of biological structures [145]. More specialized organoid-specific softwares include OrgaSegment, OrganoSeg, MOrgAna, OrgaQuant, OrganoID, POST, and more [17, 45, 73, 86, 98]. With the exception of OrganoSeg, which used adaptive thresholding, most models are trained on a deep learning framework, as algorithms like convolutional neural networks and U-nets have proven themselves particularly successful for image segmentation compared to more traditional image processing algorithms like thresholding or edge detection filters [160]. This would indicate that training models generally require computers with graphic processing units (GPUs) at the minimum. However, not everyone has access to a cluster or machines equipped with GPUs. Additionally, most models are trained on datasets of circular organoids and do not contain aspects that complicate segmentation. Examples of such images include images with uneven lighting, organoids with irregular shapes, and culture conditions that introduce artifacts, like the presence of microfluidic devices [73].

Potential strategies to apply to fill these gaps with reduced resource cost include transfer learning and hybrid models. Transfer learning applies pre-trained models to another related

application, oftentimes adding or unfreezing a few layers during training [157]. Transfer learning is a more resource-friendly process and may work well for specific tasks like the images listed above. Hybrid models fuse classical and deep learning segmentation algorithms to boost performance or efficiency [71]. Aligning with our goals of limiting ourselves to CPU usage, we hypothesize that leveraging and combining multiple segmentation models with different strengths and weaknesses into one pipeline can allow for breakthroughs in highly specific and challenging subsets of organoid datasets.

First, we conducted comparative analysis on several pre-trained segmentation models to identify the best performers based on varying metrics on a standard organoid dataset based on the assumption that models that perform poorly on circular segmentation cannot be relied on for more complex morphologies. Then, we proceed to select the top two performers and develop a segmentation pipeline that generates the masks, identifies as many correct masks as possible from both models, and produces a final output with the union of the best segmentations on an external dataset with atypical organoid morphology. Second, we also propose a boundary-aware pipeline to overcome imaging artifacts introduced by engineered arrays, which consists of first identifying array dimensions with one segmentation model, then inpainting the raw image, and finally segmenting the pre-processed brightfield pictures. All steps in the process are performed on computers equipped only with central processing units (CPUs).

4.3 Methods

4.3.1 Prostate Organoid Culture and Drug Experiment

The experiment was performed by James Lo and we used the brightfield images obtained. Patient-derived xenograft organoids (PDXO 180-30) cultured in 6-well plates and embedded

in a ring of Growth Factor Reduced (GFR) Matrigel (Corning Growth Factor Reduced Matrigel, CB40230C) were obtained and treated with dispase to induce dissociation. The dispase was dissolved in human prostate organoid medium (HOM) at a concentration of 2mg/mL. Incubation lasted between one to two hours, or until disaggregation of the organoids was observed under the Olympus brightfield microscope. The dissociated organoids were then centrifuged to allow for cell sedimentation, and the resulting supernatant was aspirated. The cell pellet was suspended in fresh HOM. The cell count was determined through the cell counter Countess to identify the volume of suspension needed. The desired amount of cells was aliquoted and re-suspended at a 7:1 volume ratio of Matrigel. Prior to the procedure, Matrigel was thawed overnight at 4 °C over ice.

One droplet of 500 cells mixed with 5uL Matrigel were seeded per well in a 96-well plate. The Matrigel was cross-linked by leaving the plate for half an hour in a 37 °C tissue culture incubator. Afterwards, 60μL HOM was added to each well. The samples were maintained for 21 days at 37 °C and 5% CO_2 in a tissue culture incubator. Every 2-3 days, the medium was replaced with fresh HOM warmed to room temperature to replenish nutrients. The samples were imaged daily on the ECHO Revolution epifluorescence microscope using Olympus 4X objective, TRANS channel, and exposure of 3 milliseconds with a 5MP CMOS Color camera.

On day 21 of culturing, the organoids were imaged on ECHO Revolution as described above and treated with enzalutamide to initiate drug treatment. Stock enzalutamide at a concentration of 100mM in dimethyl sulfoxide (DMSO; Millipore Sigma, 67-68-5) was diluted through two-fold serial dilution to desired concentrations. Wells not involved in any experiment were filled with phosphate-buffered saline (PBS) to minimize evaporation.

The HOM was aspirated from the wells and replaced with 80uL drug solution of enzalutamide diluted in DMSO. The plate was incubated at 37 °C, 5% CO_2, and approximately 90% humidity in a tissue culture incubator for 6 days. After three days, to replenish the drug and nutrients, half of the medium was removed and replaced with corresponding enzalutamide

solution. Similarly to the organoid culture phase, the samples were monitored and imaged daily on the ECHO Revolution microscope. After six days of incubation, the viability of the organoids was assessed by performing the CellTiter-Glov 3D assay and following the associated protocol.

4.3.2 Comparative Analysis of Varying Segmentation Models

We took 4 fields of view (FOVs) from day 0 and day 6 of the drug experiment. To expedite segmentation, we also shrank image dimensions to a maximum of 1024x1024 pixels. We segmented both the raw and processed versions using OrganoSeg2, OrganoID, OrgaSegment, POST, and Cellpose 2.0. We generated our ground truths through hand-drawn segmentations in Cellpose software, which included out-of-focus organoids. Our model used the evaluation pipeline developed by OrgaSegment, where we identified if an organoid was segmented or not by calculating the Intersection over Union (IoU) the mask areas to the ground truth mask areas [86].

We then calculated the average precision based on number of correctly segmented organoids over the IoU threshold. To evaluate ability to correctly identify organoid boundaries, we filtered only for true positives and determined the Pearson correlation of the mean circularity, and average symmetric distance between the predicted and ground truth segmentations. To test tracking ability and segmentation consistency across different time stamps, we used OrgaSegment's tracking function to trail organoids across all models and calculate the Pearson correlation of the fold change over the two time points.

4.3.3 Enhanced GPU-Free Segmentation

Our work is based off the brightfield organoid images from the figures in Dixon and colleagues' paper on polycystin proteins on kidney epithelial organoids as a prototype [35]. The ground

truth was obtained by hand segmentation. We fed the images through OrgaSegment and Cellpose and obtained masks, which can be converted to Python arrays where different numeric indices are associated with different segmentations, with 0 standing for background. From the results, we identified matching masks similarly as in the comparative analysis, but instead examined the ratio of overlapping area to the area of the smaller mask. OrgaSegment masks matched to multiple Cellpose masks were isolated for further processing.

Now that we had matched the smaller Cellpose segmentations to the larger OrgaSegment, we generated approximate organoid boundaries using a Canny edge filter. We eroded the OrgaSegment generated mask with a 6x6 kernel and identified if the approximate boundaries overlapped with the shrunken mask. If less than 30% of the contour points overlapped with the eroded mask, this indicated that OrgaSegment had encapsulated more than one organoid in its segmentation. Otherwise, this suggested that Cellpose had failed to segment more complex structures and that the set of segmentations associated with OrgaSegment needed to be merged.

Combining occurred by altering the mask arrays such that the masks to be merged were assigned the same index value. They were added to the collection of masks common to both OrgaSegment and Cellpose. As the merging process likely causes a non-linear sequence of indices, the indices were reset, with each mask being reassigned a new index ranging from 1 to the total number of masks. We assessed the results against the ground truth by applying the metrics average precision and average symmetry distance as described above and compared the performance of the combined model, OrgaSegment only, and Cellpose only.

4.3.4 Microwell-Aware Segmentation Pipeline

We used the brightfield epithelial cyst images obtained as described in Chapter 3. The images were fed through OrgaSegment to obtain masks. The average mask area was set as the

threshold with which to filter out small, non-square masks. Contours were obtained from the masks, and corresponding pixels on the raw image were processed via OpenCV's Telea inpainting algorithm [154]. The inpainted images were then segmented by Cellpose's cyto2 algorithm. For model evaluation, they were compared against masks obtained only through Cellpose by calculating average precision, recall, and symmetry distance as described above.

4.4 Results and Discussion

4.4.1 Selection of Best-Performing Organoid Segmentation Models for Images with Irregular Lighting

Out of all the available models, we selected OrgaSegment, OrganoID, POST's TinySAM, and OrganoSeg2 as these models could run inference on a CPU. Additionally, Cellpose (cyto2) was chosen as baseline performance to evaluate the models against. The dataset we chose was derived from an drug testing experiment on prostate organoids (Fig 4.1). Our goal was to identify different strengths and weaknesses of the models, so we utilized a variety of metrics—average precision to determine how capable the algorithm was at identifying in-focus, out-of-focus, and shadowy organoids, average symmetric distance to identify how closely the segmentation boundaries matched the ground truth, correlation coefficient of circularity to calculate how effective the model was at capturing general shape, correlation coefficient of fold change between images taken one week apart to evaluate tracking ability. Models that performed well would demonstrate an aptitude to correctly segment as many organoids as possible despite nonideal imaging conditions, thereby maximizing image data output.

To test organoid detection, first, we matched predicted organoids to the ground truth through an Intersection over Union (IoU) criteria as described in the methods and plotted

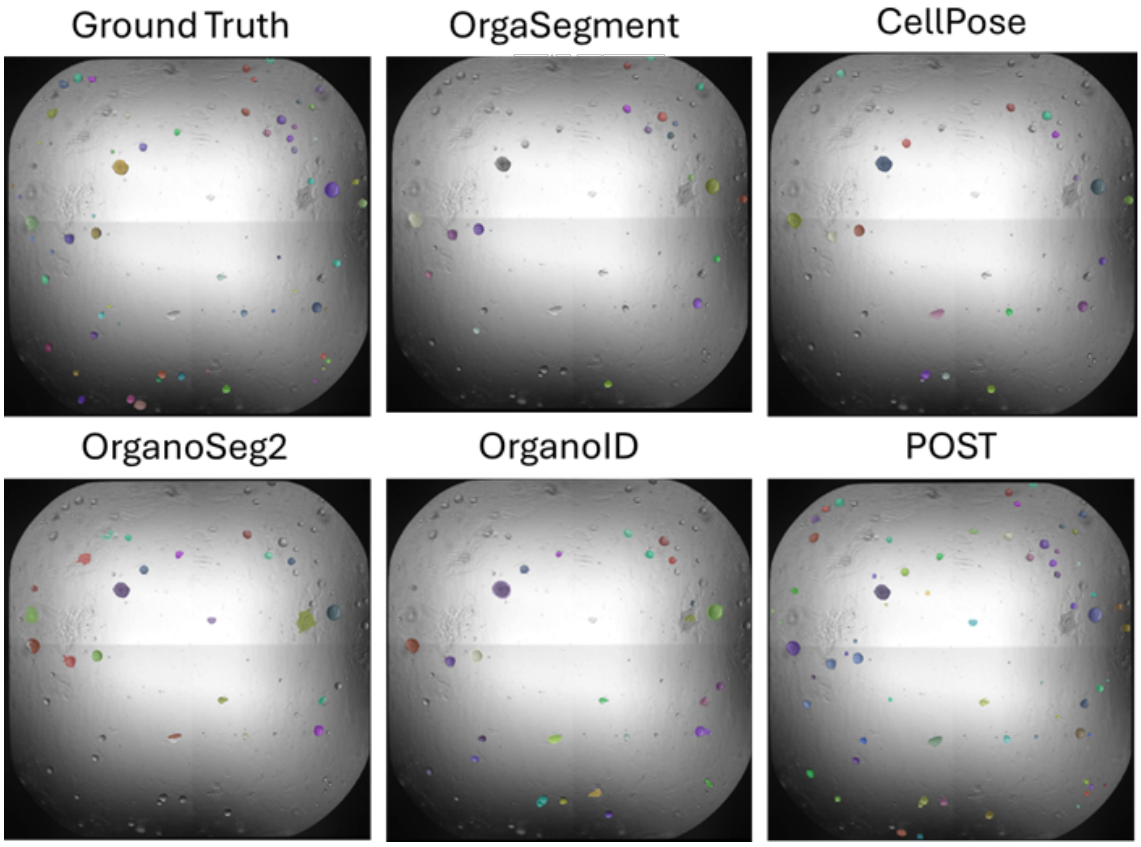

Figure 4.1: Segmentation of representative brightfield PDX organoid images with dark corners. These images were obtained immediately after seeding for the prostate cancer drug experiment. From left to right, top to bottom, the images features the ground truth (hand-drawn), OrgaSegment, Cellpose (cyto2), OrganoSeg2, OrganoID, and POST segmentations. The images were generated by overlaying the masks over the raw images in Cellpose.

the derived metrics as described Lefferts. et al. [86]. Using the numbers of correctly identified organoids, background instances marked as organoids, and organoids left unlabeled, we calculated the average precision and recall over varying IoU thresholds and generated graphs to observe their performance (Fig 4.2-4.3).

OrgaSegment and Cellpose performed very well for average precision, with values of above 0.8, but dropped a large amount for recall. This indicated they rarely mislabeled background as organoid but also missed many real organoids. OrganoID followed similar patterns as the other two, but with weaker performance. OrganoSeg2 had the worst results, showing the limitations of classic segmentation algorithms compared to deep learning models for challenging imaging datasets. Interestingly, POST showed medium, but more consistent performance across both, suggesting that it struck a balance between selectivity and inclusivity when classifying pixels as background or organoid and a strength at identifying out-of-plane organoids, which is historically noted as challenging [73].

We also assessed model ability through other metrics. First, we calculated circularity, which is defined by 4π multiplied by the area over the perimeter squared. Circularity describes how round a shape is, with a value of 1 denoting a perfect circle. For organoids both the model and ground truth identified (IoU threshold > 0.3), we calculated the Pearson correlation between their mean circularities per well (Fig 4.4). This allowed us to evaluate how effectively models could capture basic morphological properties. Cellpose's cyto2 model appeared to perform with highest consistency while OrganoID was weakest. Overall, there was little correlation between ground truth and predicted circularity.

We also examined the ASD, which computes the difference between segmentation boundaries, to investigate model ability to successfully capture unique morphological details of the organoids (Fig 4.4). The smaller the ASD the better the model. Cellpose and OrgaSegment performed best, with lowest distances, while OrganoSeg performed extremely poorly. POST's TinySAM model followed with the second-highest ASD. Speculations for the reason

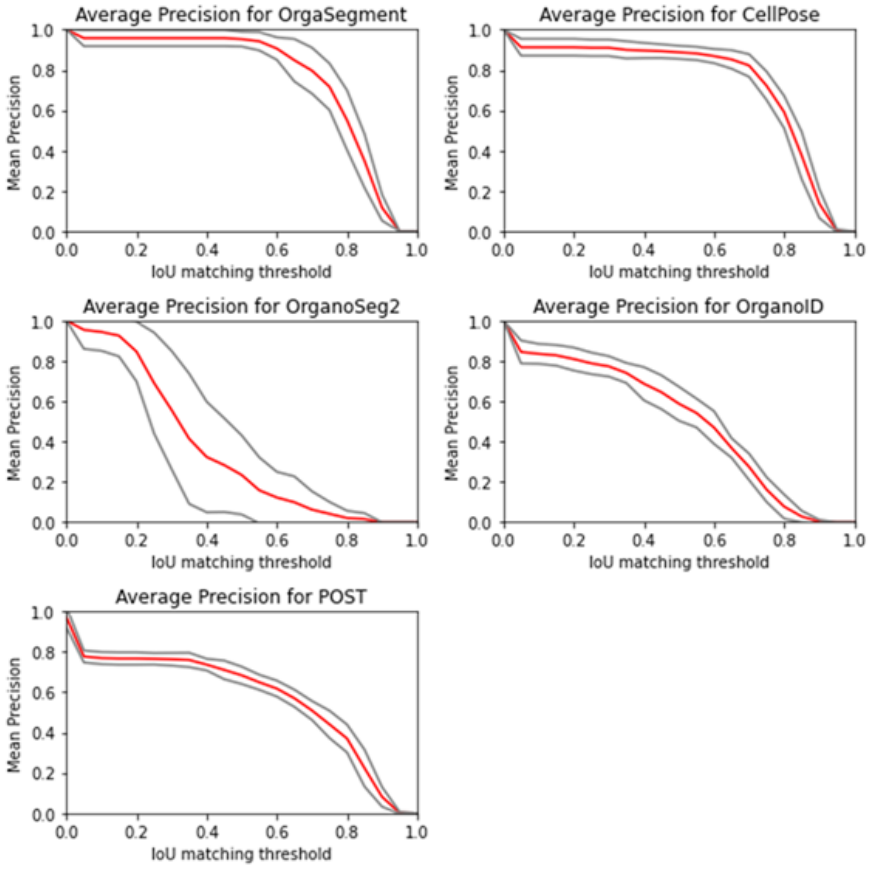

Figure 4.2: Average precision of the models were calculated based on numbers of organoids detected. A true positive, or organoid detection, was identified by calculating overlap between ground truth and model segmentations and determining if it met an overlap threshold. A false positive was any organoid segmented by the model with no matches against the ground truth. The plots demonstrate mean precision over IoU thresholds spaced over 0.1 between 0 and 1, with red lines corresponding to the mean and gray to the standard median.

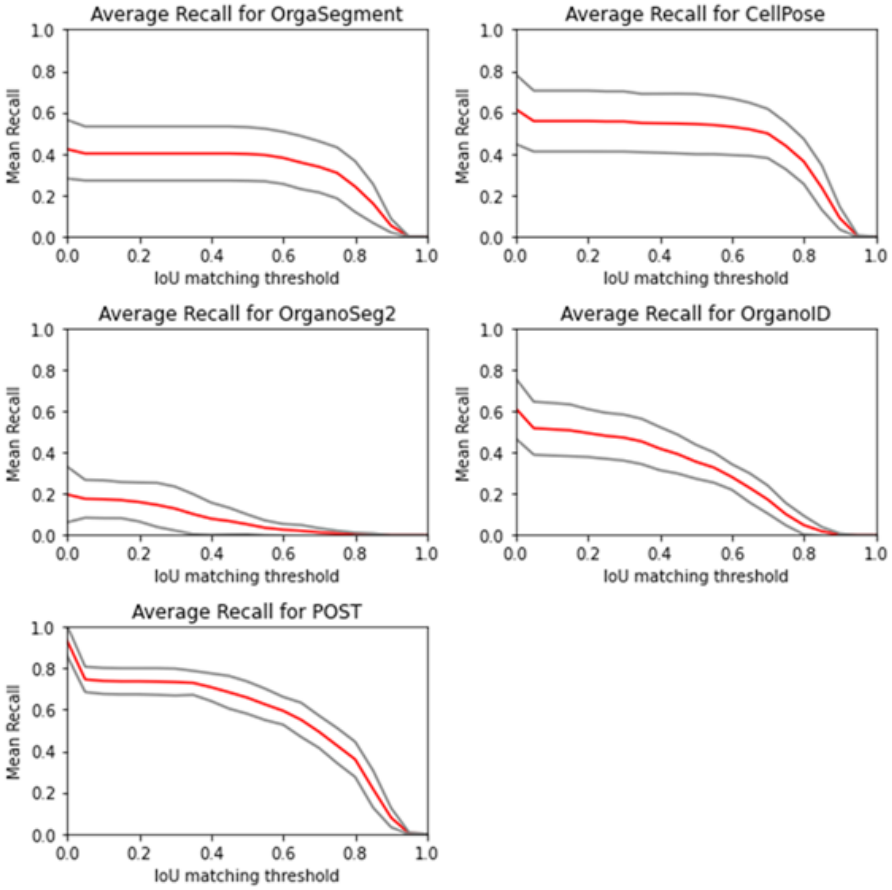

Figure 4.3: Average recall of the models were calculated based on organoid detection. A true positive, or organoid detection, was identified as described in Figure 4.2. A false negative was any organoid segmented by the ground truth with no matches against the predicting model. The plots demonstrate mean precision over IoU thresholds spaced over 0.1 between 0 and 1, with red lines corresponding to the mean and gray to the standard median.

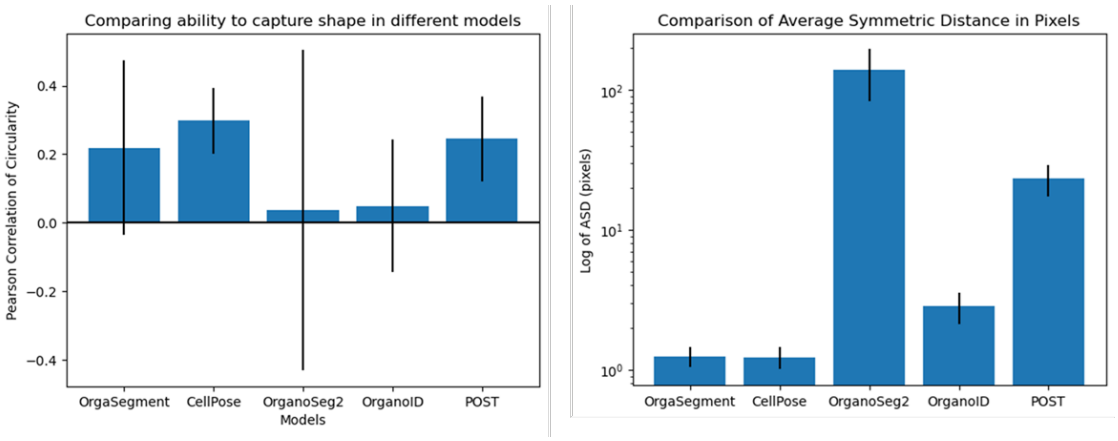

Figure 4.4: Bar plots describe morphological assessments of model segmentations. Left plot compares the Pearson correlations of the circularity of the predicted versus ground truth segmentations. Right plot compares the logarithm of average symmetric distance between the borders of the predicted versus ground truth segmentations. The error bars correspond to standard deviations.

	OrgaSegment	Cellpose	OrganoSeg2	OrganoID	POST
Correlation	0.990	0.968	0.516	0.904	-0.099

Table 4.1: Pearson correlation of fold changes determined by tracking of ground truth and the associated model. The fold changes were determined by generating a dataframe of the coordinates and centroid of the organoid and feeding it to OrgaSegment's tracking function. The mean fold changes from each well was compared against the fold changes from the ground truth using Pearson correlation.

include poor model performance at actually identifying boundaries and resolution limitations when hand-segmenting smaller organoids using Cellpose software, which may have led to an imperfect boundary delineation for the ground truth.

Finally, as the dataset provided images at different time points, we explored tracking ability. OrgaSegment performed best, followed by Cellpose while POST performed the worst, displaying no correlation (Table 4.1). Overall, while not always the top performer, this showed that OrgaSegment and Cellpose performed consistently across all metrics and is thus the most reliable. The other three models tended to be weak across, or strong in particular metrics.

4.4.2 Applying OrgaSegment and Cellpose on Irregular Organoids

Among all the tested models, OrgaSegment and Cellpose performed particularly strongly for ASD. Therefore, we aimed to further explore their performance for organoids with more complex structures, such as PKD model organoids. Our initial observations led us to hypothesize that Cellpose was stronger at object identification, while OrgaSegment was better at contour identification. We then further hypothesized that a combined OrgaSegment-Cellpose model would improve segmentation performance. Below is our exploratory design of a post-segmentation pipeline that synthesizes their strengths and reduces their weakness based on the hypothesis that a model collecting the best results from both Cellpose and OrgaSegment would improve segmentation performance. We harnessed the dataset from Dixon et. al's work on PKD organoids [35].

First, from five FOVs, we collect segmented masks from Cellpose and OrgaSegment, then pair organoids to each other based on area ratio overlap, instead of IoU, which does not account for segmentations with significant size difference. Multiple Cellpose masks matched to one OrgaSegment mask were collected as this suggested a potential complex shape. To evaluate if OrgaSegment or Cellpose was correct, we applied a Canny edge filter to capture approximate boundaries. We also eroded the OrgaSegment mask to shrink it and confirm if it crossed the contours detected by the Canny operator. If it didn't, it indicated that OrgaSegment's mask was correct and the multiple Cellpose masks were merged. Otherwise, the Cellpose masks were not merged (Fig 4.5). Pictured in Fig 4.6 are representative examples of the segmentations performed by each experimental setting compared against the ground truth.

After performing this series of steps, we evaluated their performance using average precision and recall as well as average symmetry distance (ASD). OrgaSegment showed best mean precision, while the combined model and Cellpose were stronger for recall (Fig 4.7). Bar plots comparing and contrasting ASD across varying organoid morphological types were generated.

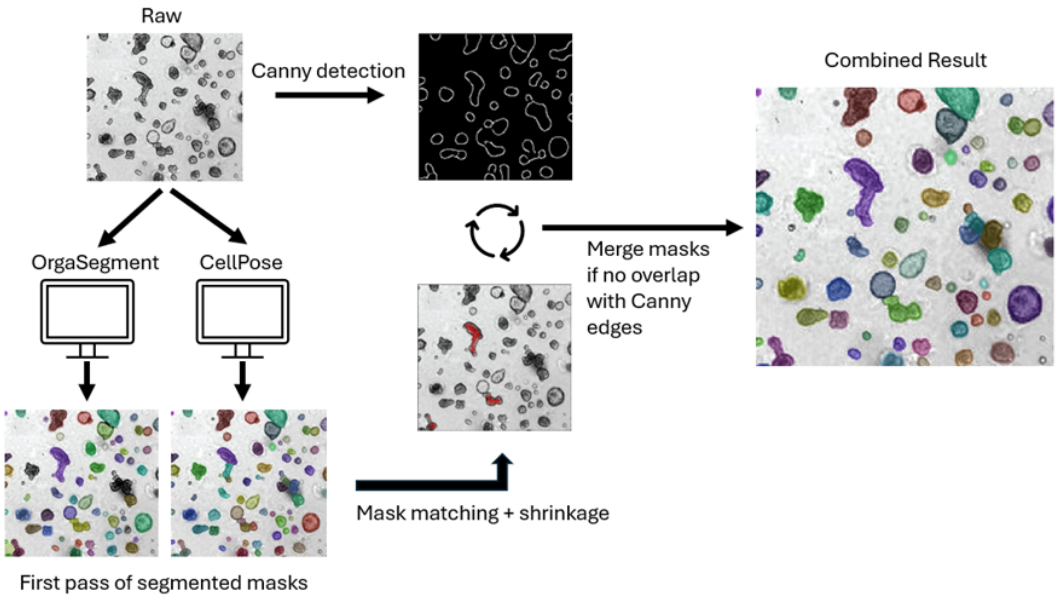

Figure 4.5: A schematic showing the combination process of fusing both models. First, masks are generated using OrgaSegment and Cellpose cyto 2. OrgaSegment masks with multiple matches to Cellpose masks are isolated and shrunk. Canny detection is applied to the raw image. If the Canny edges and shrunken masks intersect, the associated Cellpose masks are merged, leading to the final result. Images were reprinted from the brightfield picture data in Dixon et. al [35].

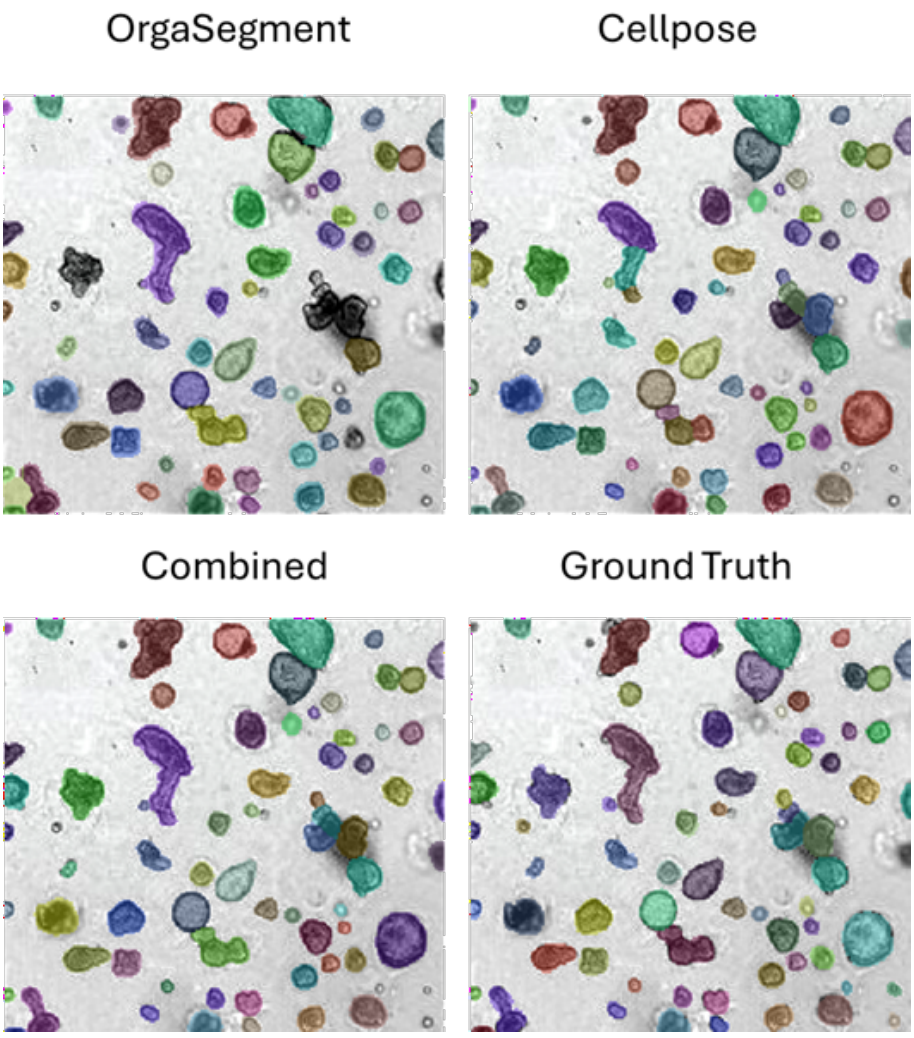

Figure 4.6: The figure shows side-by-side the performance of only OrgaSegment, only Cellpose cyto2, and the combined process against the ground truth (hand-segmentation) from left to right, top to bottom. Images were derived from the brightfield picture data in Dixon et. al [35]. Masks were overlaid atop the raws in Cellpose's software environment.

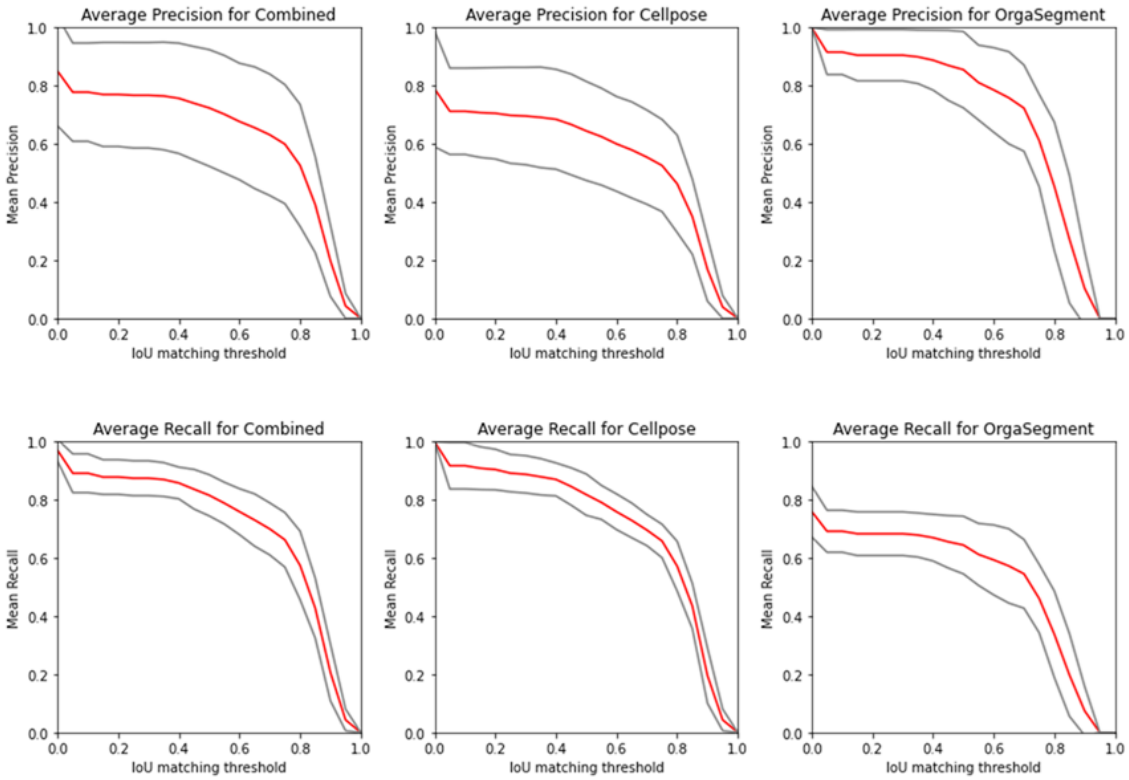

Figure 4.7: Average recall and precision of the combined, Cellpose-only, and OrgaSegment-only models were calculated based on organoid detection, as described in earlier figures. The plots demonstrate mean precision and recall over IoU thresholds spaced over 0.1 between 0 and 1, with red lines corresponding to the mean and gray to the standard median.

Statistical significance was detected only for the cases examining Cellpose or combined versus OrgaSegment ($p=0.03$ and $p=0.02$ respectively), demonstrating that Cellpose was better than OrgaSegment at segmenting round shapes and that the combined model was able to meet Cellpose's standards. For all organoid shape types and irregular organoids, ASDs trended lower for the combined model compared to CellPose, hinting at potential positive effects of incorporating segmentation information from Canny operators and OrgaSegment (Fig 4.8).

However, the pipeline shows a number of weaknesses. First, the decrease in ASD and increase in performance delivered by the model is not significant. Second, OrgaSegment's weakness is a lower recall and occasional inability to identify organoids that should be segmented. Potential other strategies to incorporate are ensemble strategies which incorporates other deep learning models or preprocessing strategies that brighten the organoids and increase

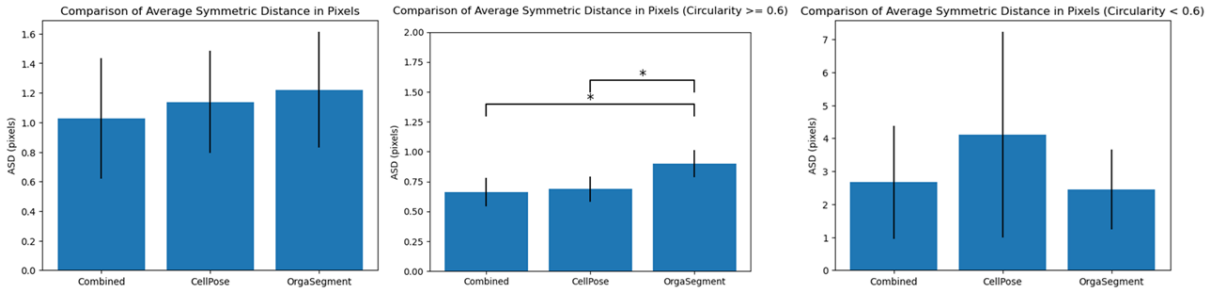

Figure 4.8: Bar plots comparing the combined model, Cellpose-only, and OrgaSegment-only results, which describe the ASD across all organoids, circular organoids (circularity greater than 0.6), and irregular organoids (circularity below 0.6). Statistical significance, or a p-value greater than 0.05, was observed only for circular organoids when comparing the combined model and Cellpose versus OrgaSegment. Error bars denote standard deviation across the FOVs.

OrgaSegment's recall. Despite these limitations, we recommend this method for users focused on segmenting irregularly shaped tissue structures and characterizing their morphology.

4.4.3 Applying OrgaSegment and Cellpose on Structures in Engineered Microenvironments

Another subfield of segmentation, which has been explored comparatively less, involves recognition of non-biological boundaries, which is necessary in order to successfully segment structures grown in microfluidic devices. If segmented without any preprocessing, softwares are prone to ignore the biological structures and instead highlight the artifacts left by the topology of the microfluidic platform. Like with acircular organoids, we hypothesized that combining pretrained models, namely Cellpose cyto2 and OrgaSegment, with other algorithms could aid highly specialized segmentation tasks without the use of GPUs. More specifically, we aimed to first identify microwell boundaries, reconstruct the images as if the boundaries did not exist, then segment the structures.

For our dataset, we leveraged 5 FOVs of 20X brightfield images from the epithelial acini experiments described in the prior chapter. The images were chosen to contain non-blurry

organoid images with minimal amounts of surface image artifacts or other epithelial acini that may add noise to model performance. The ground truth was obtained through hand-segmentation, and the baseline, or controls to compare against, were segmentations via Cellpose cyto2 without additional pre-processing for minimum performance Fig 4.9.

The microwell-cognizant pipeline is as follows. First, the image squares are identified by processing through OrgaSegment, because OrgaSegment's recall is lower than Cellpose's, which indicates increased likelihood to only segment microwell boundaries and not surface acini. While an alternative strategy is to use classical edge detection filters and combine them with user-inputted information on the geometric parameters, delegating this task to a pre-existing segmentation model promotes generalizability. The pictures obtained may be taken at different magnifications, which influences the parameters, and the sample may be positioned during imaging such that the microwells appear rotated, complicating well identification.

To ensure acini would not get accidentally processed, we also set the average mask size within one image as the minimum threshold. All masks which fell below the threshold, which were likely to be cysts and not squares, would be eliminated by setting to zero. New masks for inpainting were generated by elucidating mask contours and redrawing them. Utilizing those masks to pinpoint the microwell edges as regions of interest, we then processed the original images to replace the PDMS well boundaries with pixel values that more closely matched the surroundings, reducing its high contrast and thus its likelihood of unwanted, erroneous segmentations. As the objective is to replace microwell boundaries with the equivalent of the image background, standard processing algorithms like Gaussian blurring or mean filters are not sufficient. Instead, we employed the inpainting Telea technique, which is part of a class of algorithms that specializes in image restoration and reconstruction. Based on user inputs denoting images as containing thick or thin boundaries, the program will correspondingly adjust inpainting parameters. The inpainted images were then segmented by Cellpose cyto2

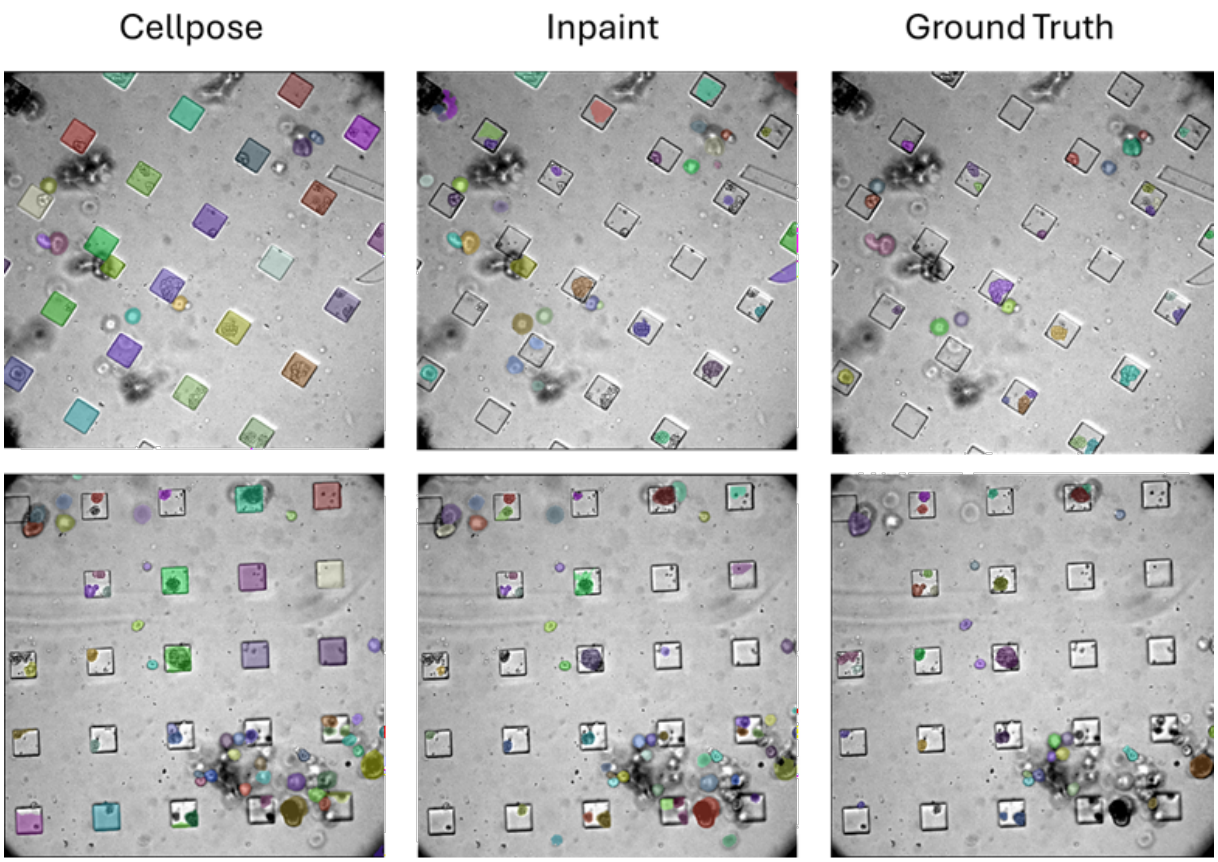

Figure 4.9: This figure compares two representative FOVs of the Cellpose cyto2-only pipeline, the microwell-aware inpainting segmentation pipeline, and the ground truth side by side from left to right respectively. The images were generated by overlaying the masks on the raws using Cellpose software. When relying only on Cellpose, microwell boundaries appear more likely to be segmented than the epithelial cysts and aggregates inside.

and their performance was compared against segmentation without any preprocessing as baseline Fig 4.10.

Average precision and recall were similar, but the inpainted version showed more stability Fig 4.11. Additionally, while the difference in ASD was not statistically significant, the bar plots suggest a downward trend Fig 4.12. With further refinement of inpainting and microwell boundary identification, the ASD can be reduced. One of the limitations is OrgaSegment's lower recall, which can cause it to miss some squares. Additionally, traditional inpainting algorithms are powerful, but not as much as diffusion models, which may better capture

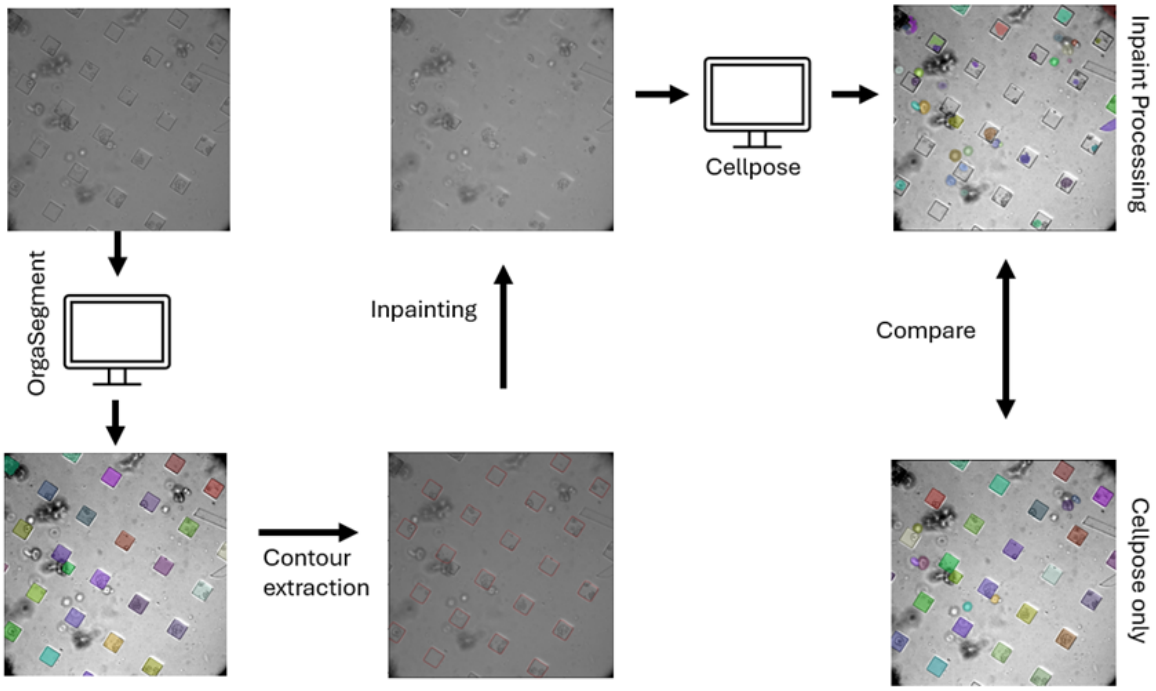

Figure 4.10: This schematic describes the process of segmenting epithelial cysts while minimizing the cases of microwells being segmented instead. First, microwells are identified by OrgaSegment. Then contours are extracted and inpainted to replace microwell boundary lines present in the image. Finally, the processed image is fed to Cellpose cyto2 to generate final segmentations and is then compared to Cellpose results from raw, unprocessed images.

background pixel distribution and apply them appropriately to microwell boundary regions. Finally, this model requires the image to be segmented twice, which can reduce processing efficiency.

4.5 Conclusion

From multiple segmentation softwares targeted towards organoid growth, we selected pipelines that could be run on a CPU to minimize resource cost. By conducting basic machine learning and morphological analysis and comparing performance to the baseline model Cellpose cyto2, we observed that most models did not meet baseline imposed by cyto2. However, OrgaSegment managed to perform at a comparable level. When we explored segmentation of irregularly shaped organoids from an external dataset, OrgaSegment showed stronger aptitude at matching organoid boundaries. Therefore, we combined OrgaSegment, Cellpose cyto2, and Canny operator algorithms to further enhance cyto2's performance.

Finally, the gap we observed in the literature of the lack of segmentation resources for images of organoids grown in microfluidic or other engineered environments motivated us to combine multiple softwares with the goal of developing an environment-aware pipeline. Leveraging data of epithelial acini confined in square microwells, we proposed a pipeline of first segmenting the squares using OrgaSegment, then an image restoration algorithm to fill in the dark lines left by PDMS microwells, and then cyto2 to obtain the actual acini segmentations. The results show initial promise towards future refinement to further development of an automated pipeline that can distinguish between organoids and environmental artifacts. Overall, the work here suggests there are benefits in combining the strengths of multiple object identification softwares in situations where access to high-power computers and therefore resources to train complex deep learning models are limited.

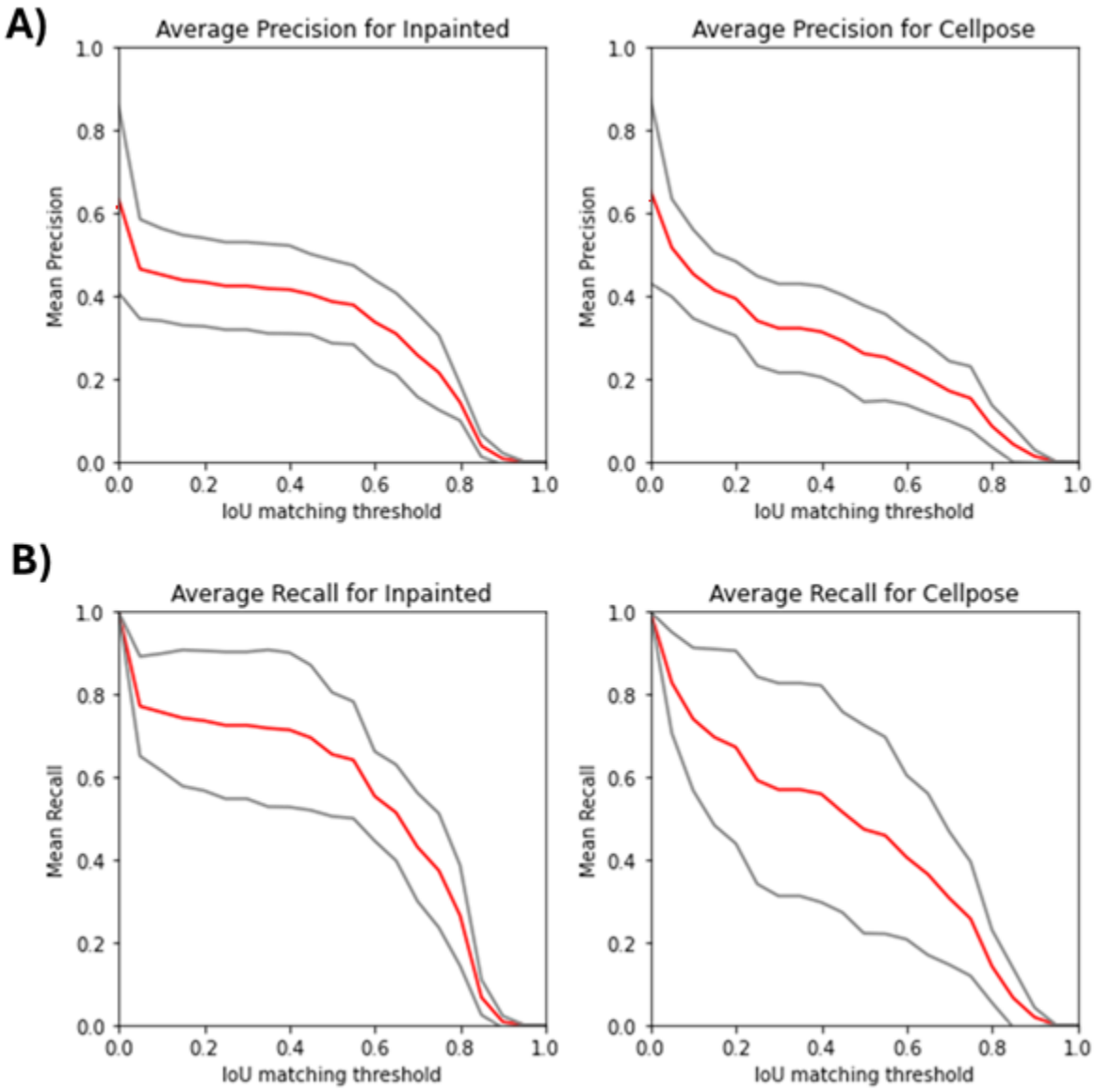

Figure 4.11: Part A and B show average precision and recall over IoU thresholds for the pipeline that includes an inpainting step to eliminate microwell boundaries from the image compared to only Cellpose. The red and gray lines correspond to the mean and the standard deviation respectively. The graphs are generated similarly to in earlier sections of this chapter.

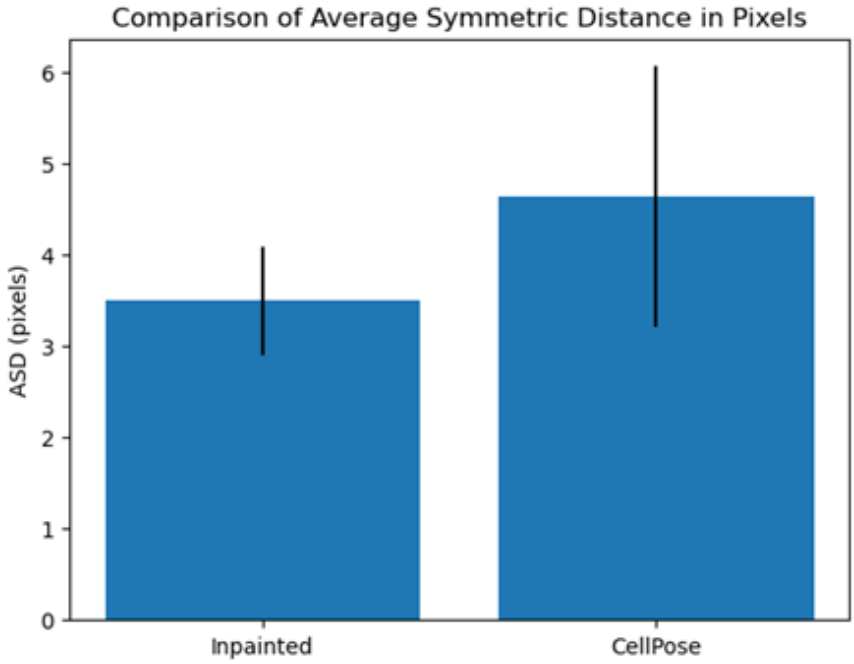

Figure 4.12: Bar plots comparing the ASD of the microwell-aware segmentation pipeline that involves inpainting, versus only Cellpose cyto2. Although the ASD appears lower for the former, statistical significance, or a p-value greater than 0.05, was not observed. Error bars denote standard deviation across the FOVs.

Chapter 5

Discussion and Conclusions

5.1 Summary

Organoids, cysts, and other complex biological structures have been cultured in order to study organ and cancer development, effects of drugs on tissues, and model various biological processes in an environment that more closely mimics *in vivo* settings. One aspect with which to benchmark organoid behaviors is morphology. Examples include how large they grow and how circular they appear. In order to control for and quantify such traits, physical and computational platforms have been developed over the years. Lithography-based microarrays are examples of physical engineered platforms that restrict tissue growth, promoting organoid manufacturing, while providing a microenvironment that can induce physiologically intriguing alterations in morphogenesis. After collecting imaging data, they are fed to segmentation softwares, often based on deep learning models, which can identify organoid and cyst boundaries in brightfield images, thereby facilitating morphological analysis.

However, these platforms have not been completely refined and contain a few issues to overcome. First, navigating complex morphology, both in imaging and segmentation, is a challenge. Due to the three-dimensional patterning of PDMS microwells, high-magnification

and high-resolution imaging of three-dimensional tissue structures inside them are challenging to produce. Segmentation models also lack strategies to deal with organoids or cysts grown in engineered microwell devices. Furthermore, training segmentation algorithms, which requires GPUs, drains resources and finances. In this thesis, we sought to propose solutions to these problems.

First, we designed an imaging platform to maximize SNR of cellular structures despite complex sample topology. We began with fabricating PDMS microwells without requiring clean room access. Then, we optimized a cell seeding protocol to promote trapping and integrated various imaging strategies to enhance image quality of the resulting culture. Utilizing the MDCK epithelial kidney cell line, we were able to apply the microwells to showcase the platform's ability and potential for future experimental studies. More specifically, we showed that the geometric cues imposed by PDMS can disrupt expected characteristics of epithelial growth. Monolayers under high confinement exhibited piling, while the existence of PDMS walls seemed to have impacted lumen development for epithelial acini.

Second, we explored if it was possible to synthesize multiple pre-trained segmentation models to achieve highly specific imaging tasks that require significant amount of training, with the ultimate goal of integration with the physical imaging platform. From a selection of high-achieving segmentation softwares, we assessed their performance via multiple metrics quantifying organoid identification, boundary fidelity, and tracking over time on a basic organoid dataset. Leveraging the top two performers, we tested our hypothesis on two starkly different challenges, one involving irregularly shaped organoids, the other consisting of epithelial cysts grown in PDMS microwells which also appear in the images. By integrating classical computer vision algorithms into the pipeline, we were able to take steps towards overcoming these problems. Together, these enhancements applied to imaging platforms in the physical and computational realms can inform investigations into three-dimensional morphogenetic confinement studies and drug testing.

5.2 Limitations and Future Directions

These platforms contain their fair share of limitations which can be continually improved upon. Cell trapping and acini throughput has not reached the desired level of efficiency and success, so we aim to continue optimizing culture and seeding conditions. We mostly adjusted the cell and Matrigel density as well as microwell dimensions. Thus, follow-up experiments that may be interesting to perform include infusing the cell medium culture with Matrigel instead of generating cell-Matrigel suspensions or varying centrifugation speed and durations [130]. Continuing to explore live imaging platforms in depth is worthwhile as well. Adjusting dimensions of the PDMS holder to constrain thinner PDMS microwell sheets, which are more pliable, is one avenue to test. Finally, one must also consider the possibility that the mounting process can cause stress on biological tissues that impact their appearance during imaging. Minimizing the weight used or performing a procedure similar to tissue mounting on slides to permanently affix them to the coverslip may avoid such undesired situations.

For the segmentation platform, additional improvements to model performance is always desirable because the current pipelines suggest improvement, but with no drastic results. For segmentation of organoids in general, one alternative method to pursue is in reducing shadow and dark artifacts within the brightfield images to increase the recall of the models, further improving object recognition. Potential strategies involve forms of adaptive gamma correction, Retinex, and fusion-based enhancement methods as well as selectively processing only dark regions [20, 41, 76]. Additionally, transfer learning, as long as the numbers of parameters remain modest, may be a potential option to further finetune the model. There has been historical precedent of having personal smartphones perform transfer learning despite its limited resources [157].

For segmentation involving engineered microarrays or microfluidic systems, delving into alternate image restoration algorithms may be beneficial. The Navier-Stokes method, exemplar-

based object removal algorithms, and pre-trained GANs if leaning towards deep learning models are potential options [14, 25, 91]. Ideally, the goal is to replace the dark lines left by the PDMS microwells such that the cysts appear to be growing on a flat surface.

Besides addressing the limitations, the results of these experiments also broach new, interesting questions to explore. How does confinement impact the mechanisms of apical-basal polarity in epithelial cells, and what proteins are most influenced? Are there differences between planar monolayers and monolayers cyst in that aspect? What is the turning point for microwell size that triggers the switch between monolayer and multilayer behavior? What are the epigenetic differences between compressed and non-compressed luminal cells?

Long-term live imaging involving tracking of polarity markers like ezrin, zonula occludens, CD13, E-cadherin, and podocalyxin and comparing to epithelial tissue grown on flat PDMS regions would facilitate understanding of the interplay between mechanical cues, actin and nucleus organization, and apical-basal polarity [40, 99, 163, 177]. Slowly increasing PDMS microwell size by increments of 10 μm maximum as well as adjusting aspect ratios and even geometric shape may allow us to pinpoint the turning point. Finally, incorporating epigenetic markers like Histone H3 Lysine 27 trimethylation (H3K27me3) and Histone H3 Lysine 9 acetylation (H3K9ac) which correspond to downregulation and activation respectively will further our understanding of how confinement induces changes in chromatin [13]. This will then impact the production of proteins, thus leading to downstream effects such as apical-basal polarity development and cell-ECM and cell-cell adhesion.

Besides the study of morphogenesis and apical-basal polarity, the microwells can be utilized to generate organoids or cysts of homogeneous shape and size. Viability assays can be performed to determine if the PDMS microwells negatively impacts health and growth. To further manufacturing, another avenue that can be explored is developing a protocol to harvest organoids from the microwells. Once dislodged from the microarray platform, they can be transferred to another well plate to initiate processes like drug testing and disease

modeling. As large-scale tracking and morphological analysis of low-magnification brightfield images becomes necessary, this is inevitably linked to the second objective of this thesis: developing pipelines that synthesize the strengths of cutting-edge computer vision algorithms for highly specific segmentation tasks.

The continuation of a curated list of segmentation pre-trained softwares accompanied by corresponding metrics describing general, boundary, and tracking performance would be highly beneficial. Furthermore, adding on to the two currently existing pipelines at the moment for other known segmentation challenges will allow us to start building a collection of GPU-free pipelines. Besides what we have already tackled, there are issues involving occlusion, blurriness, dark secretions clouding organoids, necrosis, uneven lighting, graininess, and more. For instance, tumors and tumor organoids are known to develop a necrotic core stemming from a combination of nutrient depletion, inflammation, and hypoxia [33, 173]. Modules that can monitor the ratio of bright to dark, apoptotic areas in tumors over time and therefore function as viability trackers would greatly benefit studies that explore the impact of necrosis on tumor progression and environment. Another possibility is in distinguishing between structures of different types. We observed significant numbers of epithelial aggregates culturing in the wells, which are often characterized with an irregular, "knobbly" appearance. While it has been shown that some epithelial aggregates are capable of developing into cysts and their development is worth examining in the context of geometric cues, it would be beneficial to differentiate from true cysts during data analysis [130]. Therefore, segmentation pipelines that filter them out and group the structures as cysts versus aggregates based on their morphological properties will expedite the quantification process for PDMS microwell studies.

By simultaneously advancing physical and digital platforms that characterize organoid and cyst growth, we can achieve greater insight into these models at different levels. Microfluidics and microfluidics-adjacent technologies like PDMS microwells can precisely control and restrict

their growth and environment. When integrated with high-SNR imaging platforms, they can allow us to qualitatively observe the nuances in tissue morphogenesis and development over time. Meanwhile, segmentation platforms facilitate extraction of high-level morphological details that are linked to the inner workings of the organoid. Together, they can track and identify changes occured in organoid growth and development incurred by physical or chemical cues.

Bibliography

[1] Ayushi Agrawal, Yousef Javanmardi, Sara A Watson, Bianca Serwinski, Boris Djordjevic, Wenbin Li, Amir R Aref, Russell W Jenkins, and Emad Moeendarbary. Mechanical signatures in cancer metastasis. *NPJ Biological Physics and Mechanics*, 2(1):3, 2025.

[2] Sujeong Ahn, Dohyun Kim, Kanghee Cho, and Won-Gun Koh. Microfabrication methods for 3d spheroids formation and their application in biomedical engineering. *Korean Journal of Chemical Engineering*, 40(2):311–324, 2023.

[3] Maath Alani, Hamid A Jalab, Selin Pars, Bahaa Al-Mhanawi, Rowaida Z Taha, Ernst J Wolvetang, and Mohammed R Shaker. Enhanced u-net-based deep learning model for automated segmentation of organoid images. *Bioengineering*, 12(11):1216, 2025.

[4] Jorge Almagro, Hendrik A Messal, Alberto Elosegui-Artola, Jacco van Rheenen, and Axel Behrens. Tissue architecture in tumor initiation and progression. *Trends in cancer*, 8(6):494–505, 2022.

[5] Laith Alzubaidi, Jinglan Zhang, Amjad J Humaidi, Ayad Al-Dujaili, Ye Duan, Omran Al-Shamma, José Santamaría, Mohammed A Fadhel, Muthana Al-Amidie, and Laith Farhan. Review of deep learning: concepts, cnn architectures, challenges, applications, future directions. *Journal of big Data*, 8(1):53, 2021.

[6] Gerard Apodaca. Role of polarity proteins in the generation and organization of apical surface protrusions. *Cold Spring Harbor perspectives in biology*, 10(1):a027813, 2018.

[7] Victoria Aranda, Teresa Haire, Marissa E Nolan, Joseph P Calarco, Avi Z Rosenberg, James P Fawcett, Tony Pawson, and Senthil K Muthuswamy. Par6–apkc uncouples erbb2 induced disruption of polarized epithelial organization from proliferation control. *Nature cell biology*, 8(11):1235–1245, 2006.

[8] Anwai Archit, Luca Freckmann, Sushmita Nair, Nabeel Khalid, Paul Hilt, Vikas Rajashekar, Marei Freitag, Carolin Teuber, Melanie Spitzner, Constanza Tapia Contreras, et al. Segment anything for microscopy. *Nature methods*, 22(3):579–591, 2025.

[9] Reza Azad, Ehsan Khodapanah Aghdam, Amelie Rauland, Yiwei Jia, Atlas Haddadi Avval, Afshin Bozorgpour, Sanaz Karimijafarbigloo, Joseph Paul Cohen, Ehsan Adeli, and Dorit Merhof. Medical image segmentation review: The success of u-net. *IEEE Transactions on Pattern Analysis and Machine Intelligence*, 46(12):10076–10095, 2024.

[10] Riccardo Balzarotti, Cinzia Cristiani, and Lorraine F Francis. Spin coating deposition on complex geometry substrates: Influence of operative parameters. *Surface and coatings technology*, 330:1–9, 2017.

[11] Danielle Baptista, Zeinab Tahmasebi Birgani, Helene Widowski, Fiona Passanha, Vasili Stylianidis, Kèvin Knoops, Eva Gubbins, Cinta Iriondo, Kari-Pekka Skarp, Robbert J Rottier, et al. Polymer film-based microwell array platform for long-term culture and research of human bronchial organoids. *Materials Today Bio*, 19:100603, 2023.

[12] Alexandra Bermudez, Zoe Latham, Johnny Diaz, Weihong Yan, Jerry Chen, Dapeng Bi, Andrew Goldstein, Jimmy K Hu, and Neil YC Lin. Cell jamming transition is regulated by mitochondrial pyruvate transport and endocytosis. *bioRxiv*, pages 2026–02, 2026.

[13] Alexandra Bermudez, Zoe D Latham, Alex J Ma, Dapeng Bi, Jimmy K Hu, and Neil YC Lin. Regulation of chromatin modifications through coordination of nucleus size and epithelial cell morphology heterogeneity. *Communications Biology*, 8(1):269, 2025.

[14] Marcelo Bertalmio, Andrea L Bertozzi, and Guillermo Sapiro. Navier-stokes, fluid dynamics, and image and video inpainting. In *Proceedings of the 2001 IEEE Computer Society Conference on Computer Vision and Pattern Recognition. CVPR 2001*, volume 1, pages I–I. IEEE, 2001.

[15] Cédric Blanpain and Elaine Fuchs. Plasticity of epithelial stem cells in tissue regeneration. *Science*, 344(6189):1242281, 2014.

[16] Rishi Bommasani, Drew A Hudson, Ehsan Adeli, Russ Altman, Simran Arora, Sydney von Arx, Michael S Bernstein, Jeannette Bohg, Antoine Bosselut, Emma Brunskill, et al. On the opportunities and risks of foundation models. *arXiv preprint arXiv:2108.07258*, 2021.

[17] Michael A Borten, Sameer S Bajikar, Nobuo Sasaki, Hans Clevers, and Kevin A Janes. Automated brightfield morphometry of 3d organoid populations by organoseg. *Scientific reports*, 8(1):5319, 2018.

[18] Clare E Buckley and Daniel St Johnston. Apical–basal polarity and the control of epithelial form and function. *Nature reviews Molecular cell biology*, 23(8):559–577, 2022.

[19] Joseph P Campanale, Thomas Y Sun, and Denise J Montell. Development and dynamics of cell polarity at a glance. *Journal of cell science*, 130(7):1201–1207, 2017.

[20] Gang Cao, Lihui Huang, Huawei Tian, Xianglin Huang, Yongbin Wang, and Ruicong Zhi. Contrast enhancement of brightness-distorted images by improved adaptive gamma correction. *Computers & Electrical Engineering*, 66:569–582, 2018.

[21] Austin Castelo, Caleb O'Connor, Aashish C Gupta, Brian M Anderson, McKell Woodland, Mais Altaie, Eugene J Koay, Bruno C Odisio, Tien T Tang, and Kristy K Brock. Quality versus quantity of training datasets for artificial intelligence–based whole liver segmentation. *Medrxiv*, 2026.

[22] Christopher S Chen, Milan Mrksich, Sui Huang, George M Whitesides, and Donald E Ingber. Geometric control of cell life and death. *Science*, 276(5317):1425–1428, 1997.

[23] Jia Chen and Mingjie Zhang. The par3/par6/apkc complex and epithelial cell polarity. *Experimental cell research*, 319(10):1357–1364, 2013.

[24] Danila Coradini, Claudia Casarsa, and Saro Oriana. Epithelial cell polarity and tumorigenesis: new perspectives for cancer detection and treatment. *Acta Pharmacologica Sinica*, 32(5):552–564, 2011.

[25] Antonio Criminisi, Patrick Perez, and Kentaro Toyama. Object removal by exemplar-based inpainting. In *2003 IEEE Computer Society Conference on Computer Vision and Pattern Recognition, 2003. Proceedings.*, volume 2, pages II–II. IEEE, 2003.

[26] Márton Cserni and András Rövid. Combining classical and neural approaches for image segmentation. In *2023 IEEE 21st World Symposium on Applied Machine Intelligence and Informatics (SAMI)*, pages 000033–000038. IEEE, 2023.

[27] Vishal Das, Sourya Bhattacharya, Channakeshavaiah Chikkaputtaiah, Saugata Hazra, and Mintu Pal. The basics of epithelial–mesenchymal transition (emt): A study from a structure, dynamics, and functional perspective. *Journal of cellular physiology*, 234(9):14535–14555, 2019.

[28] Anirban Datta, David M Bryant, and Keith E Mostov. Molecular regulation of lumen morphogenesis. *Current Biology*, 21(3):R126–R136, 2011.

[29] Jordan D Davis and Tomasz P Wypych. Cellular and functional heterogeneity of the airway epithelium. *Mucosal immunology*, 14(5):978–990, 2021.

[30] Paola De Stefano, Elena Bianchi, and Gabriele Dubini. The impact of microfluidics in high-throughput drug-screening applications. *Biomicrofluidics*, 16(3), 2022.

[31] Jayanta Debnath and Joan S Brugge. Modelling glandular epithelial cancers in three-dimensional cultures. *Nature Reviews Cancer*, 5(9):675–688, 2005.

[32] Maxime Deforet, V Hakim, Hannah G Yevick, Guillaume Duclos, and Pascal Silberzan. Emergence of collective modes and tri-dimensional structures from epithelial confinement. *Nature communications*, 5(1):3747, 2014.

[33] Mohammad Dehghany, Vivek Sharma, Akash Samuel Annie-Mathew, Andrei Zakharov, Tom C Hu, Guilherme Pedreira de Freitas Nader, and Vivek B Shenoy. Metabolic starvation–induced cell swelling drives solid stress in tumors. *bioRxiv*, pages 2026–02, 2026.

[34] Jacob Devlin, Ming-Wei Chang, Kenton Lee, and Kristina Toutanova. Bert: Pre-training of deep bidirectional transformers for language understanding. In *Proceedings of the 2019 conference of the North American chapter of the association for computational linguistics: human language technologies, volume 1 (long and short papers)*, pages 4171–4186, 2019.

[35] Eryn E Dixon, Ava M Zapf, Victoria L Halperin Kuhns, Denis Basquin, Rachel M Park, Richard Coleman, Lidiya Franklin, Allison C Lane-Harris, Alexis Hofherr, Michael Köttgen, et al. Extra-ciliary role for polycystins in regulation of ezrin and renal tubular morphology. *bioRxiv*, 2025.

[36] Nhi M Doan, Liangliang Qiang, Zhe Li, Santhisagar Vaddiraju, Gregory W Bishop, James F Rusling, and Fotios Papadimitrakopoulos. Low-cost photolithographic fabrication of nanowires and microfilters for advanced bioassay devices. *Sensors*, 15(3):6091–6104, 2015.

[37] Xuan Du, Yuchen Li, Jiaping Song, Zilin Zhang, Jing Zhang, Yanhui Li, Zaozao Chen, and Zhongze Gu. Precision organoid segmentation technique (post): accurate organoid segmentation in challenging bright-field images. *Bio-Design and Manufacturing*, 9(1):80–93, 2026.

[38] Christopher C DuFort, Matthew J Paszek, and Valerie M Weaver. Balancing forces: architectural control of mechanotransduction. *Nature reviews Molecular cell biology*, 12(5):308–319, 2011.

[39] Madeline K Eiken, Justin E Levine, Shinyeong Lee, Samantha Lukpat, Eleanor M Plaster, Vikram Bala, Jason R Spence, and Claudia Loebel. Polymer design of microwell hydrogels influences epithelial–mesenchymal interactions during human bronchosphere formation. *Advanced nanobiomed research*, 5(1):2300110, 2025.

[40] Alan S Fanning, Christina M Van Itallie, and James M Anderson. Zonula occludens-1 and-2 regulate apical cell structure and the zonula adherens cytoskeleton in polarized epithelia. *Molecular biology of the cell*, 23(4):577–590, 2012.

[41] Xueyang Fu, Delu Zeng, Yue Huang, Yinghao Liao, Xinghao Ding, and John Paisley. A fusion-based enhancing method for weakly illuminated images. *Signal processing*, 129:82–96, 2016.

[42] Chunyuan Gan, Jiaying Zhang, Bo Chen, Ao Wang, Hongyi Xiong, Jiawei Zhao, Chutian Wang, Shuzhang Liang, and Lin Feng. Optoelectronic tweezers micro-well system for highly efficient single-cell trapping, dynamic sorting, and retrieval. *Small*, 20(23):2307329, 2024.

[43] Scott Gehler, Suzanne M Ponik, Kristin M Riching, and Patricia J Keely. Bi-directional signaling: extracellular matrix and integrin regulation of breast tumor progression. *Critical Reviews™ in Eukaryotic Gene Expression*, 23(2), 2013.

[44] Swarnendu Ghosh, Nibaran Das, Ishita Das, and Ujjwal Maulik. Understanding deep learning techniques for image segmentation. *ACM computing surveys (CSUR)*, 52(4):1–35, 2019.

[45] Nicola Gritti, Jia Le Lim, Kerim Anlaş, Mallica Pandya, Germaine Aalderink, Guillermo Martínez-Ara, and Vikas Trivedi. Morgana: accessible quantitative analysis of organoids with machine learning. *Development*, 148(18):dev199611, 2021.

[46] Yuyuan Gu, Wencai Zhang, Xianmin Wu, Yuanwei Zhang, Ke Xu, and Jiacan Su. Organoid assessment technologies. *Clinical and Translational Medicine*, 13(12):e1499, 2023.

[47] R Halaoui and L McCaffrey. Rewiring cell polarity signaling in cancer. *Oncogene*, 34(8):939–950, 2015.

[48] Stefan Harmansa, Alexander Erlich, Christophe Eloy, Giuseppe Zurlo, and Thomas Lecuit. Growth anisotropy of the extracellular matrix shapes a developing organ. *Nature communications*, 14(1):1220, 2023.

[49] Armin Haupt and Nicolas Minc. How cells sense their own shape–mechanisms to probe cell geometry and their implications in cellular organization and function. *Journal of cell science*, 131(6):jcs214015, 2018.

[50] Jiahao He, Shengzhou Shan, Qingfeng Li, Bin Fang, and Yun Xie. Mechanical stretch triggers epithelial-mesenchymal transition in keratinocytes through piezo1 channel. *Frontiers in Physiology*, 13:745572, 2022.

[51] Kaiming He, Georgia Gkioxari, Piotr Dollár, and Ross Girshick. Mask r-cnn. In *Proceedings of the IEEE international conference on computer vision*, pages 2961–2969, 2017.

[52] Kaiming He, Xiangyu Zhang, Shaoqing Ren, and Jian Sun. Deep residual learning for image recognition. In *Proceedings of the IEEE conference on computer vision and pattern recognition*, pages 770–778, 2016.

[53] Ruiwen He, Wang Sik Lee, Phattadon Yajan, Aaron Lee, Mauro Sousa de Almeida, Sandeep Keshavan, Jozef Adamcik, Céline Loussert-Fonta, Dimitri Vanhecke, Barbara Rothen-Rutishauser, et al. Mechanoregulatory effects of cell-scale microwells on epithelial cell phenotype. *Advanced Functional Materials*, page e28452, 2026.

[54] Reka Hollandi, Nikita Moshkov, Lassi Paavolainen, Ervin Tasnadi, Filippo Piccinini, and Peter Horvath. Nucleus segmentation: towards automated solutions. *Trends in Cell Biology*, 32(4):295–310, 2022.

[55] Jeff MP Holly, Li Zeng, and Claire M Perks. Epithelial cancers in the post-genomic era: should we reconsider our lifestyle? *Cancer and Metastasis Reviews*, 32(3):673–705, 2013.

[56] Lucia Hradecká, David Wiesner, Jakub Sumbal, Zuzana Sumbalova Koledova, and Martin Maška. Segmentation and tracking of mammary epithelial organoids in brightfield microscopy. *IEEE Transactions on Medical Imaging*, 42(1):281–290, 2022.

[57] Pengwei Hu, Xun Deng, Feng Tan, and Lun Hu. Multi-axis attention with convolution parallel block for organoid segmentation. *IEEE/CAA Journal of Automatica Sinica*, 11(5):1295–1297, 2024.

[58] Cheng-Kuang Huang, Giovanni J Paylaga, Sasinan Bupphathong, and Keng-Hui Lin. Spherical microwell arrays for studying single cells and microtissues in 3d confinement. *Biofabrication*, 12(2):025016, 2020.

[59] Anneliis Ihermann-Hella, Maria Lume, Ilkka J Miinalainen, Anniina Pirttiniemi, Yujuan Gui, Johan Peränen, Jean Charron, Mart Saarma, Frank Costantini, and Satu Kuure. Mitogen-activated protein kinase (mapk) pathway regulates branching by remodeling epithelial cell adhesion. *PLoS genetics*, 10(3):e1004193, 2014.

[60] Uriah Israel, Markus Marks, Rohit Dilip, Qilin Li, Changhua Yu, Emily Laubscher, Ahamed Iqbal, Elora Pradhan, Ada Ates, Martin Abt, et al. Cellsam: a foundation model for cell segmentation. *BioRxiv*, pages 2023–11, 2025.

[61] Antonio Jacinto, Alfonso Martinez-Arias, and Paul Martin. Mechanisms of epithelial fusion and repair. *Nature cell biology*, 3(5):E117–E123, 2001.

[62] Narjes Jafari and Saeid Abediankenari. Role of micrornas in immunoregulatory functions of epithelial cells. *BMC immunology*, 25(1):84, 2024.

[63] Paul A Janmey, Daniel A Fletcher, and Cynthia A Reinhart-King. Stiffness sensing by cells. *Physiological reviews*, 100(2):695–724, 2020.

[64] Sandra Jardim, João António, and Carlos Mora. Image thresholding approaches for medical image segmentation-short literature review. *Procedia Computer Science*, 219:1485–1492, 2023.

[65] Zhang Jin-Yu, Chen Yan, and Huang Xian-Xiang. Edge detection of images based on improved sobel operator and genetic algorithms. In *2009 International Conference on Image Analysis and Signal Processing*, pages 31–35. IEEE, 2009.

[66] Sagar D Joshi and Lance A Davidson. Epithelial machines of morphogenesis and their potential application in organ assembly and tissue engineering. *Biomechanics and modeling in mechanobiology*, 11(8):1109–1121, 2012.

[67] Hae-Yun Jung, Laurent Fattet, Jeff H Tsai, Taketoshi Kajimoto, Qiang Chang, Alexandra C Newton, and Jing Yang. Apical–basal polarity inhibits epithelial–mesenchymal transition and tumour metastasis by par-complex-mediated snai1 degradation. *Nature cell biology*, 21(3):359–371, 2019.

[68] Dinesh Kalla, Nathan Smith, Fnu Samaah, and Sivaraju Kuraku. Study and analysis of chat gpt and its impact on different fields of study. *International journal of innovative science and research technology*, 8(3), 2023.

[69] Raghu Kalluri, Robert A Weinberg, et al. The basics of epithelial-mesenchymal transition. *The Journal of clinical investigation*, 119(6):1420–1428, 2009.

[70] Do Hyun Kang, Hong Nam Kim, Pilnam Kim, and Kahp-Yang Suh. Poly (ethylene glycol)(peg) microwells in microfluidics: Fabrication methods and applications. *Biochip journal*, 8(4):241–253, 2014.

[71] Ranit Karmakar, Saeid V Nooshabadi, and Allen O Eghrari. Mobile-cellnet: automatic segmentation of corneal endothelium using an efficient hybrid deep learning model. *Cornea*, 42(4):456–463, 2023.

[72] Eyal Karzbrun, Aimal H Khankhel, Heitor C Megale, Stella MK Glasauer, Yofiel Wyle, George Britton, Aryeh Warmflash, Kenneth S Kosik, Eric D Siggia, Boris I Shraiman, et al. Human neural tube morphogenesis in vitro by geometric constraints. *Nature*, 599(7884):268–272, 2021.

[73] Timothy Kassis, Victor Hernandez-Gordillo, Ronit Langer, and Linda G Griffith. Orgaquant: human intestinal organoid localization and quantification using deep convolutional neural networks. *Scientific reports*, 9(1):12479, 2019.

[74] Dilpreet Kaur and Yadwinder Kaur. Various image segmentation techniques: a review. *International journal of computer science and Mobile Computing*, 3(5):809–814, 2014.

[75] Rashmiparvathi Keshara, Yung Hae Kim, and Anne Grapin-Botton. Organoid imaging: seeing development and function. *Annual review of cell and developmental biology*, 38(1):447–466, 2022.

[76] Rizwan Khan, Atif Mehmood, and Zhonglong Zheng. Robust contrast enhancement method using a retinex model with adaptive brightness for detection applications. *Optics Express*, 30(21):37736–37752, 2022.

[77] Mark J Khoury and David Bilder. Distinct activities of scrib module proteins organize epithelial polarity. *Proceedings of the National Academy of Sciences*, 117(21):11531–11540, 2020.

[78] Kristopher A Kilian, Branimir Bugarija, Bruce T Lahn, and Milan Mrksich. Geometric cues for directing the differentiation of mesenchymal stem cells. *Proceedings of the National Academy of Sciences*, 107(11):4872–4877, 2010.

[79] Alexander Kirillov, Eric Mintun, Nikhila Ravi, Hanzi Mao, Chloe Rolland, Laura Gustafson, Tete Xiao, Spencer Whitehead, Alexander C Berg, Wan-Yen Lo, et al. Segment anything. In *Proceedings of the IEEE/CVF international conference on computer vision*, pages 4015–4026, 2023.

[80] Anton S Kornilov and Ilia V Safonov. An overview of watershed algorithm implementations in open source libraries. *Journal of Imaging*, 4(10):123, 2018.

[81] Alex Krizhevsky, Ilya Sutskever, and Geoffrey E Hinton. Imagenet classification with deep convolutional neural networks. *Advances in neural information processing systems*, 25, 2012.

[82] Heidi Kurn and Daniel T Daly. Histology, epithelial cell. 2020.

[83] Kristen Kurtzeborn, Vladislav Iaroshenko, Tomáš Zárybnickỳ, Julia Koivula, Heidi Anttonen, Otto JM Mäkelä, Darren Bridgewater, Ramaswamy Krishnan, Ping Chen, and Satu Kuure. Epithelial cell shape changes contribute to regulation of ureteric bud branching morphogenesis. *The FEBS journal*, 292(23):6253–6282, 2025.

[84] Benoit Ladoux and René-Marc Mège. Mechanobiology of collective cell behaviours. *Nature reviews Molecular cell biology*, 18(12):743–757, 2017.

[85] Junhyeok Lee, Hyungjin Chung, Minseok Suh, Jeong-Hoon Lee, and Kyu Sung Choi. Deep learning for deep learning performance: How much data is needed for segmentation in biomedical imaging? *PLoS One*, 20(12):e0339064, 2025.

[86] Juliet W Lefferts, Suzanne Kroes, Matthew B Smith, Paul J Niemöller, Natascha DA Nieuwenhuijze, Heleen N Sonneveld van Kooten, Cornelis K van der Ent, Jeffrey M Beekman, and Sam FB van Beuningen. Orgasegment: deep-learning based organoid segmentation to quantify cftr dependent fluid secretion. *Communications biology*, 7(1):319, 2024.

[87] Sandra B Lemke and Celeste M Nelson. Dynamic changes in epithelial cell packing during tissue morphogenesis. *Current Biology*, 31(18):R1098–R1110, 2021.

[88] Bing Leng, Hao Jiang, Bidou Wang, Jinxian Wang, and Gangyin Luo. Deep-orga: An improved deep learning-based lightweight model for intestinal organoid detection. *Computers in Biology and Medicine*, 169:107847, 2024.

[89] Xuan Liang, Antonia Weberling, Chun Yuan Hii, Magdalena Zernicka-Goetz, and Clare E Buckley. E-cadherin mediates apical membrane initiation site localisation during de novo polarisation of epithelial cavities. *The EMBO Journal*, 41(24):EMBJ2022111021, 2022.

[90] Han Liu, Yuefeng Liu, He Wang, Qiang Zhao, Tao Zhang, Si-an Xie, Yueqi Liu, Yuanjun Tang, Qin Peng, Wei Pang, et al. Geometric constraints regulate energy metabolism and cellular contractility in vascular smooth muscle cells by coordinating mitochondrial dna methylation. *Advanced Science*, 9(32):2203995, 2022.

[91] Hongyu Liu, Ziyu Wan, Wei Huang, Yibing Song, Xintong Han, and Jing Liao. Pd-gan: Probabilistic diverse gan for image inpainting. In *Proceedings of the IEEE/CVF conference on computer vision and pattern recognition*, pages 9371–9381, 2021.

[92] Ping Liu, Jun Li, Jiaxing Chang, Pinli Hu, Yue Sun, Yanan Jiang, Fan Zhang, and Haojing Shao. Software tools for 2d cell segmentation. *Cells*, 13(4):352, 2024.

[93] Feixiao Long. Microscopy cell nuclei segmentation with enhanced u-net. *BMC bioinformatics*, 21(1):8, 2020.

[94] Marine Luciano, Marie Versaevel, Yohalie Kalukula, and Sylvain Gabriele. Mechanoresponse of curved epithelial monolayers lining bowl-shaped 3d microwells. *Advanced Healthcare Materials*, 13(4):2203377, 2024.

[95] Ilya Lukonin, Marietta Zinner, and Prisca Liberali. Organoids in image-based phenotypic chemical screens. *Experimental & molecular medicine*, 53(10):1495–1502, 2021.

[96] Ahmad Ali Manzoor, Lauren Romita, and Dae Kun Hwang. A review on microwell and microfluidic geometric array fabrication techniques and its potential applications in cellular studies. *The Canadian Journal of Chemical Engineering*, 99(1):61–96, 2021.

[97] Miho Matsuda, Jan Rozman, Sassan Ostvar, Karen E Kasza, and Sergei Y Sokol. Mechanical control of neural plate folding by apical domain alteration. *Nature Communications*, 14(1):8475, 2023.

[98] Jonathan M Matthews, Brooke Schuster, Sara Saheb Kashaf, Ping Liu, Rakefet Ben-Yishay, Dana Ishay-Ronen, Evgeny Izumchenko, Le Shen, Christopher R Weber, Margaret Bielski, et al. Organoid: A versatile deep learning platform for tracking and analysis of single-organoid dynamics. *PLoS computational biology*, 18(11):e1010584, 2022.

[99] Doris Meder, Anna Shevchenko, Kai Simons, and Joachim Fullekrug. Gp135/podocalyxin and nherf-2 participate in the formation of a preapical domain during polarization of mdck cells. *The Journal of cell biology*, 168(2):303–313, 2005.

[100] Luis Fernando Méndez-López. Revisiting epithelial carcinogenesis. *International Journal of Molecular Sciences*, 23(13):7437, 2022.

[101] H MichelleáGrandin et al. Micro-well arrays for 3d shape control and high resolution analysis of single cells. *Lab on a Chip*, 7(8):1074–1077, 2007.

[102] Inês Miranda, Andrews Souza, Paulo Sousa, João Ribeiro, Elisabete MS Castanheira, Rui Lima, and Graça Minas. Properties and applications of pdms for biomedical engineering: A review. *Journal of functional biomaterials*, 13(1):2, 2021.

[103] Phillip A Mlsna and Jeffrey J Rodriguez. Gradient and laplacian edge detection. In *The essential guide to image processing*, pages 495–524. Elsevier, 2009.

[104] Jonathon M Muncie, Nadia ME Ayad, Johnathon N Lakins, Xufeng Xue, Jianping Fu, and Valerie M Weaver. Mechanical tension promotes formation of gastrulation-like nodes and patterns mesoderm specification in human embryonic stem cells. *Developmental cell*, 55(6):679–694, 2020.

[105] Samila Nasrollahi and Amit Pathak. Topographic confinement of epithelial clusters induces epithelial-to-mesenchymal transition in compliant matrices. *Scientific reports*, 6(1):18831, 2016.

[106] Lene N Nejsum and W James Nelson. Epithelial cell surface polarity: the early steps. *Frontiers in bioscience: a journal and virtual library*, 14:1088, 2009.

[107] Celeste M Nelson and Mina J Bissell. Of extracellular matrix, scaffolds, and signaling: tissue architecture regulates development, homeostasis, and cancer. *Annu. Rev. Cell Dev. Biol.*, 22(1):287–309, 2006.

[108] Celeste M Nelson, Ronald P Jean, John L Tan, Wendy F Liu, Nathan J Sniadecki, Alexander A Spector, and Christopher S Chen. Emergent patterns of growth controlled by multicellular form and mechanics. *Proceedings of the National Academy of Sciences*, 102(33):11594–11599, 2005.

[109] W James Nelson. Remodeling epithelial cell organization: transitions between front–rear and apical–basal polarity. *Cold Spring Harbor perspectives in biology*, 1(1):a000513, 2009.

[110] Yasunori Nishimura, Kozo Yano, Masataka Itoh, and Masahiro Ito. Photolithography. *Flat panel display manufacturing*, pages 287–310, 2018.

[111] Christopher E Novak, Kevin D Lucas, Andrzej J Strojwas, and Zhi-Min Ling. Lithography simulation of contamination-caused defects. In *Integrated Circuit Metrology, Inspection, and Process Control IX*, volume 2439, pages 198–209. SPIE, 1995.

[112] Lucy Erin O'Brien, Mirjam MP Zegers, and Keith E Mostov. Building epithelial architecture: insights from three-dimensional culture models. *Nature reviews Molecular cell biology*, 3(7):531–537, 2002.

[113] Owen M O'Connor and Mary J Dunlop. Cell-tractr: A transformer-based model for end-to-end segmentation and tracking of cells. *PLOS Computational Biology*, 21(5):e1013071, 2025.

[114] Marius Pachitariu, Michael Rariden, and Carsen Stringer. Cellpose-sam: superhuman generalization for cellular segmentation. *BioRxiv*, pages 2025–04, 2025.

[115] Yun-Jin Pai, NL Abdullah, SW Mohd.-Zin, RS Mohammed, Ana Rolo, Nicholas DE Greene, Noraishah M Abdul-Aziz, and Andrew J Copp. Epithelial fusion during neural tube morphogenesis. *Birth Defects Research Part A: Clinical and Molecular Teratology*, 94(10):817–823, 2012.

[116] Rachelle N Palchesko, Ling Zhang, Yan Sun, and Adam W Feinberg. Development of polydimethylsiloxane substrates with tunable elastic modulus to study cell mechanobiology in muscle and nerve. *PloS one*, 7(12):e51499, 2012.

[117] Daebeom Park, Soon-Sung Kwon, Yoon A Kim, Joo Young Kim, Baren Jeong, Eun-Ah Park, Yoon Seong Lee, and Whal Lee. A novel hybrid segmentation method coupled with deep learning for coronary artery extraction from coronary ct angiography. *The International Journal of Cardiovascular Imaging*, pages 1–12, 2026.

[118] Jongho Park, Chije Park, Yoshinobu Sugitani, Teruo Fujii, and Soo Hyeon Kim. An electroactive microwell array device to realize simultaneous trapping of single cancer cells and clusters. *Lab on a Chip*, 22(16):3000–3007, 2022.

[119] Joong Yull Park, Mina Morgan, Aaron N Sachs, Julia Samorezov, Ryan Teller, Ye Shen, Kenneth J Pienta, and Shuichi Takayama. Single cell trapping in larger microwells capable of supporting cell spreading and proliferation. *Microfluidics and nanofluidics*, 8(2):263–268, 2010.

[120] Taeyun Park, Taeyul K Kim, Yoon Dae Han, Kyung-A Kim, Hwiyoung Kim, and Han Sang Kim. Development of a deep learning based image processing tool for enhanced organoid analysis. *Scientific reports*, 13(1):19841, 2023.

[121] Colin D Paul, Wei-Chien Hung, Denis Wirtz, and Konstantinos Konstantopoulos. Engineered models of confined cell migration. *Annual review of biomedical engineering*, 18(1):159–180, 2016.

[122] Florent Peglion and Sandrine Etienne-Manneville. Cell polarity changes in cancer initiation and progression. *Journal of Cell Biology*, 223(1):e202308069, 2023.

[123] Vânia C Pinto, Paulo J Sousa, Vanessa F Cardoso, and Graça Minas. Optimized su-8 processing for low-cost microstructures fabrication without cleanroom facilities. *Micromachines*, 5(3):738–755, 2014.

[124] Vaclav Prajzler, Pavla Nekvindova, Jarmila Spirkova, and Martin Novotny. The evaluation of the refractive indices of bulk and thick polydimethylsiloxane and polydimethyldiphenylsiloxane elastomers by the prism coupling technique. *Journal of Materials Science: Materials in Electronics*, 28(11):7951–7961, 2017.

[125] Dong Qin, Younan Xia, and George M Whitesides. Soft lithography for micro-and nanoscale patterning. *Nature protocols*, 5(3):491, 2010.

[126] Yiming Qin, Jiajia Li, Yin Heng, Zheyuan Wang, Dezhi Wu, Mahi Rahman, Pengwei Hu, Tobias Plötz, Alexander Hopp, Nicholas Kurniawan, et al. A knowledge-driven deep learning framework for organoid morphological segmentation and characterization. *BMC Biology*, 23(1):1–14, 2025.

[127] Aditya Ramesh, Mikhail Pavlov, Gabriel Goh, Scott Gray, Chelsea Voss, Alec Radford, Mark Chen, and Ilya Sutskever. Zero-shot text-to-image generation. In *International conference on machine learning*, pages 8821–8831. Pmlr, 2021.

[128] Jacqueline R Rettig and Albert Folch. Large-scale single-cell trapping and imaging using microwell arrays. *Analytical chemistry*, 77(17):5628–5634, 2005.

[129] Alexander Revzin, Ronald G Tompkins, and Mehmet Toner. Surface engineering with poly (ethylene glycol) photolithography to create high-density cell arrays on glass. *Langmuir*, 19(23):9855–9862, 2003.

[130] Astia Rizki-Safitri, Marie Shinohara, Yasushi Miura, Mathieu Danoy, Minoru Tanaka, Atsushi Miyajima, and Yasuyuki Sakai. Efficient functional cyst formation of biliary epithelial cells using microwells for potential bile duct organisation in vitro. *Scientific reports*, 8(1):11086, 2018.

[131] Cristian F Rodríguez, Valentina Andrade-Pérez, María Camila Vargas, Andrés Mantilla-Orozco, Johann F Osma, Luis H Reyes, and Juan C Cruz. Breaking the clean room barrier: exploring low-cost alternatives for microfluidic devices. *Frontiers in Bioengineering and Biotechnology*, 11:1176557, 2023.

[132] Alejo E Rodríguez-Fraticelli, Muriel Auzan, Miguel A Alonso, Michel Bornens, and Fernando Martín-Belmonte. Cell confinement controls centrosome positioning and lumen initiation during epithelial morphogenesis. *Journal of Cell Biology*, 198(6):1011–1023, 2012.

[133] Julie Roignot, Xiao Peng, and Keith Mostov. Polarity in mammalian epithelial morphogenesis. *Cold Spring Harbor perspectives in biology*, 5(2):a013789, 2013.

[134] Olaf Ronneberger, Philipp Fischer, and Thomas Brox. U-net: Convolutional networks for biomedical image segmentation. In *International Conference on Medical image computing and computer-assisted intervention*, pages 234–241. Springer, 2015.

[135] Maria Danielle Sallee, Melissa A Pickett, and Jessica L Feldman. Apical par complex proteins protect against programmed epithelial assaults to create a continuous and functional intestinal lumen. *Elife*, 10:e64437, 2021.

[136] Jacob M Sawyer, Jessica R Harrell, Gidi Shemer, Jessica Sullivan-Brown, Minna Roh-Johnson, and Bob Goldstein. Apical constriction: a cell shape change that can drive morphogenesis. *Developmental biology*, 341(1):5–19, 2010.

[137] Johannes Schindelin, Ignacio Arganda-Carreras, Erwin Frise, Verena Kaynig, Mark Longair, Tobias Pietzsch, Stephan Preibisch, Curtis Rueden, Stephan Saalfeld, Benjamin Schmid, et al. Fiji: an open-source platform for biological-image analysis. *Nature methods*, 9(7):676–682, 2012.

[138] Cora-Ann Schoenenberger, Anna Zuk, Donna Kendall, and Karl S Matlin. Multilayering and loss of apical polarity in mdck cells transformed with viral k-ras. *The Journal of cell biology*, 112(5):873–889, 1991.

[139] Priyansh Sharma and Jenkin Suji. A review on image segmentation with its clustering techniques. *International Journal of Signal Processing, Image Processing and Pattern Recognition*, 9(5):209–218, 2016.

[140] Hyun-Soo Shin, Yun-Min Kook, Hye Jin Hong, Young-Mo Kim, Won-Gun Koh, and Jae-Yol Lim. Functional spheroid organization of human salivary gland cells cultured on hydrogel-micropatterned nanofibrous microwells. *Acta biomaterialia*, 45:121–132, 2016.

[141] Nahian Siddique, Paheding Sidike, Colin Elkin, and Vijay Devabhaktuni. U-net and its variants for medical image segmentation: theory and applications. *arXiv preprint arXiv:2011.01118*, 2020.

[142] Karen Simonyan and Andrew Zisserman. Very deep convolutional networks for large-scale image recognition. *arXiv preprint arXiv:1409.1556*, 2014.

[143] Shauheen S Soofi, Julie A Last, Sara J Liliensiek, Paul F Nealey, and Christopher J Murphy. The elastic modulus of matrigel™ as determined by atomic force microscopy. *Journal of structural biology*, 167(3):216–219, 2009.

[144] Daniel St Johnston and Bénédicte Sanson. Epithelial polarity and morphogenesis. *Current opinion in cell biology*, 23(5):540–546, 2011.

[145] Carsen Stringer, Tim Wang, Michalis Michaelos, and Marius Pachitariu. Cellpose: a generalist algorithm for cellular segmentation. *Nature methods*, 18(1):100–106, 2021.

[146] Elisa Suarez-Martinez, Irene Suazo-Sanchez, Manuel Celis-Romero, and Amancio Carnero. 3d and organoid culture in research: physiology, hereditary genetic diseases and cancer. *Cell & Bioscience*, 12(1):39, 2022.

[147] Lawrence P Sullivan, Darren P Wallace, and Jared J Grantham. Epithelial transport in polycystic kidney disease. *Physiological reviews*, 78(4):1165–1191, 1998.

[148] Jie Sun, Md Biplob Hosen, Wu-Min Deng, and Aiguo Tian. Epithelial polarity loss and multilayer formation: Insights into tumor growth and regulatory mechanisms. *BioEssays*, 47(3):e202400189, 2025.

[149] Mengyan Sun, Zhaohui Wu, Mingqiang Hu, Wei Luo, Xiaole Chen, and Ming Ma. Epithelial dynamics of cystogenesis in genetic models of autosomal dominant polycystic kidney disease. *Cells*, 15(3):297, 2026.

[150] Rui Sun, Tao Lei, Qi Chen, Zexuan Wang, Xiaogang Du, Weiqiang Zhao, and Asoke K Nandi. Survey of image edge detection. *Frontiers in Signal Processing*, 2:826967, 2022.

[151] Christian Szegedy, Wei Liu, Yangqing Jia, Pierre Sermanet, Scott Reed, Dragomir Anguelov, Dumitru Erhan, Vincent Vanhoucke, and Andrew Rabinovich. Going deeper with convolutions. In *Proceedings of the IEEE conference on computer vision and pattern recognition*, pages 1–9, 2015.

[152] Mohsen Taghizadeh, Ali Taghizadeh, and Hye Sung Kim. Mechanobiological engineering strategies for organoid culture. *APL bioengineering*, 9(3), 2025.

[153] Vivian Tang. Cell-cell adhesion interface: rise of the lateral membrane. *F1000research*, 6:276, 2017.

[154] Alexandru Telea. An image inpainting technique based on the fast marching method. *Journal of graphics tools*, 9(1):23–34, 2004.

[155] Manuel Théry, Victor Racine, Matthieu Piel, Anne Pépin, Ariane Dimitrov, Yong Chen, Jean-Baptiste Sibarita, and Michel Bornens. Anisotropy of cell adhesive microenvironment governs cell internal organization and orientation of polarity. *Proceedings of the National Academy of Sciences*, 103(52):19771–19776, 2006.

[156] Aiguo Tian, Xian-Feng Wang, Yuting Xu, Virginia Morejon, Yi-Chun Huang, Chidi Nwapuda, and Wu-Min Deng. Egfr signaling controls directionality of epithelial multilayer formation upon loss of cell polarity. *The EMBO journal*, 42(24):EMBJ2023113856, 2023.

[157] Olivier Valery, Pangfeng Liu, and Jan-Jan Wu. Cpu/gpu collaboration techniques for transfer learning on mobile devices. In *2017 IEEE 23rd International Conference on Parallel and Distributed Systems (ICPADS)*, pages 477–484. IEEE, 2017.

[158] Alexandra Dunnum VandeLoo, Nathan J Malta, Saahil Sanganeriya, Emilio Aponte, Caitlin van Zyl, Danfei Xu, and Craig Forest. Samcell: Generalized label-free biological cell segmentation with segment anything. *Plos one*, 20(9):e0319532, 2025.

[159] Ashish Vaswani, Noam Shazeer, Niki Parmar, Jakob Uszkoreit, Llion Jones, Aidan N Gomez, Łukasz Kaiser, and Illia Polosukhin. Attention is all you need. *Advances in neural information processing systems*, 30, 2017.

[160] Athanasios Voulodimos, Nikolaos Doulamis, Anastasios Doulamis, and Eftychios Protopapadakis. Deep learning for computer vision: A brief review. *Computational intelligence and neuroscience*, 2018(1):7068349, 2018.

[161] Zhijiang Wan, Manyu Li, Zihan Wang, Hai Tan, Wei Li, Lisu Yu, and Dinesh Jackson Samuel. Cellt-net: a composite transformer method for 2-d cell instance segmentation. *IEEE Journal of Biomedical and Health Informatics*, 28(2):730–741, 2023.

[162] Chun-Chao Wang, Leen Jamal, and Kevin A Janes. Normal morphogenesis of epithelial tissues and progression of epithelial tumors. *Wiley Interdisciplinary Reviews: Systems Biology and Medicine*, 4(1):51–78, 2012.

[163] Li-Ting Wang, Abira Rajah, Claire M Brown, and Luke McCaffrey. Cd13 orients the apical-basal polarity axis necessary for lumen formation. *Nature Communications*, 12(1):4697, 2021.

[164] Lin Wang, Shashi K Murthy, William H Fowle, Gilda A Barabino, and Rebecca L Carrier. Influence of micro-well biomimetic topography on intestinal epithelial caco-2 cell phenotype. *Biomaterials*, 30(36):6825–6834, 2009.

[165] Q Wang and B Margolis. Apical junctional complexes and cell polarity. *Kidney international*, 72(12):1448–1458, 2007.

[166] Yuli Wang, Asad A Ahmad, Christopher E Sims, Scott T Magness, and Nancy L Allbritton. In vitro generation of colonic epithelium from primary cells guided by microstructures. *Lab on a Chip*, 14(9):1622–1631, 2014.

[167] Cameron J Wells, Najwa Labban, Shayna L Showalter, Róża K Przanowska, and Kevin A Janes. Fast learning-free organoid quantification and tracking with organoseg2. *Scientific Reports*, 2026.

[168] John D Williams and Wanjun Wang. Study on the postbaking process and the effects on uv lithography of high aspect ratio su-8 microstructures. *Journal of Micro/Nanolithography, MEMS and MOEMS*, 3(4):563–568, 2004.

[169] Wang Xi, Surabhi Sonam, Thuan Beng Saw, Benoit Ladoux, and Chwee Teck Lim. Emergent patterns of collective cell migration under tubular confinement. *Nature communications*, 8(1):1517, 2017.

[170] Hanguang Xiao, Li Li, Qiyuan Liu, Xiuhong Zhu, and Qihang Zhang. Transformers in medical image segmentation: A review. *Biomedical Signal Processing and Control*, 84:104791, 2023.

[171] Jing Yang, Parker Antin, Geert Berx, Cédric Blanpain, Thomas Brabletz, Marianne Bronner, Kyra Campbell, Amparo Cano, Jordi Casanova, Gerhard Christofori, et al. Guidelines and definitions for research on epithelial–mesenchymal transition. *Nature reviews Molecular cell biology*, 21(6):341–352, 2020.

[172] Duygu Yazici, Ismail Ogulur, Yagiz Pat, Huseyn Babayev, Elena Barletta, Sena Ardicli, Mengting Huang, Jana Koch, Manru Li, Debbie Maurer, et al. The epithelial barrier: the gateway to allergic, autoimmune, and metabolic diseases and chronic neuropsychiatric conditions. In *Seminars in immunology*, volume 70, page 101846. Elsevier, 2023.

[173] Patricia P Yee and Wei Li. Tumor necrosis: A synergistic consequence of metabolic stress and inflammation. *Bioessays*, 43(7):2100029, 2021.

[174] Liying Yuan and Xue Xu. Adaptive image edge detection algorithm based on canny operator. In *2015 4th International Conference on Advanced Information Technology and Sensor Application (AITS)*, pages 28–31. IEEE, 2015.

[175] Meiling Zhang and Bin Zhang. Extracellular matrix stiffness: mechanisms in tumor progression and therapeutic potential in cancer. *Experimental hematology & oncology*, 14(1):54, 2025.

[176] Jianhua Zhou, Jianpei Dong, Hongwei Hou, Lu Huang, and Jinghong Li. High-throughput microfluidic systems accelerated by artificial intelligence for biomedical applications. *Lab on a Chip*, 24(5):1307–1326, 2024.

[177] Lixin Zhu, James Crothers Jr, Rihong Zhou, and John G Forte. A possible mechanism for ezrin to establish epithelial cell polarity. *American Journal of Physiology-Cell Physiology*, 299(2):C431–C443, 2010.